Nitriding of medical grade CoCrMo alloys using HIPIMS discharge

Krishnanand S. P. Shukla

A thesis submitted in the partial fulfilment of the requirements of

Sheffield Hallam University

For the degree of Doctor of Philosophy

In Collaboration with The National HIPIMS technology Centre, UK
at Sheffield Hallam University and Zimmer Biomet UK

May 2021

To: Sahadev Prasad, Vijay Laxmi, Brahmanand, Himani and Pooja

सहदेव प्रसाद, विजय लक्ष्मी, ब्रह्मानंद, हिमानी और पूजा

“अनेकसंशयोच्छेदि, परोक्षार्थस्य दर्शकम् ।
सर्वस्य लोचनं शास्त्रं, यस्य नास्त्यन्ध एव सः ॥“

It blasts many doubts, foresees what is not obvious |
Science is the eye of everyone, one who hasn't got it, is like a blind ||

Declaration

I hereby declare that:

1. I have not been enrolled for another award of the University, or other academic or professional organisation, whilst undertaking my research degree.
2. None of the material contained in the thesis has been used in any other submission for an academic award.
3. I am aware of and understand the University's policy on plagiarism and certify that this thesis is my own work. The use of all published or other sources of material consulted have been properly and fully acknowledged.
4. The work undertaken towards the thesis has been conducted in accordance with the SHU Principles of Integrity in Research and the SHU Research Ethics Policy.
5. The word count of the thesis is **40,640**.

Name	*Krishnanand S. P. Shukla*
Date	*15th May 2021*
Award	*PhD*
Faculty	*BTE*
Director(s) of Studies	*Professor Papken Hovsepian*

Abstract

The aim of this work was to develop a plasma nitriding process for a bio-grade CoCrMo alloy using a High Power Impulse Magnetron Sputtering (HIPIMS) discharge. An industrial-sized PVD machine (Hauzer techno Coating 1000-4, The Netherlands) machine equipped with two HIPIMS and two DC power supplies was utilised for this objective. Low-pressure plasma nitriding was carried out in a H_2:N_2 (15:85) environment with different nitriding voltages (-500 V to -1100 V). Nitrided specimens thoroughly were characterised using various techniques. To understand the effect of nitriding voltage on the phase composition and texture (T*) x-ray diffraction (XRD) was used. Microstructural changes due to the variation in nitriding voltage w investigated using a focused ion beam Scanning electron microscope (FIB-SEM) equipped with various detectors such as secondary electron (SE) and back scattered (BSE). Extent of nitrogen diffusion was analysed using GDOES and SIMS. Elemental analysis of the virgin nitrided layer and analysed surfaces were performed using point, line, and colour mapping electron diffraction spectroscopy (EDS). Nano/Micro hardness testers were used to understand the effect of nitriding voltage on hardness (Hp and HV) and fracture toughness (K_{Ic}). A high frequency macro impact load tester was used to understand the effect of nitriding voltage on impact fatigue behaviour of the compound layers. Fractured surfaces were analysed using SEM and FIBSEM after static and cyclic loading to understand the deformation mechanism such as fatigue cracking underneath nitrided layer. Potentiodyanmic polarisation study was performed in 3.5 wt.% NaCl and Hank's solution to analyse the corrosion performance of these nitrided layers. At the end, HIPIMS plasma nitrided specimens were compared with benchmarked DC plasma nitrided specimens. Sample nitrided using HIPIMS discharge at -900 V exhibited novel phase composition, superior hardness and fracture toughness, better wear resistance, improved corrosion resistance and reduced metal ion release compared to the benchmarked DCPN.

Acknowledgements

"A good boss makes his men realize they have more ability than they think they have so that they consistently do better work than they thought they could- Charles Erwin Wilson". First of all, I would like to thank director of studies Professor Papken Eh. Hovsepian for allowing me to carry out PhD work at National HIPIMS Technology Centre, SHU. His unconditional support and valuable guidance have helped me to reach up to this part of the ladder.

I would like to express my gratitude to Dr. Imran Khan my second supervisor from Zimmer-Biomet UK for providing financial support to sail through the journey of my research work.

It is a genuine pleasure to express my deep sense of heartfelt regards to Dr. Yashodhan Purandare who has been my mentor, guide, and a great support throughout my course of studies. Without his guidance and persistent help this road would have been incomplete. "A good teacher can educate a student, but a good mentor can shape a student future".

I would like to show my appreciation to Prof. Arutiun P. Ehiasarian for his precious feedbacks during my studies.

I would also like to thank my colleagues Dr. Daniel D. L. Loch, Dr. Arunprabhu Arunachalam Sugumaran, Mr. Paul Allender and Mr. Stuart for their support and encouragement.

I would like to extend my sincere thanks to Mr. Gary Robinson for being great source of encouragement and also for supporting me in the lab to prepare the samples as well as for doing proofreading of my thesis and papers.

I would like to specially acknowledge my housemate Mr. Kushal Kumar Chode for his help since the first day of my UK journey. I want to thank all MERI staff (Mr. Paul Allender and Dr. Anthony Bell) and student (current and past) for their help and support.

Special thanks to Mr. Sanjay Mistry and Mrs. Sonia Mistry Santos for making me feel at home when I was new to this part of the world. I would not have had it any other way.

I would like to thank Shri Ramesh Subramanyam and Miss Tanvi Patel for supporting me through hard times and giving me moral support to perceive my goals.

It is my pleasure to thank my elder brother Mr. Brahmanand Shukla and sister-in-law Mrs. Himani Shukla since they have put their dreams behind to make sure that I achieve mine. I would like to thank my father Mr. Sahadev Prasad Shukla and Mother Mrs. Vijay Laxmi Shukla for their moral support. A big thanks to my wife Mrs. Pooja Shukla for being part of this journey and walking me through it while I put my foot onto my final destination.

Advance Studies

During the course of the studies for this thesis, the following conferences and workshops were attended:

- MERI Research Symposium 2018, Sheffield, UK, May 2018.
- 9th HIPIMS conference, Sheffield, UK, June 2018.
- 10th HIPIMS and Sputter Technology conference, June 2019.
- MERI Research Symposium 2019, Sheffield, UK, May 2019.
- International Student Conference in Metallic Materials 2020 ’Sustainability in Metals Manufacturing’, July 2020.
- Young person lecture competition jointly organized by Sheffield Metallurgy and Engineering Association and IOM3, March 2021.
- Royce Student Summit organized by Henry Royce institute, March 2021.
- SVC TechCon 2021 virtual, May 2021.
- 11th International conference on Fundamental and Industrial Application of HIPIMS, June 2021.
- MERI Research Symposium 2021, Sheffield, UK, June 2021.
- SVC Courses - 323 High Power Impulse Magnetron Sputtering, 333 Practice and Applications of High-Power Impulse Magnetron Sputtering (HIPIMS), 338 Application of Reactive Sputtering, Sheffield, UK, June 2018, 230 Design and Specification of Vacuum Deposition Systems (Belan), May 2021 virtual.

List of Publications

Refereed Scientific Publications

- K. Shukla, A. A. Sugumaran, I. Khan, A. P. Ehiasarian, and P. E. Hovsepian, "Low pressure plasma nitrided CoCrMo alloy utilising HIPIMS discharge for biomedical applications," *J. Mech. Behav. Biomed. Mater.*, vol. 111, p. 104004, Nov. 2020, doi: https://doi.org/10.1016/j.jmbbm.2020.104004.
- K. Shukla, Y. P. Purandare, I. Khan, A. P. Ehiasarian, and P. E. H. Hovsepian, "Effect of nitriding voltage on the impact load fatigue and fracture toughness behaviour of CoCrMo alloy nitrided utilising a HIPIMS discharge," *Surf. Coatings Technol.*, vol. 400, p. 126227, Oct. 2020, doi: https://doi.org/10.1016/j.surfcoat.2020.126227.
- A. Sugumaran, K. Shukla, I. Khan, A. P. Ehiasarian, and P. E. Hovsepian, "Dry sliding wear mechanisms of HIPIMS plasma nitrided CoCrMo alloy for medical implant applications," *Vacuum*, vol. 185, no. December 2020, p. 109994, Mar. 2021, doi: https://doi.org/10.1016/j.vacuum.2020.109994.
- K. Shukla, Y. Purandare, A. Sugumaran, A. Ehiasarian, I. Khan, and P. Hovsepian, "Correlation between the microstructure and corrosion performance of the HIPIMS nitrided bio-grade CoCrMo alloy," *J. Alloys Compd.*, vol. 879, p. 160429, Oct. 2021, doi: https://doi.org/10.1016/j.jallcom.2021.160429.
- K. Shukla, Y. P. Purandare, A. A. Sugumaran, Daniel Loch, I. Khan, A. P. Ehiasarian, and P. E. H. Hovsepian "A New Approach Towards Performing Plasma Nitriding Of CrCoMo Medical Grade Alloys Using HIPIMS Discharge," 64th Annual Technical Conference Proceedings © 2021 Society of Vacuum Coaters, Virtual Event: May 3 – 7, 2021, https://doi.org/10.14332/svc21.proc.0000.

Publication not Directly related to this Thesis

- A. Sugumaran, Y. Purandare, K. Shukla, I. Khan, A. P. Ehiasarian, and P. E. Hovsepian, "TiN/NbN nanoscale multilayer coatings deposited by High Power Impulse Magnetron Sputtering to protect medical grade CoCrMo alloys," Coatings,Vol. 11(7), p. 867, July 2021, doi: https://doi.org/10.3390/coatings11070867.
- A. E. Alam, O. I. Olusola, D. A. L. Loch, K. Shukla, W. M. Cranton, and I. M. Dharmadasa, "Electrodeposition of ternary compounds for novel PV application and optimisation of electrodeposited CdMnTe thin-films," *Sci. Rep.*, vol. 10, no. 1, pp. 1–13, 2020, doi: https://doi.org/10.1038/s41598-020-78066-y.
- I. Solomon, K. Shukla, M. Bhatnagar, R. Rane, M. Ranjan, F. Gourbilleau, A. Sarma, "Effect of nitrogen concentrations on optical, structural and mechanical properties of self organized a-C:N films," *Ceram. Int.*, 2020, doi: https://doi.org/10.1016/j.ceramint.2020.02.163.

List of Contents

List of Abbreviations

HIPIMS:	High Power Impulse Magnetron Sputtering
PN:	Plasma Nitriding
DCPN:	Direct Current Plasma Nitriding
HLPN:	HIPIMS Low Pressure Plasma Nitriding
UBM:	Unbalanced Magnetron Sputtering
CP:	Commercially Pure
ASS:	Austenite Stainless Steel
SS:	Stainless Steel
XRD:	X-ray Diffraction
BB:	Bragg– Brentano
GA:	Glancing Angle
SEM:	Secondary Electron Microscopy
FIBSEM:	Focused Ion Beam Secondary Electron Microscope
FIBCS:	Focused Ion Beam Cross-Section
SE:	Secondary Electron
BSE:	Back Scattered Electron
SIMS:	Secondary Ion Mass Spectrometry
GDOES:	Glow Discharge Optical Emission Spectroscopy
LPPN:	Low-Pressure Plasma Nitriding
Compound layer:	$Metal_{2\text{-}3}N+Metal_4N$

Diffusion layer: $Metal_4N$

PI³: Plasma Immersion Ion Implantation

PI²: Plasma Ion Implantation

Expanded Austenite: γ_N

sccm: Standard Cubic Centimeter Per Minute

SBS: Simulated Body Fluid

PVD: Physical Vapor Deposition

MS: Magnetron Sputtering

PPS: Pulsed Plasma Sputtering

CFC: Closed-Field Configuration

SZD: Structure Zone Diagram

Hp: Surface Nanohardness

SBF: **S**imulated Body Fluid

List of Figures

List of Tables

Chapter 1

1.1. Introduction

The development of new orthopaedic implants based on the knee, hip, and components for fixation of bone using different biocompatible alloys such as CoCr alloy, Ti6Al4V alloy, stainless steel (AISI 316L, AISI 304L) has become a major challenge for the researchers. In 2016 the worldwide orthopaedic market was reported at more than US$40bn and it has been increased by 4.2% since 2015 [1]. Also, it was found that only the knee implant itself has a market of $9.3Bn and has seen 4.5% growth in 2016. In the European Union (EU), Germany was the biggest market for all sectors followed by the United Kingdom (UK), France and Italy. It has been observed that joint and knee problems are most common in India and Hip problems in the EU [2][3].

In the last few decades, the number of cases of arthritis in the United Kingdom has increased significantly, which is considered to be degenerative disease. This diseases in long term can lead to wear of bone due to the extreme loading or could also result in the absence of biological self-healing process [4]

The relative motion of two bone prosthetics (Metal-On-Metal) or prosthetic on host bone, generates the debris which are often referred to wear induced loss of material from various prosthetic components. Biological reaction due to the debris or corrosion products is also considered to be crucial in pathogenesis of aseptic loosening. The cytotoxicity of the polymeric/metallic implant, biomaterials immunologic hypersensitivity to specific biomaterial components such as Co, Ni are other factors contributing to biological reactions [5][6]. However, state-of-the-art solutions are arising from surface and metallurgical science, to avoid such unwanted events, focusing on obtaining initial solution of the prosthesis [5][7][8]. It is also considered that the reduction of the surface roughness will improve the coupling of

materials, so those amounts of toxic particles will be reduced [9]. Meanwhile, to minimize the stress shielding between the prosthetic and bone can be adjusted by adopting elasticity of the implant material [5][9][10].

It is also estimated that around 1% of patients with metal-on-metal resurfacing generated a pseudotumor in less than five years [11][12] and it is speculated that the adverse effects could be mediated by an allergic response to 'normal' levels of metal debris or could be caused directly by toxic concentrations of chromium (Cr), Nickel (Ni) and cobalt (Co) generated from bearing surfaces experiencing abnormal wear [12][13]. The articulating metallic surface may not have enough wear resistance, but it has excellent hardness and corrosion resistances. For example, CoCr alloy and AISI 316L has excellent corrosion resistance because of the high amount of Cr which forms different forms of oxides such as Cr_2O_3, CrO_2 at the surface and serve as a barrier against corrosion. There are also minor contributions of Co and Mo oxides [14].

To enhance the wear and mechanical properties of these alloys many surface coatings and ion implantation processes have been performed. In the past few years different methods such as gas nitriding (GN) [15][16], plasma carburising (PC), pulsed plasma nitriding [17], high-intensity plasma ion nitriding (HIPIN) [19], intensified plasma-assisted nitriding (IPAP), plasma immersion ion implantation (PIII) [19][20], laser gas nitriding [21], radio frequency plasma nitriding (RFPN) [21] and HIPIMS duplex Coating [23] have been introduced. In order to increase the life span of CoCrMo alloy-based prosthesis bearing surfaces, duplex coatings [24] have been developed. It was found that duplex coatings have superior properties which are unobtainable through any individual surface modification [25].

Wei Ronghya and coworkers, (2004) has applied the HIPIN technique to improve the tribological property of the CoCrMo and Ti6Al4V alloy, which takes advantage of low energy ion implantation at an elevated temperature that produces a thick nitride layer (a combination

of γ_N phase and compound layer). During this study, they also observed that with increase in ion energy, the diffusion depth increases systematically [18]. The formation of the nitrided layer up to a few microns on the surface improves the wear resistance of Ti alloy by over two orders of magnitude [25]. A.F. Yetim and coworkers (2010), have found that duplex treatment combining Ti: DLC coating with plasma nitriding can improve the hardness of Ti6Al4V by seven times. In this study, superior wear performance of duplex treatment was attributed to higher load-bearing capacity and reduced subsurface deformation [27]. Hovsepian and Ehiasarian have proposed a method to utilize High Power Impulse Magnetron Sputtering discharge to produce highly ionised plasma to be used for plasma nitriding. Applying high bias voltage at the substrate can produce high energy N^{2+} and N^{+} ions and increase their density [23]. They also found that the diffusion depth increases with an increase in bias potential and therefore the load bearing capacity of such layers when a hard coating is deposited on top. This research also demonstrated that both nitriding and coating deposition process can be produced in a single PVD system, [23]. Luo Xia and coworkers (2013), have shown that the improvement of fretting wear of the bone joints surface and the load-bearing capacity of CoCrMo alloy can be improved by performing duplex treatment [24]. The duplex treatment consists of a Nitrided layer and nanostructured coating produced in a single system [23].

1.2. Aim and Objective

The main aim of this thesis is to set up the procedure for in-situ plasma nitriding and deposition of a nanostructured coating in a single unit such as industrial size Hauzer PVD system. Based on the motivation mentioned earlier, we aim to develop in-situ duplex coatings with excellent adhesion, mechanical, tribological and corrosion properties to increase the longevity of biomedical alloys. The main idea behind this work is to obtain high nitriding depth using HIPIMS discharge to enhance the ionization of the reactive gas used for the plasma thermo- chemical process and thereby reduce the process time. This process will then be

followed by the deposition of a highly wear resistant nanoscale multilayer structured top coating, the entire duplex treatment being executed in a single PVD unit. HIPIMS plasma nitriding has already proven that it is possible to obtain a thick nitride layer in a shorter process time with a low surface roughness (an almost polished surface) [22]. An industrial-size four cathode magnetron sputtering system enabled with HIPIMS technology at the National HIPIMS Technology Centre at Sheffield Hallam University is used for this study. Low-temperature plasma nitriding has been chosen since it exhibits an expanded austenite phase (S phase or Diffusion layer- $\boldsymbol{\gamma'}-Co_4\boldsymbol{N}$) and a compound phase ($\boldsymbol{\gamma'}-Co_4\mathbf{N}$,+ $Co_{2-3}\mathbf{N}$). The excellent fatigue property of the N-interstitial (diffusion zone) and better tribological and anti-corrosion property of the compound layer makes this modification more interesting [27].

- To investigate HIPIMS enhanced Low-Pressure Plasma Nitriding (HLPPN) at different bias voltage such as -500 V to -1100 V with a consecutive difference of -100 V.
- To understand the effect of bias voltage on the diffusion of atomic nitrogen (N^+) into an interstitial position of the austenitic structure of CoCrMo alloy using a range of surface analysis techniques.
- To better understand the effect of bias voltage on the thickness of the nitrided layer (*compound ($Co_4\mathbf{N}$+ $Co_{2-3}\mathbf{N}$) and diffusion layer ($Co_4\mathbf{N}$)*.
- To understand the effect of bias voltage on the corrosion, tribological and mechanical properties of the CoCrMo alloy.
- To compare the phase composition and microstructure of the commercial DC plasma nitride (DCPN) with HIPIMS low pressure plasma nitrided (HLPN) one.
- To compare the tribological, mechanical and electrochemical properties of the CoCrMo alloy with DCPN and HLPN.

References

1. A. Madani, “2016 worldwide orthopaedic market,” 2017. [Online]. Available: https://implants-event.com/technology/2016-worldwide-orthopaedic-market-figures-dynamics-and-competition/.
2. Glen Hare “Global Bio-Implants Market (2014 - 2020) : North America has the largest market followed by Europe.” Industrytoday.co.uk.
3. The global orthopedic joint replacement market size was USD 20.00 billion in 2019 and is projected to reach USD 26.89 billion by 2027, exhibiting a CAGR of 7.6% during the forecast period.... Read More at:- https://www.fortunebusinessinsights.com/industry-reports/orthopedic-joint-replacement-market-100314.
4. M. Geetha, A. K. Singh, R. Asokamani, and A. K. Gogia, “Ti based biomaterials, the ultimate choice for orthopaedic implants - A review,” *Progress in Materials Science*. 54 (3) 2009, 397-425. DOI: 10.1016/j.pmatsci.2008.06.004.
5. F. Guillemot, “Recent advances in the design of titanium alloys for orthopaedic applications,” *Expert Review of Medical Devices*, vol. 2, no. 6. pp. 741–748, 2005.
6. E. Denkhaus and K. Salnikow, “Nickel essentiality, toxicity, and carcinogenicity,” *Crit. Rev. Oncol. Hematol.*, vol. 42, no. 1, pp. 35–56, 2002.
7. M. C. Porté-Durrieu *et al.*, “Cyclo-(DfKRG) peptide grafting onto Ti-6Al-4V: Physical characterization and interest towards human osteoprogenitor cells adhesion,” *Biomaterials*, vol. 25, no. 19, pp. 4837–4846, 2004.
8. T. M. Xiao SJ, Kenausis G, “No Title,” *Springer-Verlag, Berlin, Ger.*, vol. Biochemica, pp. 417–455.
9. T. E. McGovern, J. Black, J. J. Jacobs, R. M. Graham, and M. LaBerge, “In vivo wear of Ti6A14V femoral heads: A retrieval study” J. Biomed. Mater. Res., 32 (3) 1996,

pages: 447-457. DOI:10.1002/(SICI)1097-4636(199611)32:3<447:AID-JBM19>3.0.CO;2-D

10. E. Wintermantel, J. Mayer, and T. N. Goehring, “Composites for Biomedical Applications,” K. H. J. Buschow, R. W. Cahn, M. C. Flemings, B. Ilschner, E. J. Kramer, S. Mahajan, and P. B. T.-E. of M. S. and T. Veyssière, Eds. Oxford: Elsevier, 2001, pp. 1371–1376.
11. H. Pandit et al., “Pseudotumours associated with metal-on-metal hip resurfacings,” J. Bone Jt. Surg. - Br. Vol., 90 (7) 2008, pages: 847-851. DOI: 10.1302/0301-620X.90B7.20213
12. D. J. Langton, S. S. Jameson, T. J. Joyce, N. J. Hallab, S. Natu, and A. V. F. Nargol, “Early failure of metal-on-metal bearings in hip resurfacing and large-diameter total hip replacement: A CONSEQUENCE OF EXCESS WEAR,” *J. Bone Jt. Surg. - Br. Vol.,* 2010.
13. R. De Haan, P. A. Campbell, E. P. Su, and K. A. De Smet, “Revision of metal-on-metal resurfacing arthroplasty of the hip: THE INFLUENCE OF MALPOSITIONING OF THE COMPONENTS,” *J. Bone Jt. Surg. - Br. Vol.,* 2008.
14. Zina Noori Abdulhameed, “Corrosion Behavior of Some Implant Alloys in Simulated Human Body Environment Republic of Iraq Corrosion Behavior of Some Implant Alloys in Simulated Human Body Environment A Thesis Submitted To The Department of Materials engineering, University of Tech,” University of Technology, Republic of Iraq, 2015.
15. M. Yang and R. Jr, *Alloy Effects on the Gas Nitriding Process*, vol. 23. 2014.
16. D. Lee, W. Ali Abro, K. Sang Lee, M. Abro, I. Pohrelyuk, and O. Yaskiv, *Gas Nitriding and Oxidation of Ti-6Al-4V Alloy*, vol. 382. 2018.

17. F. Mindivan and H. Mindivan, *Microstructure and Tribocorrosion Properties of Pulsed Plasma Nitrided Cast CoCr Alloy for Dental Implant Applications*. 2018. 39.
18. R. Wei, T. Booker, C. Rincon, and J. Arps, "High-intensity plasma ion nitriding of orthopaedic materials," *Surf. Coatings Technol.*, vol. 186, no. 1–2, pp. 305–313, 2004.
19. J. Lutz and S. Mändl, "Effect of ion energy and chemistry on layer growth processes during nitriding of CoCr alloys," *Nucl. Instruments Methods Phys. Res. Sect. B Beam Interact. with Mater. Atoms*, 267 (8-9) 2009, pp. 1522-1525.
DOI: https://doi.org/10.1016/j.nimb.2009.01.083.
20. J. Lutz and S. Mändl, *Wear Mechanism, Wear Rate and Contact Pressure in PIII Nitrided CoCr Alloys*, Plasma processes and polymers, 6 (51) 2009, pages: 565-569. http://doi.wiley.com/10.1002/ppap.200930309.
21. C.-H. Zhang, S. Zhang, H. C. Man, C.-S. Liu, and Q.-K. Cai, *Laser gas nitriding of Ti6Al4V alloy*, Journal of Optoelectronics Laser, vol. 15. 2004, pages: 946-950.
22. F. El-Hossary, N. Z. Negm, S. Khalil, and M. Raaif, *Surface modification of titanium by radio frequency plasma nitriding*, vol. 497 (1-2) 2006, pages: 196-202. https://doi.org/10.1016/j.tsf.2005.09.193.
23. P. Hovsepian, G. Thompson. B. Lewis, A. Ehiasarian, and W.-D. Munz, *Performance of High-Precision Knife Blades Treated by Plasma Nitriding and PVD Coating*, Proceedings, Annual Technical Conference - Society of Vacuum Coaters, 2003.
24. X. Luo and X. Li, "Design and characterisation of a new duplex surface system based on S-phase hardening and carbon-based coating for ASTM F1537 Co-Cr-Mo alloy," *Appl. Surf. Sci.*, vol. 292, 2014, pp. 336-344.
DOI: https://doi.org/10.1016/j.apsusc.2013.11.141.
25. T. Bell, H. Dong, and Y. Sun, "Realising the potential of duplex surface engineering," *Tribol. Int.*, vol. 31, no. 1–3, pp. 127–137, 1998.

26. R. Hutchings and W. C. Oliver, “A study of the improved wear performance of nitrogen-implanted Ti-6Al-4V,” *Wear*, vol. 92, no. 1, pp. 143–153, 1983.
27. A. F. Yetim, A. Celik, and A. Alsaran, “Improving tribological properties of Ti6Al4V alloy with duplex surface treatment,” *Surf. Coatings Technol.*, vol. 205, no. 2, pp. 320–324, 2010.
28. E. J. Mittemeijer, “Fundamentals of Nitriding and Nitrocarburizing,” ASM Handbook: Steel Heat Treating Fundamentals and Processes, vol. 4A, 2013, pages: 619-646.

Chapter 2

Literature Review

This chapter discusses the previous works done on the CoCrMo alloy to improve the load-bearing capacity using coatings and surface alloying techniques. This chapter is divided into two separate sections. The first section describes the basics of plasma and glow discharge, nitriding, plasma nitriding, types of plasma nitriding; and the advantages of using HIPIMS discharge to improve the nitriding process discussed in detail. The following sections of the chapter discuss in brief the possibility of employing various monolithic coatings such as CrN, TiN, NbN and their multilayer (superlattice) to enhance the corrosion, mechanical and tribocorrosion properties of the biomaterials.

2.1. Nitriding

The development of the nitriding process can be traced to the 19th century. The works of Adolph M. (1908) and Adolph F. (1922) improved the surface modification technology of steel. Later (1932), Wehnheldt and Berghaus presented a new model of the nitriding process of steel (ion nitriding). Nitriding is a very well-known process by which the atomic nitrogen diffuses into the steel. The important, often undisclosed aspect of the nitriding process is that it does not require phase change from ferrite to austenite or further from austenite to martensite [1]. Even after the nitriding process, steel remains in the ferrite phase with improved hardness and corrosion properties. It means that the crystal structure of the steel is still BCC (body centred cubic) lattice, and it will not grow towards face centred cubic (FCC) lattice [1]. Despite this, there was no change in crystal size and more importantly, no change in dimensions of the steel, only minor expansion in d-spacing of the steel matrix due to the nitrogen diffusion [1].

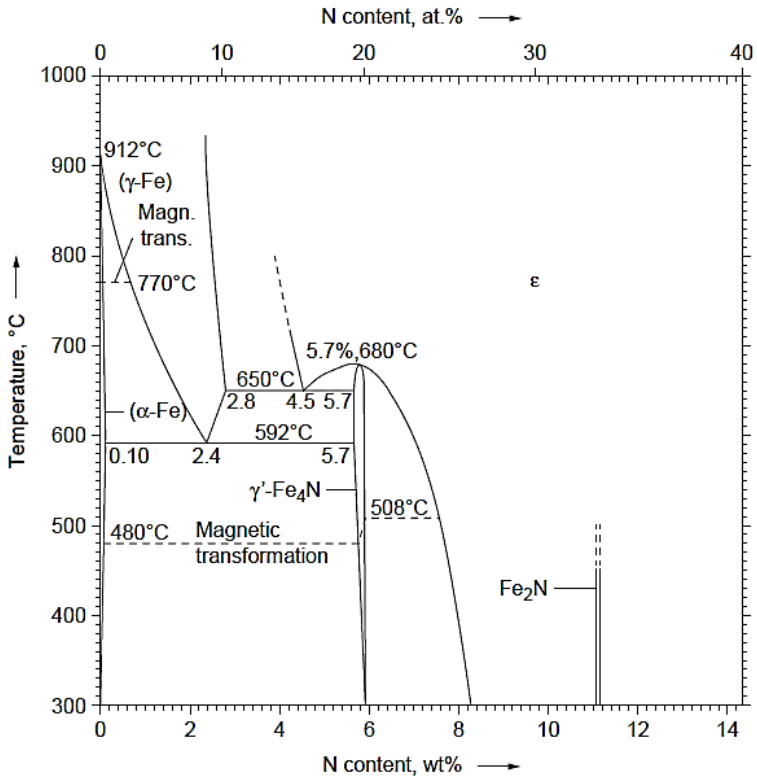

Figure 2-1: The equilibrium phase diagram of Fe-N [2]. Note: the behaviour of Co-N with temperature can be found here.

Diffusion of the atomic nitrogen into the matrix (SS or compound alloy) depends on the solubility of diffusing element into the matrix. The equilibrium diagram is the best way to understand the diffusion mechanism and change in phase of the alloys. For example, nitrogen solubility into steel depends on the temperature, and at ~450 ºC nitrogen diffusion in Fe base alloy is around 5.5 - 6.1 at.% as shown in figure 2.1. Beyond this temperature, the surface phase formation in steel alloys predominantly ferrite (ε) phase. As the temperature reaches 490 ºC, expanded austenite (γ') phase becomes dominant, and the solubility of nitrogen in steel begins to decrease at a temperature of ~680 ºC [1]. Nitriding process control factors are given below (Table 2-1), as suggested by David Pye (ASM International- Practical Nitriding and Ferritic Nitrocarburizing).

Table 2.1: Control factor affecting nitriding suggested by P Dye.

Base Pressure	Control of reactive gas
Chamber temperature or control over preheat treatment process.	Surface precleaning before nitriding process.

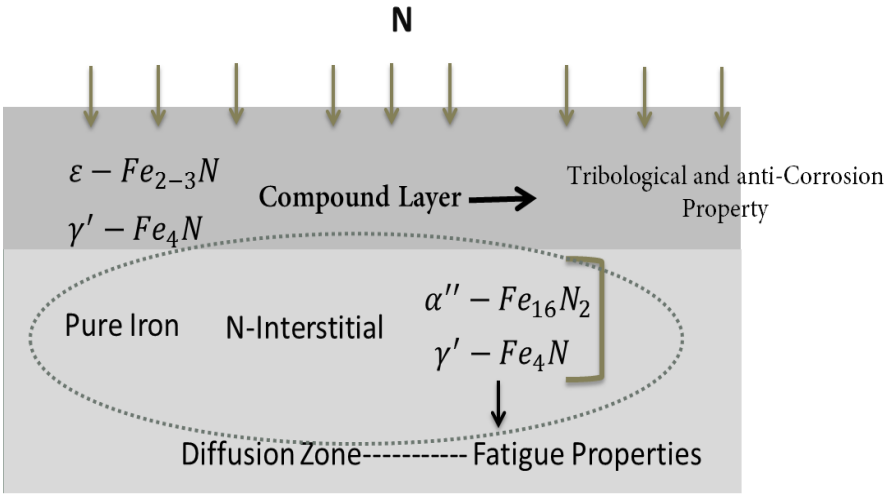

Figure 2-2: Schematic of compound layer formation in an austenite stainless steel [2].

Formation of a compound layer also called as $\mathbf{M_{(Fe,\ Co,\ Ni\ etc)2\text{-}3}N+M_{(Fe,\ Co,\ Ni\ etc)4}N}$, in the ferrite and austenite base alloy below 550° C can be divided into sub-sublayers and is shown in figure 2.2. A compound layer mainly consists of hexagonal closed packed (hcp) $\varepsilon-M_{(Co,\ Ti\ and\ Fe)2-3}N$, M sublattice and N more or less ordered in octahedral interstice and face centred cubic (FCC) ($\gamma'-M_{(Co,\ Ti\ and\ Fe)4}N$,), where M sublattice and N ordered in octahedral interstices. Whereas a diffusion layer is a mixture of Body-centred tetragonal ($\alpha''-M_{(Co,\ Ti\ and\ Fe)16}N_2$) nitrogen content, 12.5 at.% and Face-centred cubic ($\gamma'-M_{(Co,\ Ti\ and\ Fe)4}N$,) nitrogen content, 19.4 - 20 at.% where M sublattice and N are ordered in octahedral interstices [2].

The above explanation of the formation of a compound layer is valid for any type alloying techniques which are currently employed to perform the nitriding (carburising and boriding) process. Figure 2.3 depicts the possible techniques used at industrial scale to perform the

nitriding of stainless steel or compound alloys. However, the salt bath nitriding is excluded from the study, as the use of cyanide-based chemical is prohibited in the European region. Also, gas nitriding requires a long process time, which makes this technique very expensive for the industry to use.

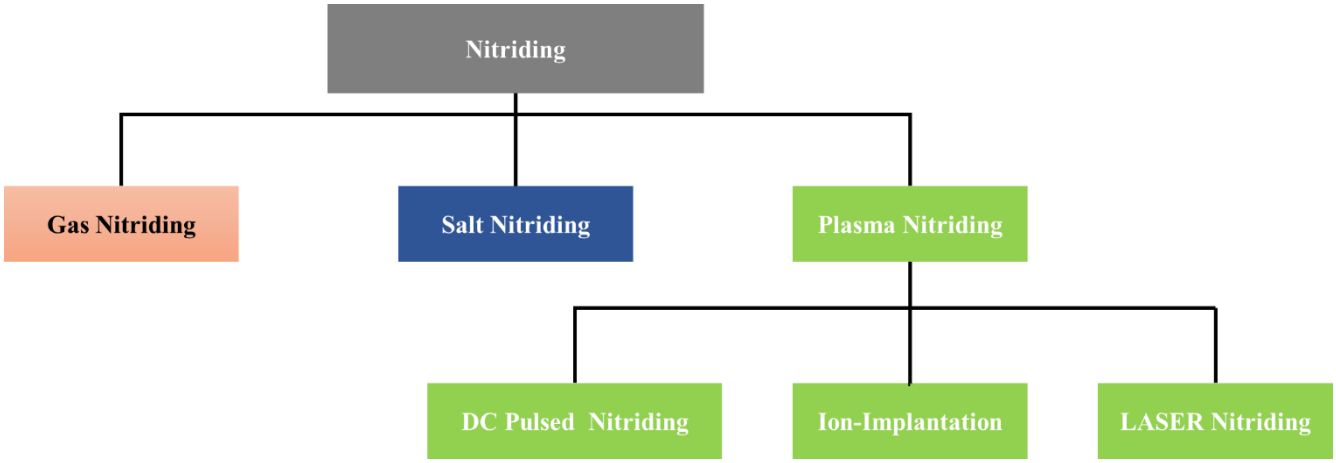

Figure 2-3: Flow chart of the surface alloying techniques currently used in the industry to perform nitriding of alloys.

2.1.1. **DC Pulsed Plasma Nitriding**

Plasma nitriding is a surface hardening technique using a low-pressure glow discharge plasma. A mixture of nitrogen and hydrogen gases is used for plasma formation so that nitrogen ions diffuse into the surface to form various nitrides. The formation of nitrides produces a very hard surface up to few micron depths. Hence this surface engineering technique is widely employed to improve the wear and surface hardness of steel and various compound alloys such as Ti, Co, Co-Ni alloy. The direct-current (DC) glow discharge is a simplest type of glow discharge. This DC glow discharge plasma is created by applying a potential difference between two electrodes. Because of the potential difference, the atoms of the discharge gas e.g nitrogen are ionised to produce free electrons and positively charged ions. The characteristics of the discharge depend upon different factors such as geometry of the electrode and vessel, gas used,

operating pressure etc. Typical current voltage characteristics of a DC discharge is shown in figure 2.4.

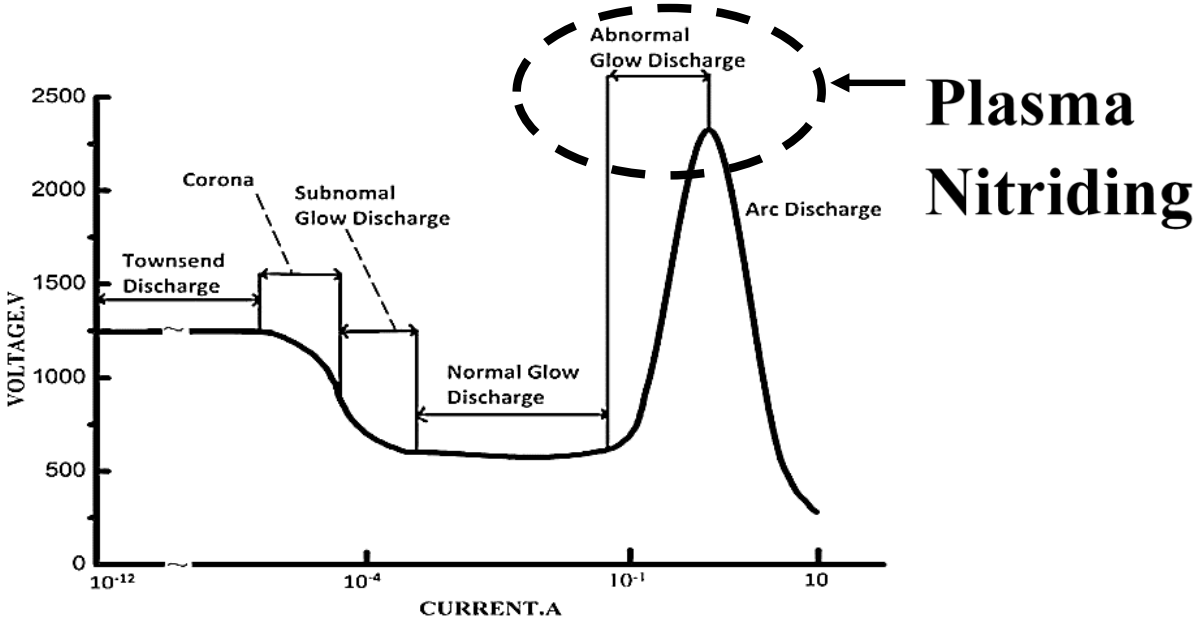

Figure 2-4: Typical characteristic current-voltage (I-V) cure of glow discharge. Figure adapted from Xu Z and coworkers. (2008) [5].

DC discharge can be classified into the various sections as per the current density. As it is already known that the no visible light can be observed in the vacuum diode at shallow current and voltage (dotted line in the figure); whereas voltage and current increases further the discharge stage to move from Corona followed by subnormal glow, normal glow, abnormal glow and arc discharges. Once the characteristic V-I curve crosses the normal glow discharge region, it jumps to the abnormal glow discharge where any change in V-I will not affect the behaviour of the glow discharge. At this point, total current density, J_t can be further increased by extra ionization using electric and magnetic fields which is ideal for magnetron sputtering techniques. This region is also used for the plasma nitriding or plasma alloying of the metal. Moreover, a further increase in V will lead to the arc discharge region where arcing on the target is frequent [6][7]. At the arc discharge region, the glow discharge collapses and high current density discharge forms.

To obtain the glow discharge, the high potential applied between the cathode (sample holder is also known as case holder, technical term) and anode (vacuum chamber). In plasma, the electrons are accelerated at high potential and collide with neutral Ar, N. The collision between electron and nitrogen has elastic behaviour at lower electron energy as for glow discharge, these collisions become inelastic. Due to this inelastic collision between gas molecules or atoms with an electron, results in their excitation. Therefore, various molecules spontaneously experience through one of the following processes (a) Transition of an electron from excitation states to ground state (b) dissociation (c) ionisation (d) recombination. During plasma nitriding, the first course is the interaction between ions and substrate material surface. The positive ions (Ar^+ and N^+ etc.) from glow discharge driven by electric field will bombard the substrate surface (cathode), resulting in various interaction effects depicted in Figure 2.5. However, this technique has various advantages over the conventional nitriding process such as

1) No need for surface finishing.
2) Faster diffusion of the diffusing species in the subsurface.
3) Due to high vacuum, no chance of surface contamination (no presence of oxygen, O_2 in the chamber).
4) Formation of a white layer can be minimised.
5) Layer thickness can be controlled.

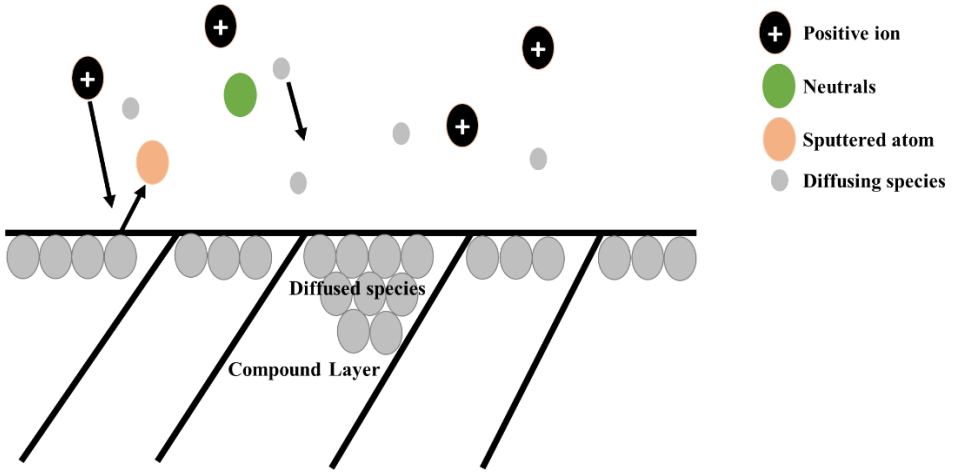

Figure 2-5: Schematic of ion-matter interaction adopted from [6].

2.1.2. **Laser Nitriding**

Nitriding based on laser irradiation has been employed to increase the wear and surface hardness of medical-grade alloys. Laser nitriding (LN) is similar to that of plasma nitriding (PN). In this technique, a pulsed laser beam continuously irradiated the surface in a nitrogen (N_2) environment (process gas can be changed depending on the alloying element) to form a hard nitrided layer or compound layer on the desired surface [8][9][10][11]. The high surface temperature and pressure allows decomposition of N_2 molecule to atomic nitrogen (N). At the same time, evaporated metal and gas-atoms will be ionised. During the lase irradiation, free electrons arise and can cause plasma shielding. This plasma shielding indirectly allows the absorption of the laser beam in the plasma and causes further heating of the plasma.

In the past few decades, various researchers have attempted to improve the tribological and surface hardness of the medical grade alloy using laser technology. By using a high power CO_2 laser, they managed to obtain a thick compound layer of about 100 micrometres [8]. The process of formation of a thick compound layer is mentioned below by considering the surface

temperature below the evaporation threshold. For example, the process of laser nitriding of CoCrMo alloy can be described as.

$$[Co] + N_2 \rightarrow [Co] + [N_2] = Adsorption\ process$$

$$N_2 \rightarrow 2[N] = Dissociation\ Process \qquad \textbf{Equation 2-1}$$

$$[N] on\ surface \rightarrow N\ diffusion$$

The use of such technology also requires understanding of the parameters such as spot size (D_s), laser power, lateral shift (d), scan number (n) and scan velocity (v_s). Also, it is crucial to choose an adequate operation mode of the laser (continues wave or pulsed). Usually, in continuous wave mode, the scan velocity is a critical parameter which needs to be considered carefully, whereas, in pulsed laser mode, the laser frequency (f) is a crucial parameter. It is considered that the intense irradiation melts the surface and allows the alloying element to diffuse within the matrix. As a result, a fast dissolution of alloying element into the matrix occurs which is one reason for achieving a thick compound layer in less process time (~ 100 mms^{-1}). As a result, cracking within the formed layer can be seen as a major issue in this type of nitriding process. However, this can be minimised by varying the various parameters mentioned earlier in the section.

This technique has been widely applied to increase the surface hardness, corrosion resistance, and tribological properties such as the wear of stainless steel (SS) [8][10] and Ti alloys. Katayama and co-workers (1983) [9] managed to nitride Ti alloy using a solid-state laser (Nd:YAG). They found that the microhardness of TiN layer formed on the surface can be varied (up to 1700 HV) by simply increasing the number of shorts (pulse duration of 3.5 ms with 1.06 µm wavelength). On the other hand, a thick TiN layer was observed on the surface treated using CO_2 laser (operating in continuous wave mode), whereas the surface was rougher compared to that of solid-state laser [9]. Walker and co-workers (1985) performed similar

experiment on both commercially pure (CP) Ti and Ti-15Mo alloy using CO_2 (continuous wave mode) laser. Here, they found that the dendrites based on TiN are responsible for the high hardness (up to 1000 HV) [11]. Comparative work presented by Bell and co-workers (1986) indicates that using the laser nitriding technique a thick nitrided layer consisting of TiN-Ti_2N can be achieved compared to that of plasma nitrided at high temperature. Also, hardness profiling of the formed layer at a fixed load of 25 gram shows the specimens treated using laser nitriding (1400 HV) were harder than that of plasma nitriding (~ 1200 HV, 12 hours at 850° C) [8].

2.1.3. **Ion Implantation**

Ion implantation is another very important technique been that has been used to enhance the surface properties of the bulk material [12] [13]. Origin of the technique can be traced back to the early 1960s where ion source was used to study the propulsion mechanism in space engines. At this time, the technique was employed to improve the corrosion and mechanical properties of the materials as well as for doping of semiconductors in microelectronics. Ion beam implantation uses directional high energy ions in the range of 10-300 keV capable of penetrating below the surface of the substrate or workpiece. The sufficient penetration depth can be varied from a few nanometres (nm) to a micrometre (μm) merely by changing the ion beam current. Mechanism of ion implantation can be understood from figure 2.6 [7].

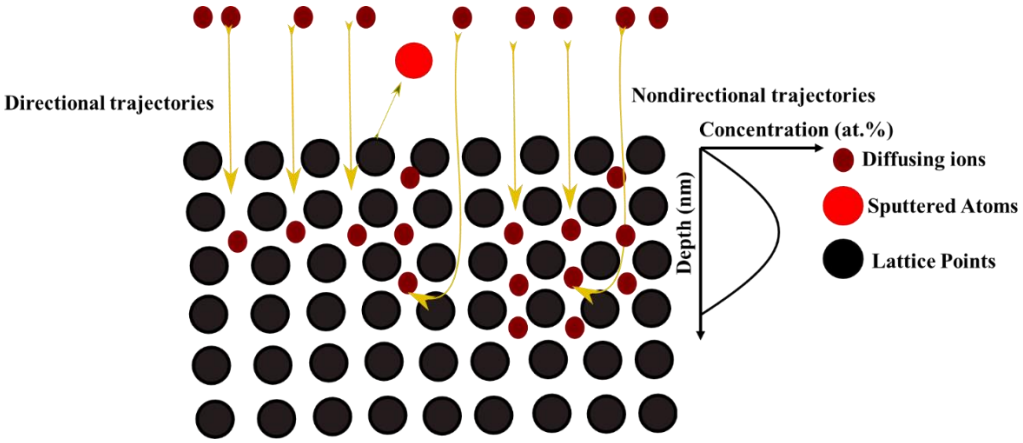

Figure 2-6: Schematic of diffusion of alloying species using ion implantation technique in a crystalline material. (picture was adopted from J. Rethe books, volume 2) [7].

Positive ions directed onto the substrate surface by applying high electric potential through the chamber under high vacuum in a directional manner. Some of these ions travelled straight (channelled trajectory) and collided with lattice and diffused very deep in the matrix (no barrier within the lattice), whereas a few of them travelled in a non-directional manner (dechannelled trajectories) due to defects present in the lattice. At the same time, sputtering of passive layers adsorbed on the substrate surface (degassing) also occurs similar to that of ion etching of the surface and reaches the desorbed state quickly. This state is achieved in time comparable to that of plasma-wall interaction predicted using equation. However, it is ideally desirable to avoid sputtering of the surface during the doping or alloying process (diffusion of N/C etc.) which is measured as number of atoms per ions (sputtering yield). Sputtering can be avoided simply by changing various parameters such as ion beam energy, tilt and twist angle and implantation dose [7].

On the other hand, this technique allows the formation of a diffusion layer (without precipitating Cr) within the metal matrix similar to that of PN and nitriding process [13]. The microstructure and phases formed during ion implantation can be directly correlated with the data obtained from PN alloys. C. Blawert and co-workers, (2000) reported the formation of S-phase or expanded austenite in austenite stainless steel (ASS) using plasma ion implantation

and immersion ion implantation (I^3) for the first time (400° C) [14]. This work was done under both nitrogen, N and carbon, C environment, which leads to the formation of a duplex layer. The top layer (about 3 µm) consisted of purely nitrogen-based compound layer, whereas the layer based on C was observed much more in-depth (up to 13 µm). From here, a conclusion can be drawn that the diffusion of C in ASS is faster than that of N. Similarly, many researchers have used this technique to enhance the corrosion and wear properties of the untreated CoCrMo alloy at elevated temperature. D. Ikeda and co-workers (2002) reported that the corrosion resistance of the untreated alloy could be improved by using appropriate combinations of the parameter. Here, they also measured lower friction coefficient (µ) for the implanted specimens than that of untreated CoCrMo alloy [15]. Whereas Bruce and co-workers (2004), found that the composition of the nitrided layer formed on CoCrMo alloy using ion nitriding can be modified with change in temperature and the dose of ions (intensity of ionisation) [16]. On the other hand, Orhan O. and co-workers (2006), found that S-phase (γN) can be formed at a low process temperature (400° C) using plasma ion implantation. But, the formed layer is not effective in minimising the ion release into simulated body fluid (SBS) as compared to that of the untreated specimen [17].

Apart from all the mentioned advantages, ion-implantation technique is not viable for industrial-scale for various reasons which makes this technique not suitable for large scale processing. Also, it is costly and hard to maintain [12].

2.2. Physical Vapour Deposition (PVD)

PVD techniques have been utilised to deposit hard and functional thin film coatings on various substrates in the range of a few nanometres, nm to 100 µm to improve the surface properties. PVD technique is a green technique which has no adverse effect on the environment and promises a wide range of applications based on three simple steps mentioned in Figure 2.7.

The difference between all PVD techniques is the source of vaporisation of bulk metal to deposit the material onto the substrate such as sputtering and evaporation. However, all these techniques follow three fundamental steps mentioned in the figure 2.7.

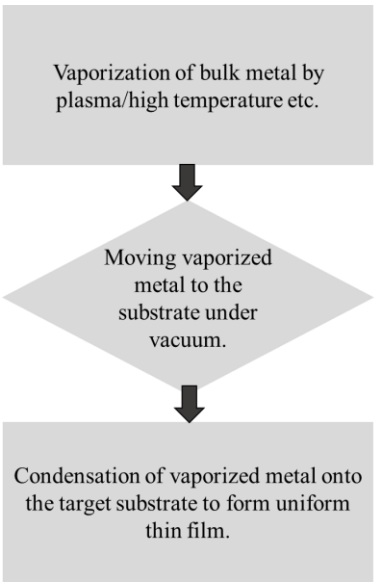

Figure 2-7: Depicts the fundamental steps in the PVD process.

2.2.1. **Evaporation technique:**

2.2.1.1. Thermal Evaporation:

In the last two centuries, the deposition method evolved from non-plasma to plasma assisted techniques and some of these require vacuum to mobilise the atom from the source to the surface of the host substrate. In the early 20th century, industrial-sized evaporation systems which can withstand high temperatures were developed. Such systems depend on placing the substrate in a large vacuum chamber at a process pressure lower than 1.3×10^{-5} mBar. At this pressure the mean free path, λ of an individual atom is somewhat close to or higher than the dimension of the vacuum tank. As earlier described, the bulk metal used as evaporant is heated in an electrically resisted crucible refractory above the melting point of the metal. At this point, atoms evaporate at a specific rate and forms a uniform coating to a desirable thickness on the

substrate, including the interior of the vacuum chamber [7]. For example, to deposit aluminium onto the substrate requires heating at or more than 933.52 °C (to evaporate). In this technique, the vapour pressure of specific molten evaporant can be calculated using the *Clausius-Clapeyron equation* which uses the atomic number, (Z), atomic weight, melting temperature, boiling point in kelvin (K).

$$\frac{dp}{dT} = \frac{pH}{RT^2} \qquad \textbf{Equation 2-2}$$

Where, P is the pressure in Pa, T is the temperature in K, R is the gas constant, and H is the latent enthalpy (per mole). Further, the above equation can be rearranged in to,

$$\frac{dP}{P} = \frac{HdT}{RT^2} \qquad \textbf{Equation 2-3}$$

Therefore, after integrating both sides of the equation considering the pressure and temperature of the evaporant,

$$p = Ce^{(-H/RT)} \qquad \textbf{Equation 2-4}$$

Here, C is the constant for a given pressure and the material used as an evaporant.

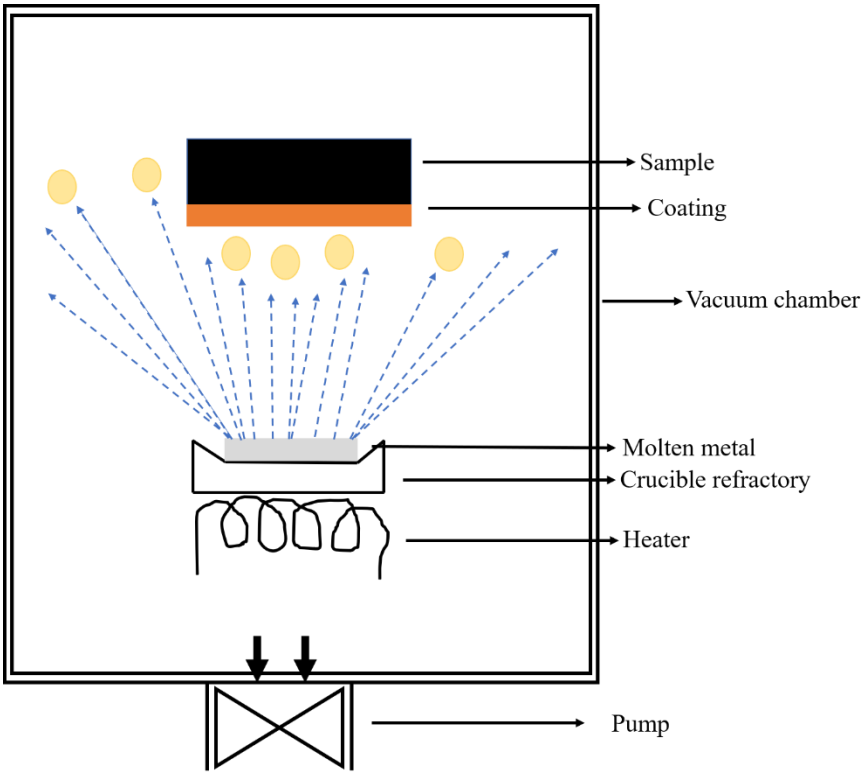

Figure 2-8: Illustrates the working mechanism of industrial-sized thermal evaporation machine [7].

2.2.1.2. Electron (e-) Beam Evaporation:

Like thermal evaporation, e- beam technique also works below 1.3×10^{-5} mBar pressure where the λ of an atom is equal or greater than the size of the chamber. In e- beam technique shown schematically in figure 2.9, the bulk metal is heated using the high energy e- beam produced by electrically charged filaments placed beneath the electrically insulated crucible refractory. The magnetic field of about 10 mT below the crucible allows the emitted e- accelerated in a curved manner (270˚) which allows these e^- to gain energy before they reach the molten metal which also serves as the anode in the system. For the magnetic field source placed below the crucible evaporant both permanent magnets and electromagnets can be used. However, various e- beam deposition machines prefer electromagnets as it allows to change the magnetic field and gives the freedom to move the e- beam on the surface of the molten metal. The applied voltage in this technique can be varied from few kilovolts, kV to a few tens of kV (crucible evaporant is kept at ground) [7].

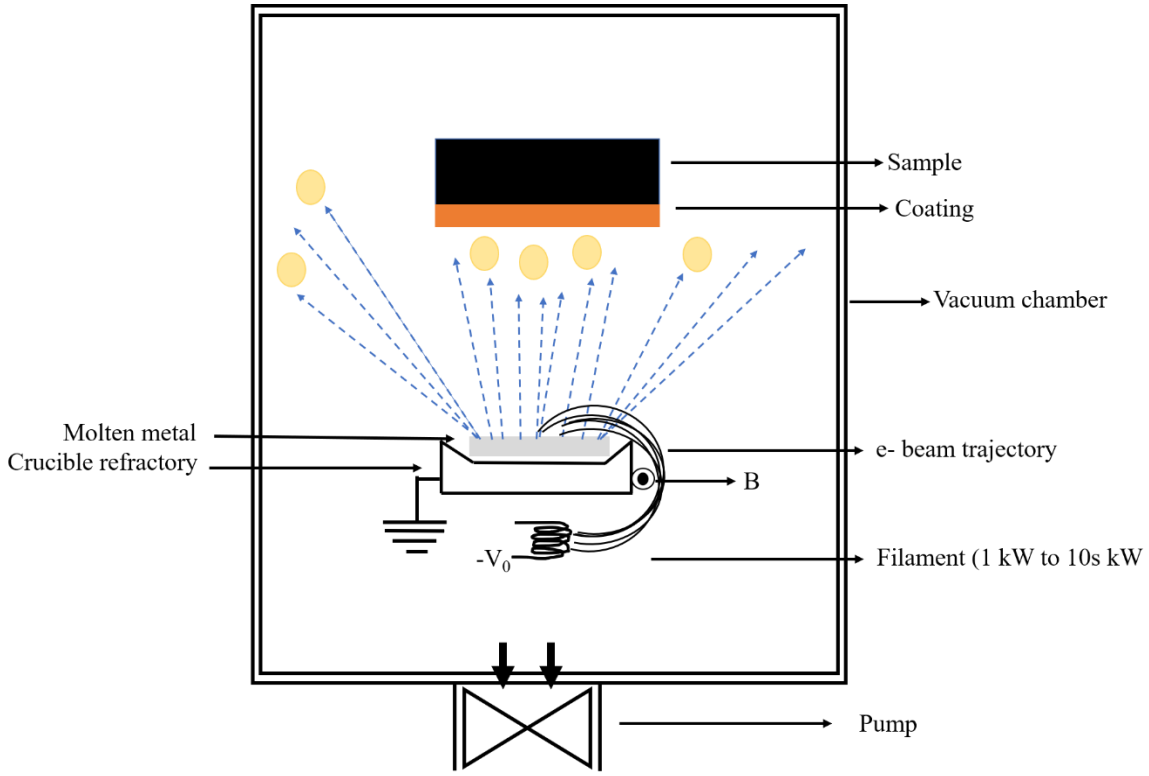

Figure 2-9: Illustrates the working mechanism of an industrial-sized electron (e-) beam evaporation machine [7].

The radius (metres, m) of the curvature of the e- beam can be calculated using the equation shown below.

$$R = \frac{mv}{qB} \text{ (m)} \qquad \textbf{Equation 2-5}$$

Where, v is the velocity of the e^- in the applied magnetic field (B) is written in terms of energy, E (eV) and m is the mass of the e^-.

$$v = \sqrt{\frac{2eE}{m}} \text{ (ms}^{-1}\text{)} \qquad \textbf{Equation 2-6}$$

After substitution of equation 2-5 into equation 2-6 gives the equation of R (m).

$$R = \frac{1}{B}\sqrt{\frac{2mE}{e}} \text{ (m)} \qquad \textbf{Equation 2-7}$$

Ideally, the required B is around 10 mT and the power dissipated in e- beam evaporation deposition machine is in between few kilowatts (kW) to a few tens of kW. Such systems are

commercially available to deposit uniform reflective and electrically insulated (ceramic) coatings on a variety of substrates [7].

2.2.2. **Sputtering Yield (S)**

By definition, sputtering is a process based on a loss of surface atoms from the solid material (acting as a cathode) due to the bombardment of high energetic ions, and in some cases neutrals [7]. The removal of surface atoms depends on the various parameters such as sputtering yield (S), power used, pressure etc. Sputtering yield (S) can be calculated using the equation below,

$$S = \frac{Number\ of\ atom\ removed}{Number\ of\ incident\ ions\ bombarded} \qquad \textbf{Equation 2-8}$$

Where S depends on mass of the incident ion (M), the energy of the incident ion (E_i), crystallinity of the target material, the atomic weight of the target material, angle of incidence of the incidence ions on the target surface [7].

In sputtering, the contribution of electrons is negligible due to their mass and neutrals are not energetic enough to sputter under the industrial environment. However, high energetic ion bombardment (high S) makes this technique of industrial interest. There are various sputtering techniques used in industry such as Magnetron Sputtering (MS), Pulsed Plasma Sputtering (PPS) and High Impulse Power Magnetron Sputtering (HIPIMS).

2.2.3. **Magnetron Sputtering**

First, sputtering phenomena was reported in the early 1800s where researchers used optical emission to investigate the shift from constant glow discharge to arc discharge and the type of metal atom removed from the target surface. In the year 1883, Michael Faraday experimented to understand the optical and electrical characteristics of glow discharge where he unintentionally deposited thin film on a glass chamber [18]. Later, 1857, he published a paper on the optical properties of the vacuum arc deposited film. In the same year, Heinrich

Geissler [19] used a mercury pump to generate a vacuum in a glass tube to study the optical properties of glow discharge. They found that the colour of glow discharge changes with the decay of the ionised gas. Before this, William Grove (1852) [20] published a paper discussing the deposition of metal and ion etching. In his experiment a steel needle was used as the cathode and a silver-plated substrate was used. However, the deposited layer was initially found to be iron oxide and reported to be reactive sputtering (oxygen present in the glass tube). Later, in the same experiment he changed the polarity of the cathode and anode to observe the ion etching phenomena where he found that not only was iron oxide removed, but it also removed the substrate atoms (reported as molecular disintegration) [18].

In 1858, Professor Julius Plucker from the University of Bonn observed the luminous region (green colour) on the cathode and in the same experiment he found that the position of the luminous region could be deflected by changing the magnetic field [21]. Arthur Schuster modified the setup proposed by Crook's experiment by placing the plates parallel to cathode and potential applied between them. He experienced that the particles (originally mentioned as cathode rays) were shifted towards the positive side of the setup which confirms that they are negatively charged [18]. Albert Hull (1921) presented a new vacuum devised setup, which he described as a magnetron. In this setup plasma was confined by controlling the electron behaviour using magnets placed behind the metal target (electrons trapped within the magnetic field to form race track). His discovery showed that the current flow through vacuum tube between cathode and anode is not affected by B up to certain critical point but falls to zero after an increase in the magnetic field beyond the critical point [22].

In the 1930s, Frans Penning presented a most compatible condition for magnetron sputtering, which considers the closed electric- and magnetic- field ($\bar{E} \times \bar{B}$) traps also known as Lorenz force which allows the increase of the plasma density at the cathode (target). At the

same time, he also observed that the generated secondary electrons from the target were in result of Lorenz force initiating the cycloidal spin on the target. These electrons lose a small fraction of the energy during their 1st orbit by direct collision with ions and neutrals in plasma which makes it impossible to return back on the cathode (against the electric field, $\bar{E}$) and they continue their cycloidal movement within the closed-field trap ($\bar{E} \times \bar{B}$). In later years, he realised that by minimising the magnetic field strength in the plasma allows ions in the discharge to travel towards the anode (e- trap within the closed-field). Which means $\bar{E} \times \bar{B}$ stops electrons to travel to the anode and makes them participate in the ionisation [18][22][23][24][25][26][27]. In 1940, Penning and Moubis presented the first magnetron sputtering setup where they placed a magnetic field parallel to the cylindrical glass chamber. This setup clearly showed that the plasma could be confined close to the copper target with ~1 mm thick collisionless discharge sheet [18][28]. Also, they managed to calculate the sputtering rate of the metal by measuring the mass of the substrate (mica). It was the first setup in which the target was cooled during the experiment, and this setup is still used in magnetron sputtering technique to avoid target meltdown. Penfield and Thornton were the first to describe the industrial-scale magnetron sputtering (inverted) system to deposit thin films on substrates of large area (longer than 1 m). Such setup was primarily designed to deposit Chromium (Cr) on silicon to function as a photomask [29].

2.2.3.1. Planar Magnetron Sputtering:

The earlier developed magnetron sputtering machine was able to improve the ionisation efficiency due to use of transverse $\bar{B}$ (orthogonal to $\bar{E}$). Unfortunately, this setup only allows confining the glow discharge near the cathode. Considering the issue, Rokhlin (1939) [18][30], suggested the use of a magnetic field applied parallel to the vacuum chamber (radial symmetry) with strong transverse component of $\bar{B}$. This configuration was later called closed-field magnetron sputtering. Such a setup was first used to deposit a thin film in year 1963 by Kay

[18][31]. He observed that the ion current density, Ji was increased significantly at the cathode (Aluminium target). The resulting increase in the sputtering rate of the Al indicating the positive impact of closed-field configuration (CFC). Approximately six years later, Mullaly also found that using the quadrupole magnetic field, the sputtering rate of the material can be improved. Interestingly, in both cases the circular racetracks were formed on the used target due to target erosion.

The first commercial parallel plate (CPP) CFC reported and later patented by John Chapin, 1979, where he proposed rectangular shape target considering the cooling of the magnetron. In this case the racetrack of the eroded area of the target was rectangular in shape. As per the claim, the $\bar{B}$ on the target forms the closed loop which forms the endless track (magnetic bottle) which traps the electron [18][32].

A review article published in the year 1978 by Robert Waits pointed out the drawback of such a configuration. Based on the above-mentioned setup, only a small fraction of the cathode is utilised resulting in waste of the material of about 67 %, initially, it was around 75 %. This was only achieved by rearranging the magnetic field which resulted in opening of the racetrack [33]. Later, W. de Bosscher and co-workers, 1999, used the advantage of permanent magnets and designed a system which can be initially rotated in a circular path during the experiment to utilise the maximum area of the target. Further they also rotated the magnet assembly to a very complicated path to achieve the target utilisation of around 60 % [34].

2.2.3.2. Unbalanced Magnetron Sputtering (UMS):

The magnetron sputtering, MS Setup proposed by John Chapin had some limitation in terms of control of the film microstructure/phase composition, favourable orientation, physical/chemical properties, surface roughness and density of the film as it becomes difficult to provide enough low-energy high flux ion bombardment onto the substrate. After a decade,

Brian and co-workers proposed a setup which had a similar magnet arrangement but different in strength. Here, they simply found that by rearranging the magnets (stronger magnet outside and week magnet inside) as shown in figure 2.10a, the magnetic field can be unblanced. The stronger magnet outside allows a small leak in glow discharge trapped at the cathode. As a result, permitting low energy ions to bombard the desired substrate. However, researchers found that this setup also has some drawback such as loss of electron and ions to the chamber (bombarding). Later, a researcher at university of Illinois in 1992 presented new architecture of UBM with a set of Helmholtz coil (external magnetic field controlled by applied current) to control the unbalancing of the magnetic field circuit by applying axil magnetic field using the coils as shown in the figure 2-10. Such arrangement minimises the loss of ions and electron without altering the sputtering rate. Presently, UBM is widely employed in industry to deposit various coatings [35][36][37].

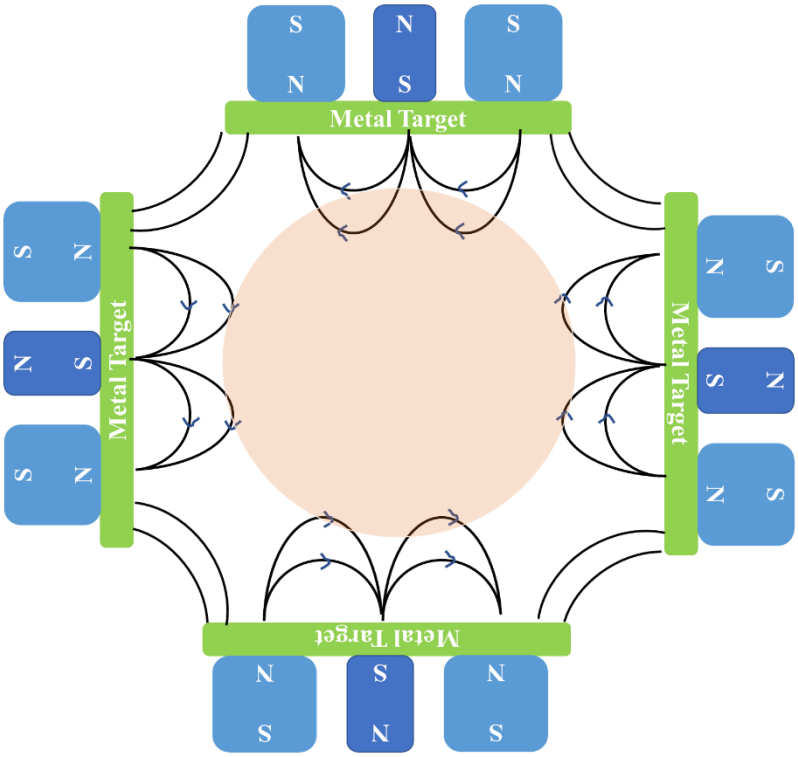

Figure 2-10: A schematic of the magnet arrangement and magnetic field lines in closed field unbalanced magnetron sputtering configuration.

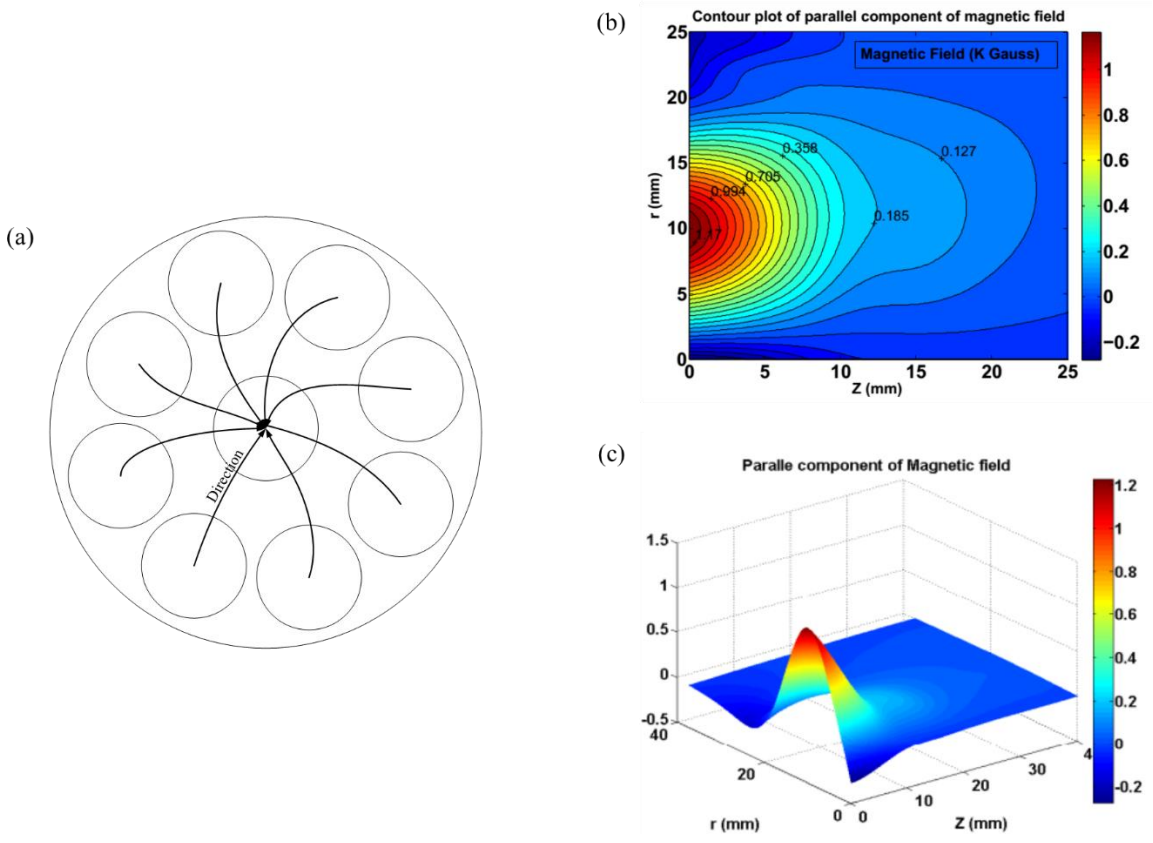

Figure 2-11: (a) Magnet arrangement in UBM (b-c) magnetic profile of UBM.

2.2.3.3. HIPIMS Coating

High-Power Impulse Magnetron Sputtering (HIPIMS) technique is a surface modification technology originally developed at Sheffield Hallam University. HIPIMS technology combines the magnetron sputtering (MS) with pulse power technology, where power is applied in pulsed mode at a relatively high amplitude and low duty cycle. The majority of sputtered atoms and near target gases such as argon (Ar), N etc. are ionised. Also, it is often argued that the power density in HIPIMS (near the target region) can exceed 10^7 Wcm^{-2} which is impossible to obtain in traditional direct current magnetron sputtering (DCMS). Although, at this level of glow discharge arcing on the cathode surface (target) is very common and requires a special arc suppression unit. Arcing on the target might damage the quality of the coating (microdroplets) [38][39]. However, this technology is already equipped with arc

detection and suppression unit which interrupts the process for a short period whenever arc is detected. The advantage of using HIPIMS technology is it can produce plasma with high metal ions density of about 70 % or higher for some material such as titanium (Ti) and copper (Cu) with high ion energy in the range of 20-200 eV compared to that of conventional MS (direct current) [38][39].

On the other hand, HIPIMS has a lower deposition rate compared to that of DCMS due to re-sputtering of initially sputtered metal ions. Nevertheless, sputtering rate can be improved by combining UBM and HIPIMS or by applying a magnetic field less than 40 milli tesla (mT). Ehiasarian, A.P and co-workers (2003) applied HIPIMS technology to improve the durability of a surgical blade. Here, they found that it is possible to plasma nitride using HIPIMS discharge combined with UBM by varying the bias voltage (Ub) from -500 V to -1000 V, whereas no evidence of S-phase formation was reported. It could be linked to the high amount of ion bombardment, which leads to the localised heating of the specimen surface [40]. As earlier discussed in the section, the composition of a compound layer is sensitive to temperature which means temperature > 450° C promotes the formation of a layer consisting of Cr precipitation and below 450° C it consists S-phase. So, it is crucial to consider appropriate Ub to plasma nitrided austenite alloy or ASS.

2.2.3.3.1. Nanostructured Coatings

Titanium nitride (TiN)

Titanium nitride (TiN) is extensively used to modify the surface of implant materials such as Ti alloy, CoCr alloy and biocompatible steel like AISI 316L and has a golden appearance. TiN coatings are considered to have ceramic characteristics of hardness in the range of 24-26 GPa, low wear coefficient, high wear resistance and excellent corrosion resistance against aggressive environments such as simulated body fluid (SBF), saliva, etc.

I Dion, 1992, found that TiN has blood tolerability properties with the haemolysis very close to zero. Considering, this the TiN coating was used to modify the surface of such as ventricular assist devices and pacemakers [41]. In 2008, Cogan and co-workers applied this coating on the of chronic electrode implant to study the injuries to the spinal cord. It was suggested that by depositing TiN, CoCrMo alloy has potential application in the fabrication of prosthetics and dental implants. It can reduce the release of metal ions such as Co, Cr and Mo into the human body which have severe side effects once they reach maximum concentration. For example, carcinogenic effects in human body can be seen if Co metal ions are released in the quantities of more than 25 ppm [42]. For the first time, TiN was used to modify the surface of joint implants to reduce the wear resistance and the release of metal ions; this technology was patented in 1997 [43].

The property of such coating also depends on the method of coating deposition. In standard DCMS, TiN was always found to have a columnar structure which makes this coating difficult to survive in the highly corrosive environment. The columnar structure allows the ions, for example, Cl^- (human blood contains, 0.9 % NaCl) to travel through the gap between columns. Such example is presented in figure 2.14. R. Machunze and co-workers, 2009 observed that the film grown on a silicon substrate using DCMS shows the variation in residual stress. Observation shows that a film of about 0.53 μm has a higher compressive stress (-1.4 GPa) than that of a thicker film (1.63 μm, -1.0 GPa) [44].

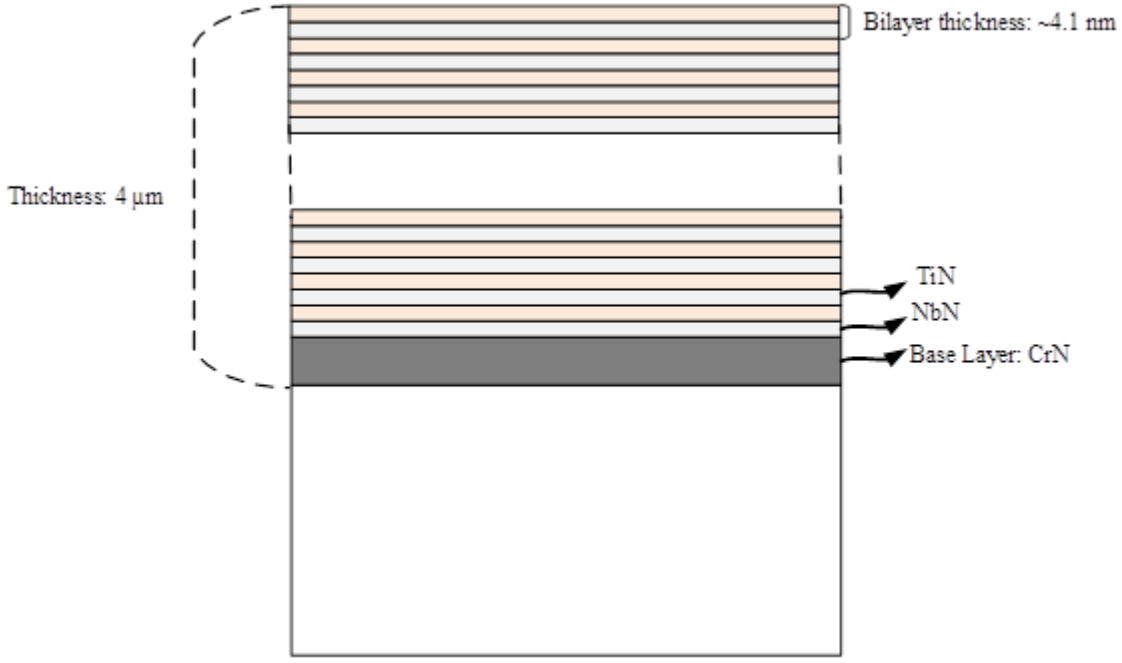

Figure 2-12: Schematic of nanostructure multilayer coating.

In the same year, R. Machunze and co-workers demonstrated that if the TiN films grown using HIPIMS discharge without substrate biasing will promote films with lower compressive stress (thin TiN: -2 GPa and Thick TiN: -0.5 GPa). On the other hand, film grown with an applied bias voltage (-125 V) shows very high compressive stress of about -4 GPa. However, film grown using -125 V bias voltage had very dense microstructure than that of the film grown under no biasing (voids between columns were observed where average width of the grain was 18 nm) [45]. Papken Hovsepian and co-workers, 2014 showed that the residual stress (-0.22 GPa to -11.62 GPa) and texture can be controlled by varying the parameters of the unbalancing of magnetic strength, bias voltage. Also, the density of the coating can be changed by using a combination of UBM and HIPIMS. For example: pure columnar structure can be obtained by using 4 UBM to dense structure by using 2 UBM and + 2 HIPIMS [38]. J. Böhlmark and co-workers, 2006, were the first to present the comparative study on DCMS, Arc sputtering and HIPIMS. Their study showed that TiN coatings obtained from DCMS were full of defects and had a pyramidal columnar structure from the top and the surface of coating produced by Arc sputter specimen was found to have cauliflower-like structure. On the other

hand, TiN deposited using HIPIMS had a fine grain and dense structure. This shows the HIPIMS is capable of producing coatings without droplet and other defect [46].

Chromium Nitride (CrN):

CrN is second most used coating after TiN because of its high resistance against oxidation, better wear resistance, superior hardness and high resistance against corrosion. However, the hardness of the CrN coating which is in the range of 15-20 GPa is lower than that of TiN. CrN has two stable forms i.e., CrN and Cr_2N. CrN is mainly had *face-centred cubic structure* (FCC) and Cr_2N has a *base centred cubic structure* (BCC) which makes Cr_2N phase harder than that of CrN. Extensive studies on CrN coatings demonstrate that a layer of about 3 μm is mostly not helpful in providing protection against corrosion and improved wear resistance compared to that of hard chrome coating (Cr). This could be due to the porosity of CrN coating (disadvantage of DCMS). CrN coating is widely chosen because of better adhesion to stainless steel and even on electroplated substrate [47].

Studies show that the hardness of CrN coating can be improved up to 30 GPa by using bias voltage (-200 V) and extreme target poisoning conditions using high nitrogen flow [47]. Recently, researchers [48] found that the CrN deposited by DCMS contains (111), (200) and (220) phase, whereas the same coating deposited using HIPIMS technique produced a layer that has intense (200) texture (T*). Coatings deposited using DCMS had clear formation of columnar structure along the growth direction, but HIPIMS deposited CrN was dense despite a columnar structure. CrN coating demonstrates the excellent resistance against corrosion or mechanically assisted corrosion (tribocorrosion) [49].

Multilayer coatings

To improve the load bearing capacity of the biomaterial alloy such as CoCrMo, multilayer coatings such as TiN/NbN, TiN/CrN, TiN/VN and CrN/NbN have been used as they have better wear resistance, superior hardness and excellent corrosion resistance. For the first time such coatings were presented by researchers at University of Illinois in 1987 where they managed to grow a single crystal TiN/VN superlattice coating on MgO (100) substrate using sputtering technique. Their observation shows that the hardness of the coating is a function of bilayer thickness (λ). The highest hardness was around 5560 HV measured for λ= 5.2 nm [50]. Later, Cho et al., 1992 developed superlattice coatings based on TiN/NbN using a rotating substrate holder. In this study they found that the hardness of the coating changes with change in bias voltage and N_2 flow ratio while bilayer period thickness is fixed. The highest hardness of 4900 HV was measured for λ = 24 nm (which was achived at bias voltage=-150 V and N_2 flow for Nb:Ti = 2:1) [28]. Another similar work presented by this team found that the surface microhardness of the superlattice coating, like TiN/NbN, can be influenced by various parameters such as bilayer period thickness, bias voltage, N_2 partial pressure and gas flow ratio. Also, in the same study it was reported that the phase composition depends on the bilayer thickness. For example: mixed (111)/(200) phase for λ= 2.5 nm to preferred (111) phase for λ= 25 nm [51].

In 1995, Hurkmans and co-workers reported a new set of multilayer coatings based on TiN and W_2N superlattice where the thickness of the layers were in the range of 2.45 nm to 17.5 nm. They found that with the proper combination of N_2 partial pressure and satellite rotation frequency (single or 3-fold), highest hardness of about 30 GPa and very high critical load (around 60 N) with minimum residual stress (1 GPaμm^{-1}) can be achieved [52]. A year later, Setoyama and co-workers, 1996 reported a unique set of coatings developed using Ti and

Al targets. During this work TiN/AlN superlattice coatings were deposited using Arc ion-plating technique where period thickness was varied from 1 nm to 35 nm. Here, they found that AlN crystal structure changes from Wurtzite type to NaCl (FCC) type at 2.5 nm period thickness which further changes from FCC-type to mixture of cubic and wurtzite (AlN) at 35 nm period thickness. Interesting observation in this work was that the hardness of the superlattice coating reached 41 GPa which was almost 1.6 times higher than that of monolithic TiN coating [53].

In 1998, Nordin and co-workers deposited different combinations of multi-layered coatings based on CrN, MoN, NbN and TaN where TiN was common in all. All multilayer combinations showed (200) phase as a preferred orientation except one MoN . TiN/MoN coating found to have mixed orientation of (111), (200) and (220) phases. Another interesting observation in this work was the thickness of the column. The thickest columns were found in TiN/NbN, TiN/TaN and monolithic TiN, whereas the thinnest columns were observed for TiN/CrN and TiN/MoN. Important observations made during this work was that mechanical and tribological properties of the coating depends on the phase composition of the coating system rather than the type of the combination [54].

Early in 2000, Papken Hovsepian and co-workers reported four different combinations of superlattice metal nitrides such as TiAlN/CrN, TiAlYN/VN, TiAlN/VN and CrN/NbN. Before depositing superlattice coatings, substrate surfaces were exposed to intense metal ion bombardment (metal ion etching) followed by deposition of CrN base layer. During this work, they found that using specific metal ion etching (V, Cr and Nb) before deposition improves the adhesion significantly. In this work it was also reported that the residual stress of the coating can be altered by changing bias voltage (-75 to -120 V) where maximum compressive residual stress was reported for TiAlN/CrN which was -9.2 GPa. TiAlN/VN was found to be with the

lowest coefficient of friction, CrN/ NbN showed the best corrosion resistance where as TiAlN/ CrN and TiAlYN/CrN showed the best micro abrasive wear resistance, [55].

D.C. Cameron and co-workers, 2001, shown that by varying the substrate position and substrate bias voltage the optimum hardness of superlattice CrN/NbN can be achieved [56]. Later in 2004, E. Bemporad and co-workers, deposited the same coating on steel to improve the wear resistance in an industrial scale PVD machine. The result shows that the lifetime of the substrate material was increased significantly up to 6 to 11 months compared to that of monolithic CrN coating [57].

In 2008, Hovsepian and co-workers [58], presented new nanoscale multilayer coatings based on CrN and NbN deposited using combined UBM and HIPIMS. Study shows that the coating with bilayer thickness of 4.1 nm (total thickness of 2.9 μm) had the best tribological properties, corrosion resistance and superior hardness. Superlattice CrN/NbN coating deposited on CoCrMo alloy using HIPIMS discharge improves the surface hardness significantly (~34 GPa), higher wear resistance (4.94×10^{-16} $m^3N^{-1}m^{-1}$), lower coefficient of friction (μ=0.49) and fatigue (539 ± 59 MPa). Metal ion analysis shows that the CrN/NbN coating significantly minimizes the release of toxic ions (Co, Cr and Mo) from the substrate which makes this coating favourable for biomedical applications [59]. Juliano and co-workers, 2015 presented that the hardness, (*H*) of about 36 GPa can be achieved by depositing superlattice TiN/CrN coatings (bilayer thickness, 6.3 nm) [60]. Also, research shows that by combining both TiN and CrN with specific bilayer thickness can enhance the fracture toughness (K_{IC}), tribological properties and corrosion resistance. J.W. Du and co-workers, 2020 [61], obtained highest hardness of ~30 GPa by depositing superlattice TiN/CrN coatings with bilayer thickness of 6.3 nm compared to that of monolithic TiN (*H= 26.4 GPa*) and CrN (*H=17.3 GPa*). TiN/CrN multilayer coatings

have better oxidation resistance (800 °C for 10 hours) compared to that of monolithic CrN and TiN.

To the best of our knowledge HIPIMS plasma nitriding has never been reported before. The present work explores in-depth effect of HIPIMS discharge on plasma nitriding of CoCrMo alloy.

References

[1] D. Pye, “Practical NITRIDING and Ferritic Nitrocarburizing,” *Pract. Nitriding Ferritic Nitrocarburizing*, no. 06950G, 2003, [Online]. Available: www.asminternational.org.

[2] E. J. Mittemeijer, “Fundamentals of Nitriding and Nitrocarburizing,” in *ASM Handbook: Steel Heat Treating Fundamentals and Processes*, vol. 4A, . Dossett and G.E. Totten, Ed. 2013, pp. 619–646.

[3] Daniel Loch, MERI and University, “Development of an inductively,” 2015, SHU thesis archive, ProQuest: 10697283.

[4] B. Chapman and J. L. Vossen, “*Glow Discharge Processes: Sputtering and Plasma Etching*,” *Phys. Today*, vol. 34, no. 7, pp. 62–62, 1981, doi: 10.1063/1.2914660.

[5] Z. Xu and F. F. Xiong, *Plasma Surface Metallurgy*. 2017, https://doi.org/10.1007/978-981-10-5724-3.

[6] Z. Xu and F. F. Xiong, “Plasma Nitriding,” in *Plasma Surface Metallurgy: With Double Glow Discharge Technology---Xu-Tec Process*, Singapore: Springer Singapore, 2017, pp. 13–21.

[7] J. R. Roth, *Industrial Plasma Engineering: Application To Nonthermal Plasma Processing*, 1st ed., vol. 2. Boca Raton: CRC Press, 2001.

[8] T. Bell, H. W. Bergmann, J. Lanagan, P. H. Morton, and A. M. Staines, “Surface engineering of titanium with nitrogen,” *Surf. Eng.*, vol. 2, no. 2, pp. 133–143, 1986, doi: 10.1179/sur.1986.2.2.133.

[9] Y. Katayama, S., Matsunawa, A., Morimoto, A., lshimoto, S. and Arata, “Surface hardening of titanium by laser nitriding,” in *Proceedings of the Fifth International Conference on Applied Laser Electro-optics (ICALEO), Laser Institute of America, Orlando, FL*, 1983, pp. 127–134, doi: https://doi.org/10.2351/1.5057471.

[10] P. Schaaf, F. Landry, M. Han, E. Carpene, and K. P. Lieb, “Laser nitriding of iron,

stainless steel, and plain carbon steel investigated by mössbauer spectroscopy," *Hyperfine Interact.*, vol. 139–140, no. 1–4, pp. 307–314, 2002, doi: 10.1023/A:1021283624384.

[11] A. Walker, J. Folkes, W. M. Steen, and D. R. F. West, "Laser surface alloying of tllaniun substrates with carbon and nitrogen," *Surf. Eng.*, vol. 1, no. 1, pp. 23–29, 1985, doi: 10.1179/sur.1985.1.1.23.

[12] R. S. Razavi, G. R. Gordani, and H. C. Man, "A review of the corrosion of laser nitrided Ti-6Al-4V," *Anti-Corrosion Methods and Materials*, vol. 58, no. 3. pp. 140–154, May 24, 2011, doi: 10.1108/00035591111130523.

[13] H. Dong, "S-phase surface engineering of Fe-Cr, Co-Cr and Ni-Cr alloys," *Int. Mater. Rev.*, vol. 55, no. 2, pp. 65–98, Mar. 2010, doi: 10.1179/095066009X12572530170589.

[14] C. Blawert *et al.*, "Characterisation of duplex layer structures produced by simultaneous implantation of nitrogen and carbon into austenitic stainless steel X5CrNi189," *Surf. Coatings Technol.*, vol. 128–129, no. 1, pp. 219–225, 2000, doi: 10.1016/S0257-8972(00)00651-4.

[15] D. Ikeda *et al.*, "Effect of nitrogen plasma-based ion implantation on joint prosthetic material," *Surf. Coatings Technol.*, vol. 156, no. 1–3, pp. 301–305, 2002, doi: 10.1016/S0257-8972(02)00094-4.

[16] B. R. Lanning and R. Wei, "High intensity plasma ion nitriding of orthopedic materials. Part II. Microstructural analysis," *Surf. Coatings Technol.*, vol. 186, no. 1-2 SPEC. ISS., pp. 314–319, 2004, doi: 10.1016/j.surfcoat.2004.02.047.

[17] O. Öztürk, U. Türkan, and A. E. Erogˇlu, "Metal ion release from nitrogen ion implanted CoCrMo orthopedic implant material," *Surf. Coatings Technol.*, vol. 200, no. 20–21, pp. 5687–5697, May 2006, doi: 10.1016/j.surfcoat.2005.08.113.

[18] J. E. Greene, "Review Article: Tracing the recorded history of thin-film sputter

deposition: From the 1800s to 2017," *J. Vac. Sci. Technol. A Vacuum, Surfaces, Film.*, vol. 35, no. 5, p. 05C204, 2017, doi: 10.1116/1.4998940.

[19] C. J. Cleveland, "Geissler, Johann Heinrich Wilhelm," in Encyclopedia of Earth, Environmental Information Coalition," *Natl. Counc. Sci. Environ. Washington, D. C.*, 2008.

[20] W. Grove, "No Title," *Philos. Trans. R. Soc. (Taylor Fr.)*, vol. 142, no. 87, 1852.

[21] J. Pl€ucker, "Ueber die Einwirkung von Magneten auf die elektrischen Entladungen in verd€unnten Gasen: On the effect of magnets on the elec- tric discharge in dilute gases," *Ann. Phys. Chem.*, vol. 88, no. 103, 1858.

[22] A. W. Hull, "'The magnetron,'" *J. Am. Inst. Electr. Eng.*, vol. 40, no. 715, 1921.

[23] A. W. Hull, "The Effect of a uniform magnetic field on the motion of electrons between coaxial cylinders," *Phys. Rev.*, vol. 18, no. 31, 1921.

[24] F. M. Penning, "Coating by cathode disintegration," U.S. patent 2,146,025.

[25] D. Depla, S. Mahieu, J. E. Greene, "Sputter deposition processes," Editor(s): Peter M. Martin, Handbook of Deposition Technologies for Films and Coatings, 2010, pp. 253-296. https://doi.org/10.1016/B978-0-8155-2031-3.00005-3

[26] F. M. P. and J. H. A. Moubis, "Cathode Sputtering in a Magnetic Field," *Proc. K. Ned. Akad. Wet*, vol. 43, no. 41, 1940.

[27] F. M. Penning, "Die Glimmentladung bei Niedrigem Druck Zwischen Koaxialen Zylindern in einem Axialen Magnetfeld (The glow discharge at low pressure between coaxial cylinders in an axial magnetic field)," *Physica*, vol. 873 (3) 1936.

[28] X. Chu, M. S. Wong, W. D. Sproul, S. L. Rohde, and S. A. Barnett, "Deposition and properties of polycrystalline TiN/NbN superlattice coatings," *J. Vac. Sci. Technol. A Vacuum, Surfaces, Film.*, vol. 10, no. 4, pp. 1604–1609, 1992, doi: 10.1116/1.578030.

[29] J. A. Thornton and A. Penfield, "Cylindrical magnetron sputtering," in Thin Film

Processes, edited by J. L. Vossen and W. Kern (Academic, New York, 1978)

[30] G. N. Rokhlin, J. Phys. USSR 1, 347 (1939).

[31] E. Kay, "Magnetic field effects on an abnormal truncated glow discharge and their relation to sputtered thin-film growth," J. Appl. Phys. 34, 760 (1963).

[32] J. S. Chapin, "Sputtering process and apparatus," U.S. patent 4,166,018 (28 August 1979).

[33] "R. K. Waits, 'Planar magnetron sputtering,' in Thin Film Processes, edited by J. L. Vossen and W. Kern (Academic, New York, 1978)."

[34] "W. de Bosscher and H. Lievens, 'Advances in magnetron sputter sources,' Thin Solid Films 351, 15 (1999)."

[35] "I. Petrov, F. Adibi, J. E. Greene, W. D. Sproul, and W.-D. Munz, 'Use of an externally applied axial magnetic field to control ion/neutral flux ratios incident at the substrate during magnetron sputter deposition,' J. Vac. Sci. Technol., A 10, 3283 (1992)."

[36] A. A. Sugumaran, "Development of nanostructured PVD Coatings for Total Knee Replacement Joints using HIPIMS," Sheffield Hallam University, 2014.

[37] Biswas and Barnali, "Growth defects in CrN/NbN coatings deposited by HIPIMS/UBM techniques," 2017, [Online]. Available: http://shura.shu.ac.uk/18154/.

[38] P. E. Hovsepian, A. A. Sugumaran, Y. Purandare, D. A. L. Loch, and A. P. Ehiasarian, "Effect of the degree of high power impulse magnetron sputtering utilisation on the structure and properties of TiN films," *Thin Solid Films*, vol. 562, pp. 132–139, 2014, doi: 10.1016/j.tsf.2014.04.002.

[39] A. P. Ehiasarian, "HIPIMS With Low Magnetic Field Strength," GB 2437730 A, 2007.

[40] P. Hovsepian, G. Thompson. B. Lewis, A. Ehiasarian, and W.-D. Munz, Performance of High-Precision Knife Blades Treated by Plasma Nitriding and PVD Coating, SVC 46, At: San Francisco, CA, USA, May 2003.

[41] Dion I, Baquey C, Candelon B, Monties JR. Hemocompatibility of titanium nitride. Int J Artif Organs. 1992 Oct;15(10):617-21. PMID: 1428211.

[42] S. F. Cogan, "'Neural stimulation and recording electrodes,'" *Annu. Rev. Biomed. Eng.*, vol. 10, pp. 275–309, 2008.

[43] R. P. Van Hove, I. N. Sierevelt, B. J. Van Royen, and P. A. Nolte, "Titanium-Nitride Coating of Orthopaedic Implants: A Review of the Literature," *Biomed Res. Int.*, vol. 2015, 2015, doi: 10.1155/2015/485975.

[44] R. Machunze and G. C. A. M. Janssen, "Stress and strain in titanium nitride thin films," *Thin Solid Films*, vol. 517, no. 20, pp. 5888–5893, 2009, doi: 10.1016/j.tsf.2009.04.020.

[45] R. Machunze, A. P. Ehiasarian, F. D. Tichelaar, and G. C. A. M. Janssen, "Stress and texture in HIPIMS TiN thin films," *Thin Solid Films*, vol. 518, no. 5, pp. 1561–1565, 2009, doi: 10.1016/j.tsf.2009.09.069.

[46] J. Böhlmark, C. I. Ab, C. Physics, I. F. M. M. Physics, A. B. S. Tooling, and T. Selinder, "Reactive Film Growth of TiN by Using High Power Impulse Magnetron Sputtering (HIPIMS)," 2006.

[47] A. P. Ehiasarian, "Development of PVD Coating Processes Informed By Plasma Diagnostics- PHD Thesis," Sheffield Hallam University.

[48] D. Zhang *et al.*, "Comparative study on protective properties of CrN coatings on the ABS substrate by DCMS and HiPIMS techniques," *Surf. Coatings Technol.*, vol. 394, no. April, p. 125890, 2020, doi: 10.1016/j.surfcoat.2020.125890.

[49] R. Chetcuti, P. A. Dearnley, A. Mazzonello, J. Buhagiar, and B. Mallia, "Tribocorrosion response of duplex layered CoCrMoC/CrN and CrN/CoCrMoC coatings on implant grade 316LVM stainless steel," *Surf. Coatings Technol.*, vol. 384, no. September 2019, p. 125313, 2020, doi: 10.1016/j.surfcoat.2019.125313.

[50] U. Helmersson, S. Todorova, S. A. Barnett, J. E. Sundgren, L. C. Markert, and J. E.

Greene, “Growth of single-crystal TiN/VN strained-layer superlattices with extremely high mechanical hardness,” *J. Appl. Phys.*, vol. 62, no. 2, pp. 481–484, 1987, doi: 10.1063/1.339770.

[51] X. Chu, S. A. Barnett, M. S. Wong, and W. D. Sproul, “Reactive unbalanced magnetron sputter deposition of polycrystalline TiN/NbN superlattice coatings,” *Surf. Coatings Technol.*, vol. 57, no. 1, pp. 13–18, 1993, doi: 10.1016/0257-8972(93)90331-H.

[52] T. Hurkmans, T. Trinh, D. B. Lewis, J. S. Brooks, and W. D. Münz, “Multilayered titanium tungsten nitride coatings with a superlattice structure grown by unbalanced magnetron sputtering,” *Surf. Coatings Technol.*, vol. 76–77, pp. 159–166, 1995, doi: 10.1016/0257-8972(95)02596-0.

[53] M. Setoyama, A. Nakayama, M. Tanaka, N. Kitagawa, and T. Nomura, “Formation of cubic-AlN in TiN/AlN superlattice,” *Surf. Coatings Technol.*, vol. 86–87, no. PART 1, pp. 225–230, 1996, doi: 10.1016/S0257-8972(96)03033-2.

[54] M. Nordin, M. Larsson, and S. Hogmark, “Mechanical and tribological properties of multilayered PVD TiN/CrN, TiN/MoN, TiN/NbN and TiN/TaN coatings on cemented carbide,” *Surf. Coatings Technol.*, vol. 106, no. 2–3, pp. 234–241, 1998, doi: 10.1016/S0257-8972(98)00544-1.

[55] P. E. Hovsepian, D. B. Lewis, and W. D. Münz, “Recent progress in large scale manufacturing of multilayer/superlattice hard coatings,” *Surf. Coatings Technol.*, vol. 133–134, no. November, pp. 166–175, 2000, doi: 10.1016/S0257-8972(00)00959-2.

[56] D. C. Cameron, R. Aimo, Z. H. Wang, and K. A. Pischow, “Structural variations in CrN/NbN superlattices,” *Surf. Coatings Technol.*, vol. 142, no. 144, pp. 567–572, 2001, doi: 10.1016/S0257-8972(01)01057-X.

[57] E. Bemporad, C. Pecchio, S. De Rossi, and F. Carassiti, “Characterisation and wear properties of industrially produced nanoscaled CrN/NbN multilayer coating,” *Surf.*

Coatings Technol., vol. 188–189, no. 1-3 SPEC.ISS., pp. 319–330, 2004, doi: 10.1016/j.surfcoat.2004.08.069.

[58] Y. P. Purandare, A. P. Ehiasarian, and P. E. Hovsepian, "Deposition of nanoscale multilayer CrN/NbN physical vapor deposition coatings by high power impulse magnetron sputtering," *J. Vac. Sci. Technol. A Vacuum, Surfaces, Film.*, vol. 26, no. 2, pp. 288–296, 2008, doi: 10.1116/1.2839855.

[59] P. Eh. Hovsepian, A. P. Ehiasarian, Y. Purandare, A. Sugumaran, T. Marriott, I. Khan. Development of superlattice CrN/NbN coatings for joint replacements deposited by high power impulse magnetron sputtering. J. Materials Science: Materials in Medicine, (2016) 27:147. DOI 10.1007/s10856-016-5751.

[60] J. A. Araujo, G. M. Araujo, R. M. Souza, and A. P. Tschiptschin, "Effect of periodicity on hardness and scratch resistance of CrN/NbN nanoscale multilayer coating deposited by cathodic arc technique," *Wear*, vol. 330–331, pp. 469–477, 2015, doi: 10.1016/j.wear.2015.01.051.

[61] J. W. Du, L. Chen, J. Chen, and Y. Du, "Mechanical properties, thermal stability and oxidation resistance of TiN/CrN multilayer coatings," *Vacuum*, vol. 179, no. April, p. 109468, 2020, doi: 10.1016/j.vacuum.2020.109468.

Chapter 3
Experimental Methodology

3.1. Material, Substrate Preparation and HIPIMS Nitriding

3.1.1. Material:

CoCrMo alloy has been chosen for the entire study due to its high applicability in total hip replacement and total knee replacement. The composition of CoCrMo (standard- ASTM F75-12) is given in table 3-1.

Table 3-1
Chemical composition of CoCrMo alloy (F75).

Element	Cr	Mo	Ni	C	Si	Mn	S	N	Co
wt.%	27 – 30	5 – 7	≤ 0.5	≤ 0.35	≤ 1.0	≤ 1.0	≤ 0.10	≤ 0.25	Balance

3.1.2. Substrate Preparation:

Description of sample dimensions and the tests for which they were used is given in the table 3-2.

Table 3-2
Substrate material used for various tests and analytical methods.

CoCrMo alloy	Ø 20 mm×5.5 mm	FIB-SEM, SIMS, XRD, Nano and micro hardness, Tribological Test, Impact fatigue analysis, Fracture toughness analysis and electrochemical analysis

Before HIPIMS nitriding discs made from CoCrMo alloy were polished using different grades of abrasive sheet (mechanical grinding: 180, 320, 600, 1200, 2400, 4000 grit). The grinding

was carried out in conditions of running water and was followed by polishing using 6 and 1 µm diamond paste applied on velvet cloth. Before loading into the chamber, samples were cleaned in the automated industrial-sized cleaning line containing baths with various industrial detergents along with ultrasonic agitation to remove contaminants from the surface. Following the cleaning procedure, the samples were rinsed by deionised water and vacuum dried (85° C) for 30 minutes. Finally, the samples were immediately loaded into the chamber in order to avoid any contamination or residual dust. Contaminants on the surface might lead to forming surface defects during the process. Detailed information about cleaning line and solutions used at each stage is presented in the table 3-3.

Table 3-3

Sample's cleaning procedure.

Step ID	Solution	Temperature (^{0}C)	Time (min)
1	DI water+ Deconex HT 015+ Deconex HT 1169	58	7
3	DI water+ Deconex VP 1233A	55	7
2, 4	Tap water rinsing,	Room	1
6, 7	DI water rinsing and vacuum drying	50 and 85	Max. 30 min.

3.1.3. **Process Chamber Details (Hauzer HTC 1000-4/ABS coating machine):**

An industrial size *Physical Vapor Deposition* (PVD) system equipped with four magnetrons (Hauzer Techno Coating, The Netherlands) at the National HIPIMS Technology Centre at Sheffield Hallam University were used for both HIPIMS plasma nitriding and the deposition of nanostructured coating. The system is equipped with two mechanical vacuum

pumps (500m^3/h Root's pump and a 250 m^3/h rotary vane pump) and two turbomolecular pumps with a pumping speed of 2500 m^3/h (Blazers TPH 2200) which can achieve high vacuum in the range of about 10^{-6} mbar. The system is also equipped with high precision gas flow controllers operating in the range of 0-500 sccm to control the gas flow of nitrogen-hydrogen mixture (N_2:H_2) and argon (Ar). Plasma emission monitoring (Gencoa SpeedFlo) was used to control the reactive gas flow during the process.

The PVD system shown in figure 3.1 can be operated in either HIPIMS mode or Unbalanced Magnetron Sputtering (UBM) mode by simply switching the power supplies. The dimension of all four cathodes is around 1200 cm^2. The overall system is equipped with four DC and two HIPIMS power supplies (Hüttinger Elektronik Sp. z o.o., Warsaw, Poland) a dedicated bias power supply with active arc suppression units on the cathode and the substrate bias supplies (Hüttinger Elektronik Sp. z o.o., Warsaw, Poland). The HIPIMS power supply was capable of providing peak current of up to 1 kA and at a voltage of 2 kV. However, all these four cathodes are also equipped with a movable magnetic array mounted externally behind the targets in order to change the magnetic field from 400 Gauss to 100 Gauss.

Moreover, an insulated copper coil is placed around each cathode by which the magnetic field strength on cathode surface is varied to control the unbalancing effect on the magnetron. A rotating sample holder carousel is installed in the centre of the chamber which allows operation with three-fold orbital rotational motion [1][2]. To obtain the desired chamber temperature there are two radiation heaters mounted on both doors of the chamber. The temperature was precisely monitored with specially designed electrically isolated thermocouples mounted in the vacuum chamber and allowing direct temperature measurement at high bias voltages. The ion etching (surface cleaning) is obtained by merely injecting argon gas (Ar) during the process. Similarly, nitriding and coatings obtained by adding H_2/N_2 (15:85) and Ar/N_2 gas through gas inlets.

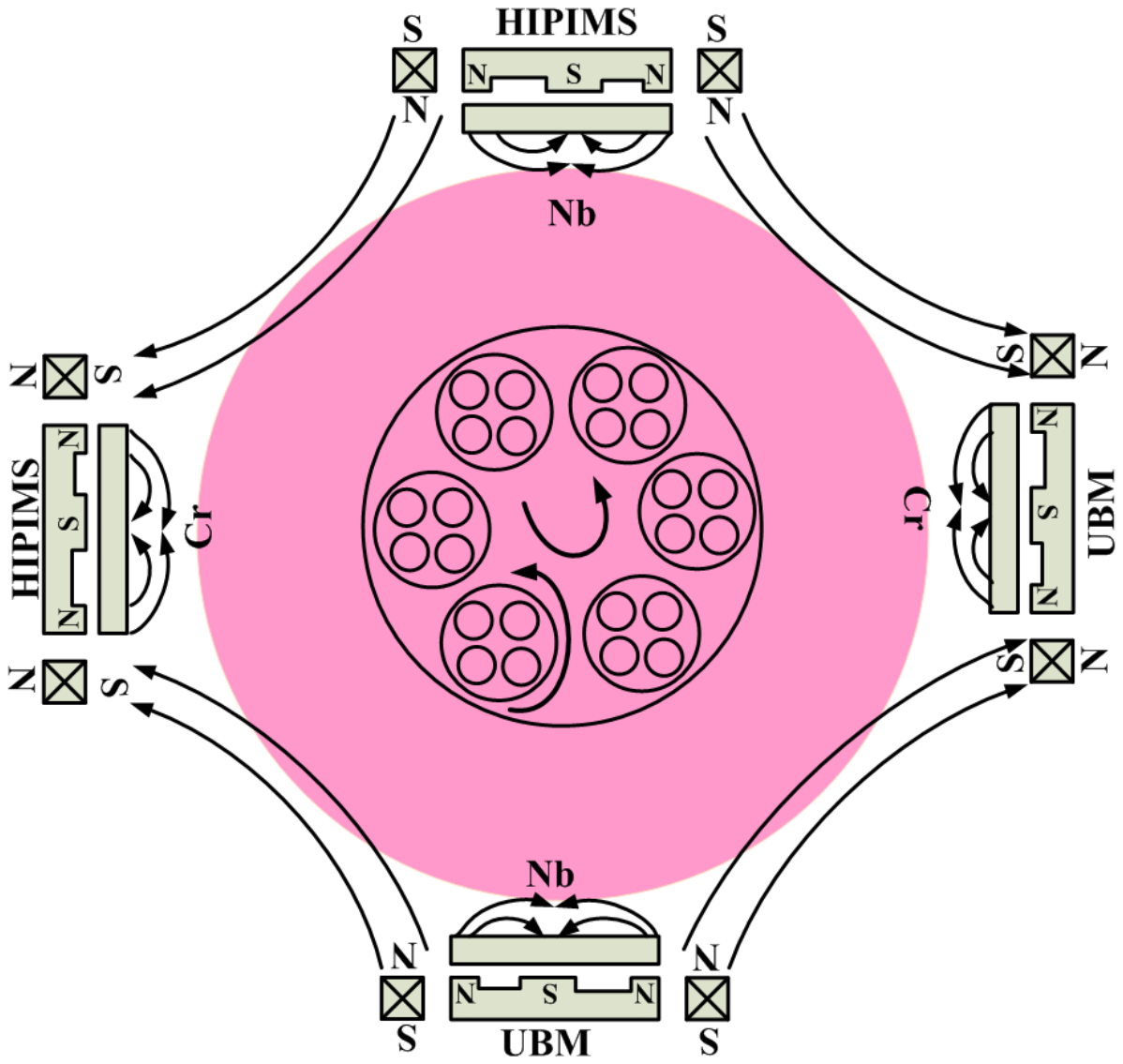

Figure 3-1: Schematic diagram of industrial sized PVD system.

3.1.4. **HIPIMS Nitriding Process Parameters:**

During nitriding the process power on the cathode were maintained between 1-2 kW to avoid high sputtering of the metal targets (Cr and Nb). Only parameters were varied here was nitriding voltage to understand the effect of high energy bombardment on nitriding or diffusion depth.

Table 3-4

Nitriding process parameters.

Base Pressure	5.8×10^{-6} mbar
Operating Pressure	8.3×10^{-3} mbar
Reactive Gas	N_2:H_2 (85:15)
Process Temperature	400° C
Substrate holder	3-fold rotated
Power on each Metal Target (Cr/Nb)	1-2 kW
Nitriding Voltage	-500 V to -1100 V

3.2. Characterisation methods

3.2.1. X-ray Diffraction (XRD) Analysis

In this study, a PANalytical Empyrean automated X-ray Powder diffractometer (Co and Cu x-ray tube), with a PIXCEL-3D area detector, was used in θ-2θ Bragg–Brentano (*BB*) and Glancing Angle (*GA*) beam geometry to determine the phase combination in the specimen. In this work, *BB* geometry was not selected for the study due to its high penetration depth at a higher incident angle. The scanning range for *GA-XRD* was selected as 2θ = 20° to 120° with a step size of 0.006°. The *GA-XRD* technique is a convenient method for stress analysis and phase identification studies in the case of the nanostructured coatings. Due to the reduced penetration depth of the X-rays in *GA* geometry, the contribution related to the substrate is eliminated in comparison to standard X-ray diffraction. In this geometry, the incidence angle (α) is fixed at 0.5°, 1° and 2°. The detector position was varied from 20º to 120º while keeping incident beam fixed. PANalytical *HighScore Plus* Software, together with the ICDD Powder

Diffraction File database, was used to analyse the phases present in the *GA-XRD* diffraction patterns.

The lattice parameters (a), interplanar distance (d) and lattice expansion $\left(\frac{\Delta a}{a_0}\right)$ were calculated using Bragg's equation [4] [5].

$n\lambda=2d\sin\theta$ **Equation 3-1**

where n=1 and θ value were obtained using data analysis software (Origin 9.0). So,

$$d = \frac{\lambda}{2\sin\theta}$$ **Equation 3-2**

Where d value can be calculated for each reflection using their known crystal structure.

For cubic structure,

$$\mathrm{d(hkl)} = \frac{\mathrm{a(hkl)}}{\sqrt{(h^2 + k^2 + l^2)}}$$ **Equation 3-3**

$$\mathrm{a(hkl)} = d^*_{hkl}\sqrt{(h^2 + k^2 + l^2)}$$ **Equation 3-4**

So, **Equation 3-5**

$$\text{lattice expansion } \left(\frac{\Delta a}{a_0}\right) = \frac{a_0}{(a - a_0)}$$

Further to explore the crystallographic orientation of the nitrided layer, texture coefficient (T*) was calculated for all samples using the method presented in [6].

$$T^* = \frac{\mathrm{I_{hkl}/R_{hkl}}}{(1/\mathrm{n})\sum_0^{\mathrm{n}}(\mathrm{I_{hkl}/R_{hkl}})}$$ **Equation 3-6**

Where $I_{(hkl)}$ is the measured peak intensity from the (hkl) reflections, $R_{(hkl)}$ is the reference standard (random) peak intensity from the (hkl) reflections and n is the number of reflections considered.

Note: The observed peaks in diffraction patterns indicate a family of planes which are produced at specific diffraction angle 2θ. In the X-ray diffraction patterns, γ is austenite phase, γ_N expanded austenite (also known as S phase), ε is a ferrite.

3.2.2. **Focused Ion Beam-Scanning Electron Microscopy (FIB-SEM):**

A Quanta 3D SEM equipped with a focused ion beam (FIB), secondary electron, and backscattered electron detector was used in this work. The electron beam having energy ranging from a few 200 eV to 50 keV, scanned across the sample surface. As the source electron beam interacts with the sample, the incident electrons interact with the atomic electrons and scattered across due to different collisions such as elastic and inelastic. Various types of emissions associated with electron beam-sample surface interaction are shown in figure 3.3. Using detectors such as secondary electron (SE) or backscattered electron (BSE), these deflected and emitted electrons from the samples surface can be collected and utilised to depict a sample's topographical, microstructural features and chemistry. Here, SEM was used to collect the SE images of a planar and fractural cross-sectional view of the nitrided samples. SE electrons were ejected as a result of an inelastic collision. By theory, once the incident electron with adequate energy interacts with an atom, an electron can be ejected from the same atom due to energy transfer from the source electron (incident). However, such ejected electrons have relatively minimal energy; as a result, only electrons of the atoms at the surface get away from the specimen and capture. Further, low and high magnification images were obtained

using Everhart-Thornley and Through-the Lens Detector. The working distance was fixed for 10 mm, and the beam voltage varied from 5 keV to 20 keV to obtain the high-resolution images.

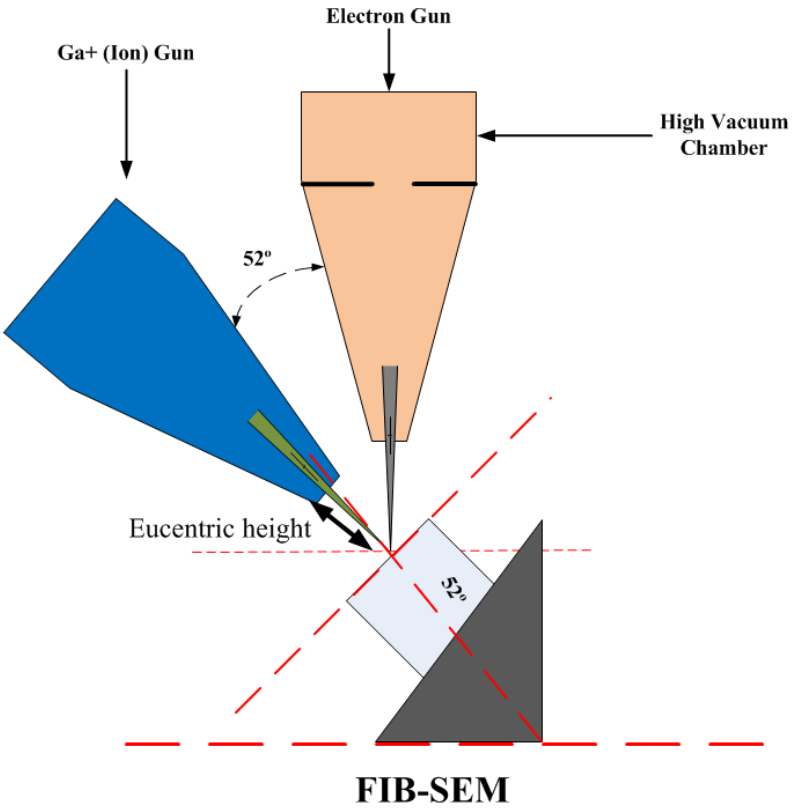

Figure 3-2: Schematic of FIB-SEM instrument.

Also, a Focused Ion Beam Cross-section (*FIB-CS*) technique (FEI Quanta 3D) was used to study the subsurface deformation mechanism of the specimens during various mechanical studies. The *FIB* gun was equipped with a Ga source which was further ionised by applying a high voltage of 2 kV to 30 kV. The mechanism of the FIB gun is like those electron guns where electrostatic lenses are used to accelerate the beam and to focus the beam on to the object. Interaction of the ion with the object surface emits the secondary e- similar to the electron beam to image the surface. Additionally, ion interaction generates defects in the sample and removes the material through sputtering. The beam current can be changed from 1 pA to 65 nA based on the type of milling. The sputtering rate of the material can be controlled by changing the ion current. In this work, mainly cleaning cross-section and rectangular cross-section mode were used.

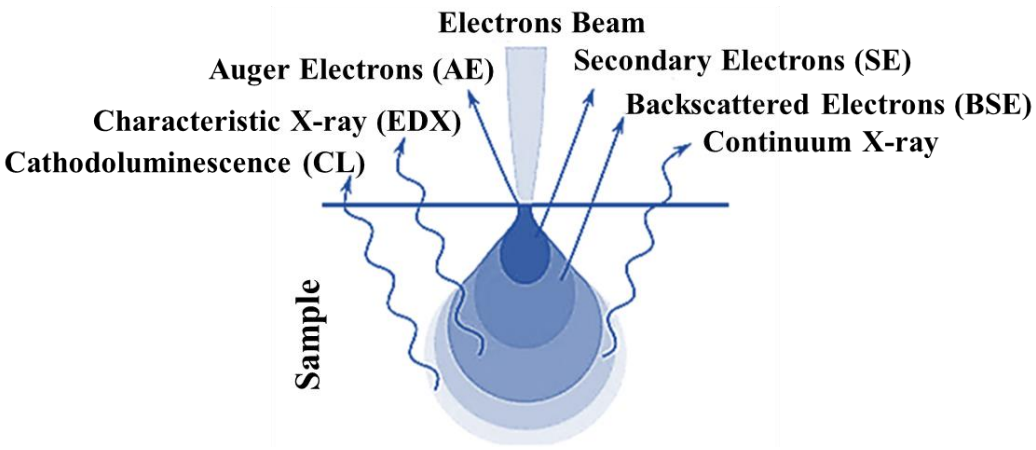

Figure 3-3: Schematic of electron-matter interactions (various types of signal generated) [8].

In this work, for milling of the deformed area, an ion beam accelerating voltage of 30 kV voltage was used. After milling, an ETD SE detector was used to image the cross-section of the deformed area. The working distance was fixed for 10 mm to maintain the Eucentric height, and the voltage was varied from 2 keV to 10 keV.

The chemical composition of the wear debris after impact and tribo tests were analysed using energy-dispersive X-ray spectroscopy. Characteristic x-rays are generated due to the transition of electrons from higher electrons shell to lower electron shell. High energy incident electrons can also eject inner shell electrons from the sample surface atoms. As a result, electrons from the outer shell shift to the inner shell, and in-process characteristic x-rays with specific wavelengths and energies are emitted [1][2][8].

3.2.3. **Secondary ion mass spectrometry (SIMS)**

Secondary ion mass spectrometry (SIMS) by a HIDEN Analytical SIMS Workstation utilizing a quadrupole mass spectrometer. This instrument was used to analyse the layer composition and diffusion depth of the nitrided layers. Oxygen (O) ions were used at a beam current of 420 nA to analyse the layer composition and diffusion depth. The sample was placed in an ultra-high vacuum chamber and bombarded with ions using specially designed ion gun. The area of analysis was 100 μm^2. The sputtered particles from the sample surface consisted of a mixture

of ions and neutrals. The ions were separated and at the same time neutrals were ionised by electron beam. At the end, ionised species accelerated through various filters and detectors to mass spectrometer to analyse targeted element based on its mass to charge ratio.

3.2.4. **Glow Discharge Optical Emission Spectroscopy (GDOES):**

Quantitative elemental depth analysis was performed using GDOES (Horiba Jobin Yvon). The obtained results were in the form of elements counts per second which was further processed into results of at. % per nanometer depth by comparing it with a standard sample with known stoichiometry such as CrN (50:50). However, to confirm the interface between nitrided layer and CoCrMo matrix (substrate), the sputtering of sample surface was carried out upto the thickness of 10 µm. Before the measurement of actual samples, background measurements were performed for Co, Cr, Mo, W, Fe, N and H to corelate with obtained result.

3.2.5. **Pin-on-disc**

The tribological study is a combination of various studies such as wear (volume loss), friction behaviour (friction coefficient) and chemical composition analyses of the wear products.

The wear resistance represented by the wear coefficient, K_c and the friction coefficient), μ are essential properties of any tools, prosthesis and other mechanical devices. Pin on disc (POD) technique is widely used to calculate K_c and μ of the materials or coatings in aggressive (saltwater, body fluid etc.) and non-aggressive (air) environments. It can also be found that friction force is directly related to normal load (N) (through Amonton's 2nd law) [9].

$$F = \mu N \qquad \textbf{Equation 3-7}$$

Where µ is called the coefficient of friction.

Wear is related to the loss of material due to the removal mechanism during continuous friction between the mating surfaces. It is believed that the wear does not occur through on its own wear mechanism. Wear of the material can be affected by various reasons such as

environment, temperature, load, surface roughness, speed of pin. Significant information can be obtained through wear debris size and shape, volume and surface roughness [10]. The various range of wear mechanisms can be seen according to the condition in which it tested. These mechanisms can be categorised into four different modes such as (a) adhesive wear (b) abrasive wear (c) fatigue wear and (d) corrosive wear [10].

In this work, the POD instrument was used (CSM, Anton Paar) to study the tribology behaviour of the samples in dry sliding condition. This instrument is equipped with different ball as a counterpart (pin). The counterpart is pressed against the rotating specimen surface clamped in the specimen holder with a static load of 5 N applied on the head of the pin. This Pin is attached on an elastic arm which moves laterally and measures the tangential force or frictional force between the pin and the specimen with a sensor [11]. As a result, the pin generates the circular scar with specific width which is well known as a wear track. Details of the test parameters are given in the table 3-5.

Table 3-5

Dry sliding wear tests parameters

	Dry Sliding
Ball (6 mm)	Al_2O_3
Temperature (°C)	26-28°
Humidity (%)	35-45
Sliding length (km)	0.2, 0.25, 0.5, 1.0 and 2.0
Load (N)	5

Wear coefficient was calculated using the standard method proposed by Archard's [12][13]

$$K_c = \frac{2 \times 3.14 \times R \times A}{F_N \times 2 \times 3.14 \times R \times Number\ of\ laps}$$ **Equation 3-8**

Where K_c is wear coefficient (m^3/N.m), V is a wear volume loss (m^3), F_N is normal load applied (N) and L is the sliding distance (m). Average wear volume was obtained using the surface profilometer (DEKTAK 150 Stylus) by scanning the wear track three times. The area was obtained from the software (Dektak).

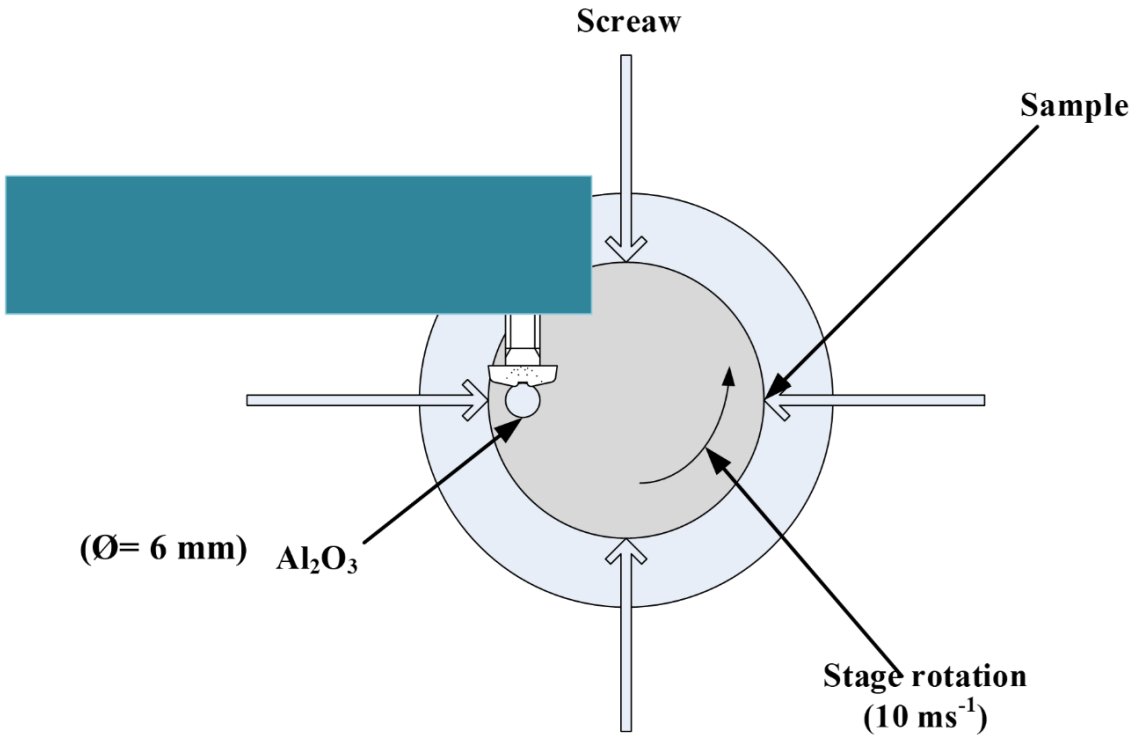

(a)

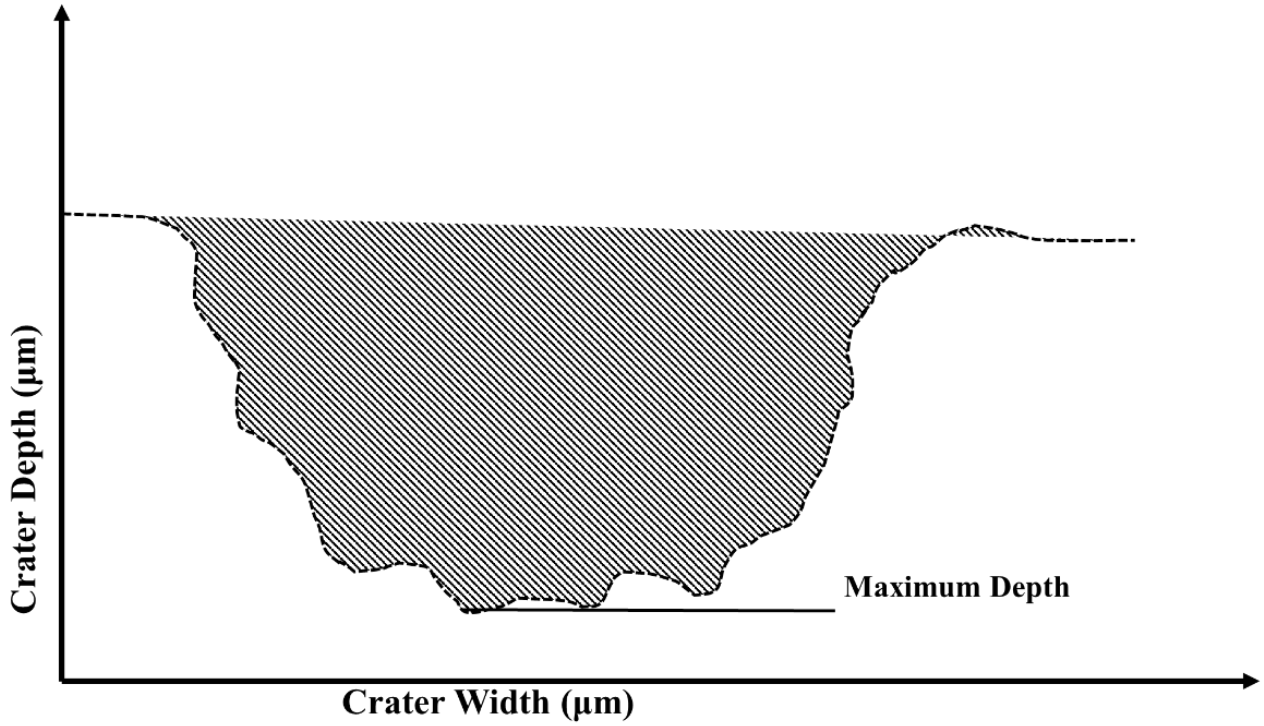

(b)

Figure 3-4: (a) Schematic diagram of pin-on-disc and wear track profile and (b) Wear track profile obtained using profilometer.

3.2.6. **Mechanical Tests**

Various microhardness measurement techniques including Vicker's and Knoop and nanohardness tests were used to evaluate the surface hardness of the materials, modified layers and matrices. A Vickers microhardness tester was utilised to calculate the fracture toughness of treated and untreated samples.

3.2.6.1. Nanohardness Analysis

A standard CSM Nanohardness tester equipped with a Berkovich indenter was used to measure the surface hardness (H) and Elastic modulus (E) of specimens. The indenter was moved towards the normal direction to the surface, by applying progressive load on the surface up to the set point. For this experiment, a fixed applied load of 5 mN was used for all specimens. After holding for few seconds, the indenter was completely or partially removed until the

complete relaxation of the surface occurs. Once the load is entirely removed from the surface, the surface attempts to recover its original shape but is prevented from doing so as plastic deformation occurs during loading-unloading cycle [14]. However, some recovery happens due to elastic strain relaxation in the material. Later the H and E value were calculated using the obtained L-U curve, also known as the force-displacement curve by using the software. At the same time the depth and the load are measured using the same L-U curve. The formula used by the software to calculate the H and E value after the test is presented below (equation 3-9).

$$H = \frac{L}{24.5h_c^2} \text{ and } E = \frac{1}{2}\frac{\sqrt{\pi}}{\sqrt{24.5h_c^2}}\frac{dL}{dh} \qquad \textbf{Equation 3-9}$$

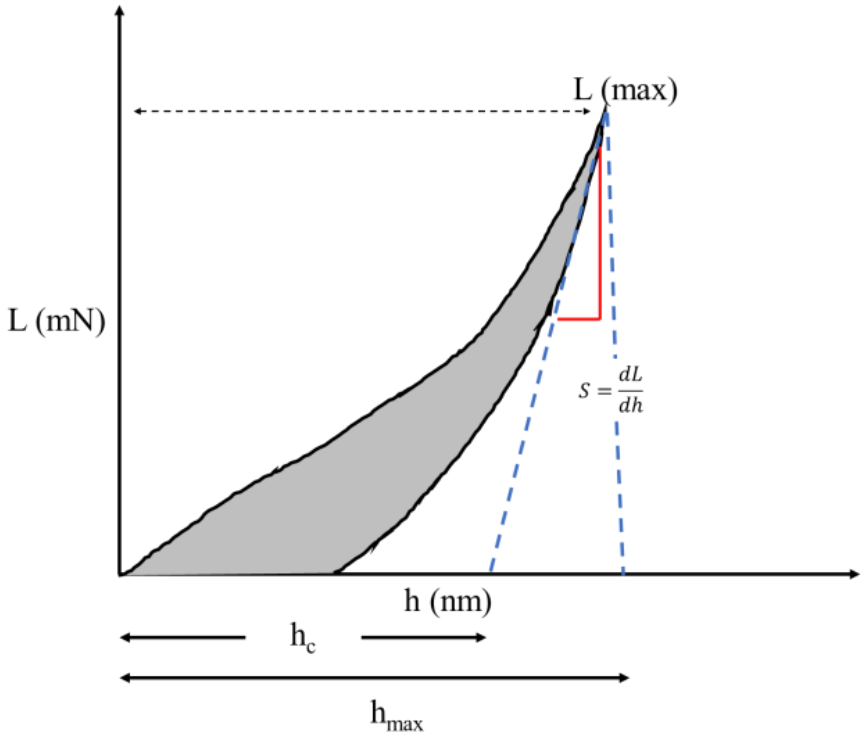

Figure 3-5: Loading-unloading curve.

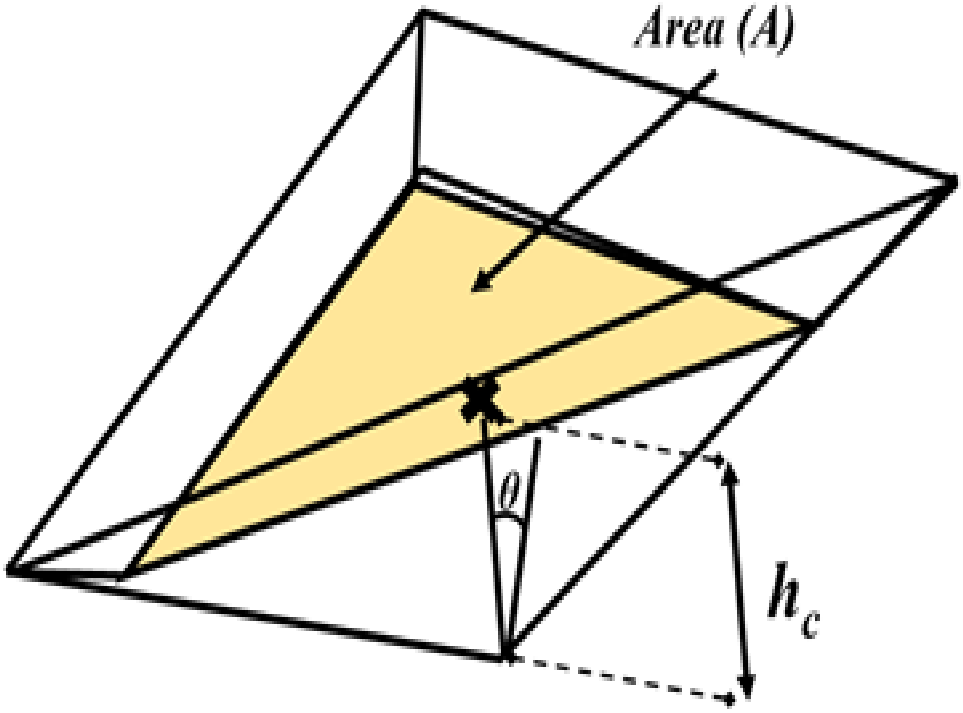

Figure 3-6: A schematic impression of indent impression on the surface.

where, P is applied load and $\frac{dP}{dh}$ is same as the slope of the unloading side of the curve shown in figure 3-5. Note: The area under the unloading curve defines the amount of plastic deformation occurs during unloading.

3.2.6.2. Knoop Hardness Test:

The Knoop microhardness (KMH) test is a standard test to measure the microhardness of the modified layers as well as bulk metals and alloys. The Knoop test is analogous to that of the Vickers microhardness test. The only difference between them is the shape and angle of the diamond pyramidal indenter [14]. The Knoop indenter has unequal edge length, which leaves the impression with one diagonal with seven times bigger than the shorter diagonal. Details of information about the impression are presented in the figure 3-7. Ideally, hardness value calculation is similar to Nanohardness. Longer diagonal length (d) is used to calculate the

projected area of the impression. To measure the precise area of the impression a digital microscope connected to a computer equipped with image analysis software was used.

$$\mathrm{KMH} = \frac{2L}{d^2\left[\cot\frac{172.5}{2}\tan\frac{130}{2}\right]}$$ **Equation 3-9**

Where 172.5° and 130° are the angles of the opposite faces of the Knoop indenter and L is the applied load.

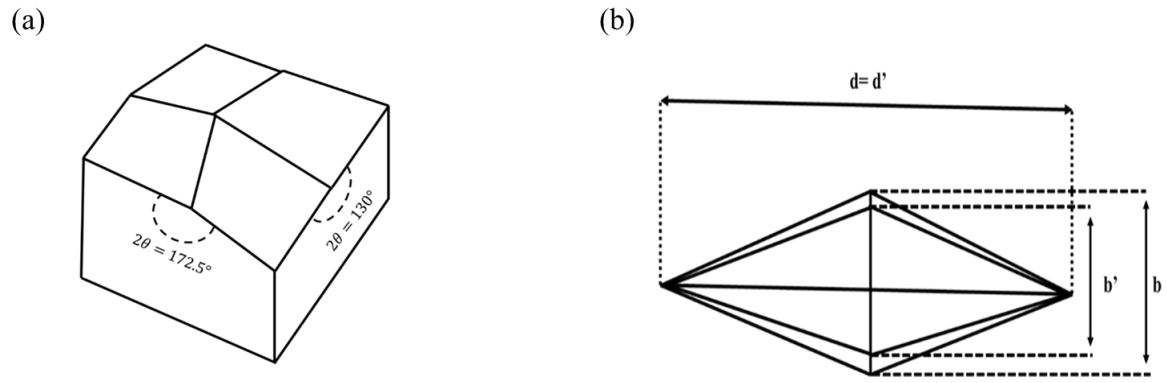

Figure 3-7: (a) Schematic of Knoop indenter and (b) The long and short diagonal of the indenter. The length of the long diagonal remains the same during both loading and unloading (d=d') whereas the short diagonal length after unloading decreased from b to b' [14].

3.2.6.3. Fracture Toughness Analysis:

In this work, the indentation method was used to calculate the fracture toughness (K_{Ic}) of the samples. Ideally, in this method, a sharp diamond-type indenter such as Vicker's was mainly used. Upon loading, at high applied load, tensile stresses are generated in the material as the radius of the plastic zone increases. Whereas, during unloading of the indenter, the build-up of extra stresses due to elastically strained area of the material (outside the plastic zone) attempts to regain its original shape. However, it is prevented from doing so due to permanent plastic deformation which is directly associated with the plastic region in the material [14]. Indentation technique has become one of the important methods to evaluate the fracture toughness of the coatings and alloyed surfaces [15][16]. Generally, three different kinds of cracks can be

observed, such as radial, lateral and median cracks. These cracks are illustrated in the below Table 3.6.

Table 3-6

Detailed explanation of type of cracks.

Crack Type	Type	Origin	Reason for Formation
Radial	Vertical half-penny	On the surface, outside the plastic zone	Hoop stress and spread downward into the sample.
Lateral	Horizontal	Beneath the surface and parallel to the load axis	Tensile stresses and extended to the surface. Emerges surface ring which can lead to the chipping of the surface.
Median	Vertical circular penny	Beneath the surface of the material and parallel to the symmetry axis. Also, have direction adjacent to the corners of the indentation.	Not clear. However, based on applied load, the two half-penny cracks can extend upward intersect the surface.

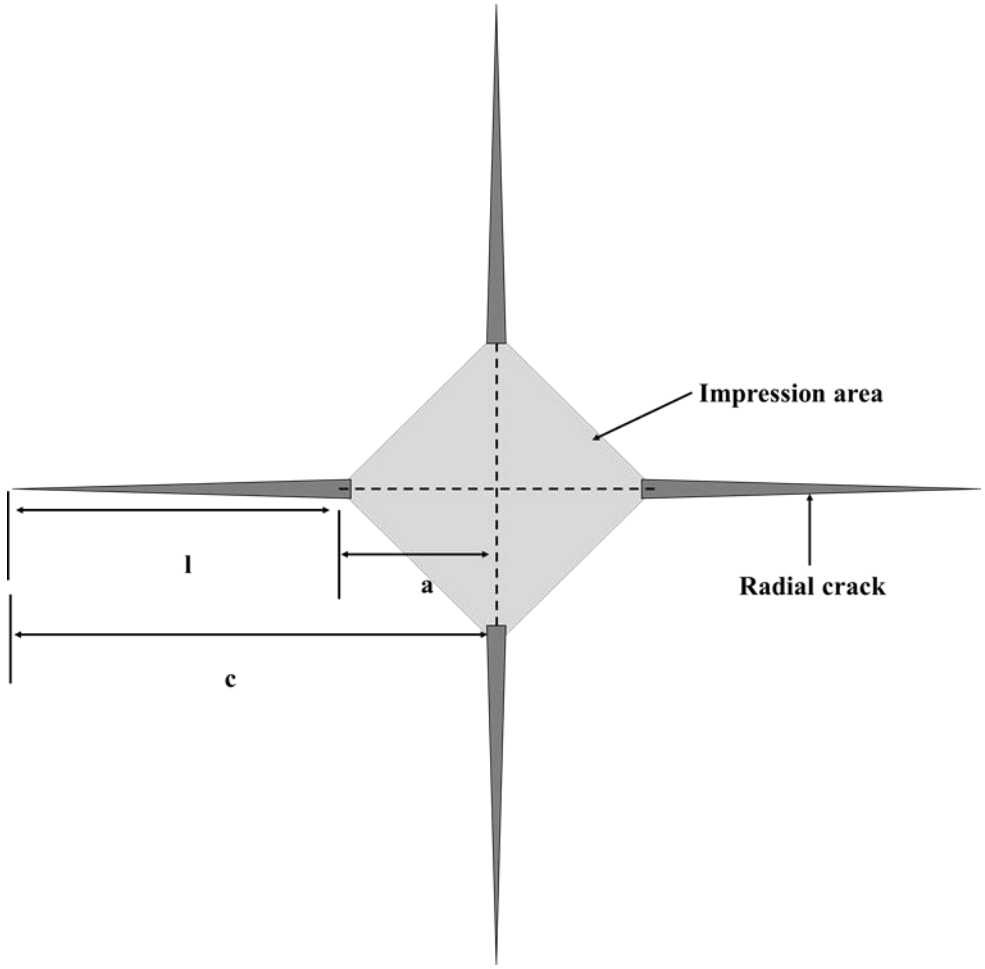

Figure 3-8: Schematic of radial cracking at Vickers indentation

To calculate K_{lc} value of the samples requires precise measurement of crack length (c) using an electron microscope (EM) formed on the surface after indentation along the edges of the indenter. The formula to calculate K_{lc} is described below [14] [17] [18]

$$K_{lc} = \delta \sqrt{\frac{E}{H}} \times \left(\frac{L}{c^{3/2}}\right) MPamm^{1/2}$$ **Equation 3-10**

Where δ (0.016) is the constant value obtained from literature, L is the applied load (N), E is the elastic modulus (Nmm^{-2}), and H is the Vickers hardness value of the material (Nmm^{-2}).

So,

$$c = (l + a)$$ **Equation 3-11**

$$c^{3}/_{2} = \left(\frac{\sum_{i=1}^{4} c_i}{4}\right)^{3}/_{2}$$ **Equation 3-12**

3.2.6.4. Impact Fatigue Analysis:

Materials such as CoCrMo alloys and biocompatible steels used in the making of prosthetics where cyclic loading is very common. Under such loading conditions, fatigue cracks are very common and can lead to severe consequences. To understand the cracking mechanism under such loading condition of such materials around 10 million (10^7) cyclic point loadings are applied. Later, the tested area was analysed under a microscope. By utilizing microscopy, the cracking mechanism can be explored. Further study can be done using Raman spectroscopy to understand the oxidation behaviour of the surface after impact testing. Ideally, the fatigue limit of the material can be obtained by plotting the number of impacts vs. applied load or stress (S-N curve). After the start of the test, S decreases gradually and at some point it stabilizes, which means the material reached its fatigue limit. In this work, a macro impact tester (CemeCon) was utilised to make various impacts on the untreated and nitrided specimens. Below table 3-7 contains the parameter used for the tests.

Table 3-7

Impact fatigue test parameters.

Parameters	
Ball diameter	9 mm
Load	500 N
Number of Impact	Initial= 250 Final= 1 million
Frequency	50 impacts/sec.
Applied current	10 A

3.2.7. **Potentiodynamic Polarisation (Corrosion) Study**

Corrosion is an event under which degradation of material into the original state as found in nature due to chemical reaction of metals/alloys in an aggressive environment such as acids, bases etc. It is also known as the reverse metallurgy engineering, because it allows the metals to reform the structure into their most thermodynamically stable state as sulphides, oxides or other compounds. Hence, metallurgy allows forming metal by supplying energy [1][2].

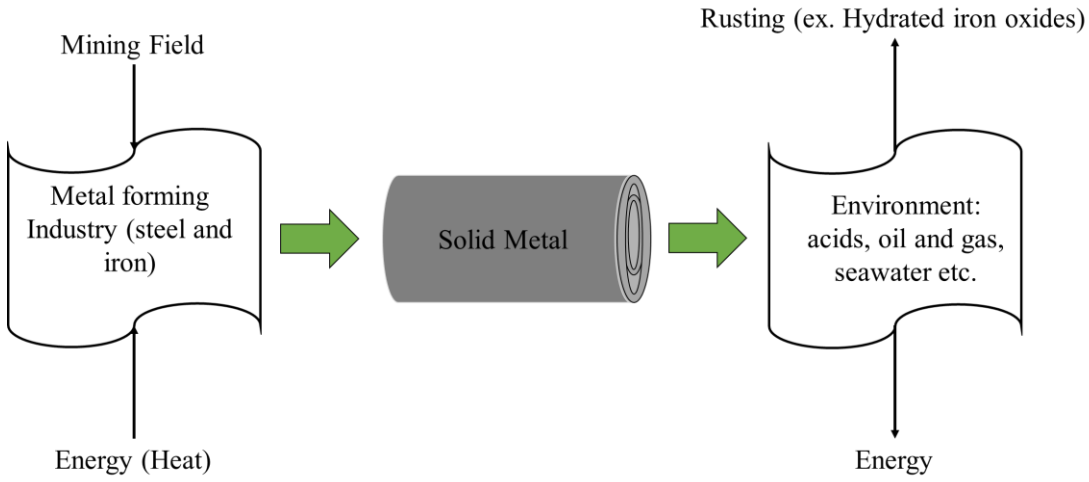

There are various types of corrosion reaction occurring on an environmentally exposed surface [19]:

a) On the entire surface (generalised corrosion).

b) On a specific area of the surface (localised corrosion).

c) Stress corrosion cracking occurs under tensile loading; the attack on the surface can cause crack formation perpendicular to the tensile stress.

d) Selective corrosion mostly takes place in alloys, where the corrosion process puts all the constituent of the alloy into the test solution (environment). In some cases, only one component of the material is dissolved, or only the grain boundaries of the material attacked producing the intergranular corrosion (in case of coatings).

So, corrosion is a coupled electrochemical reaction where both cathodic and anodic reactions co-occur at different sites of the materials. Under anodic reaction, production of an e^- occurs as a result of an oxidation reaction.

$$Me(s) \rightarrow Me^{+}_{(aq)} + e^{-} \qquad \textbf{Equation 3-13}$$

Where notation (s) is solid, and (aq) is aqueous.

Whereas, under cathodic reaction, reduction of given species happens, which means a decrease in oxidation number.

$$2H^{+}_{(aq)} + 2e^{-} \rightarrow H_{2(aq)} \qquad \textbf{Equation 3-14}$$

Such a reaction predominantly can be seen in the acidic environment. So, total corrosion reaction can be visualised as,

$$Fe + 2H^{+} \rightarrow Fe^{+2} + H_2 \qquad \textbf{Equation 3-15}$$

Note: Two half-cell reactions can occur on the same material as the polycrystalline metals contain various grain and crystal faces (grain boundaries). Also, these metals have multiple defects such as steps, edges, screw dislocation, point defects and kink sites.

In this work, a Gill potentiostat was utilised to examine the corrosion behaviour of nitrided and duplex coated specimens. An Ag/AgCl was used as a reference electrode. Specimens were used as working electrode and two graphite rods as an auxiliary electrode. The working electrode was polarised from -1000 mV to +1000 mV at a scan rate of 0.5 $mVsec^{-1}$ to observe both cathodic and anodic behaviour. The potential was changed with respect to time, and simultaneously current was measured between auxiliary and working electrode. The detailed test setup is presented schematically in figure 3.9.

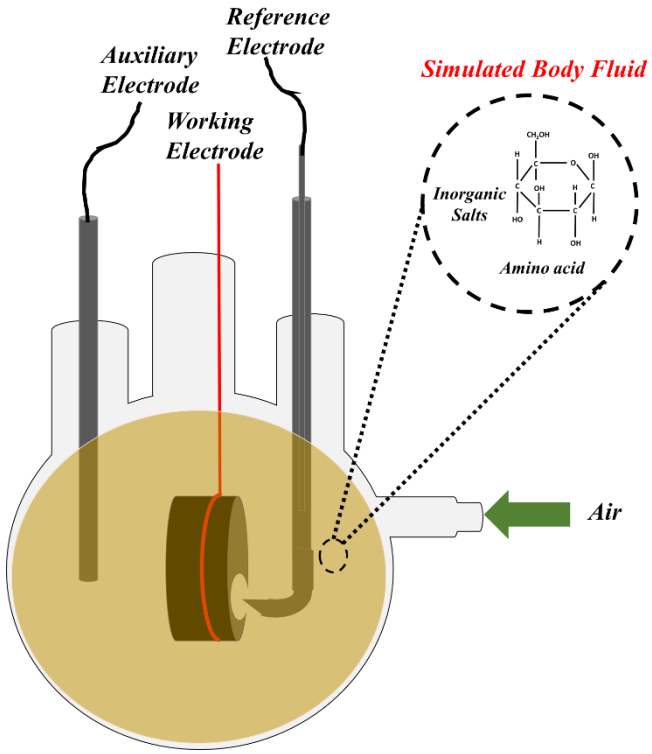

Figure 3-9: A schematic cross-section view of three electrode cell corrosion test setup**.**

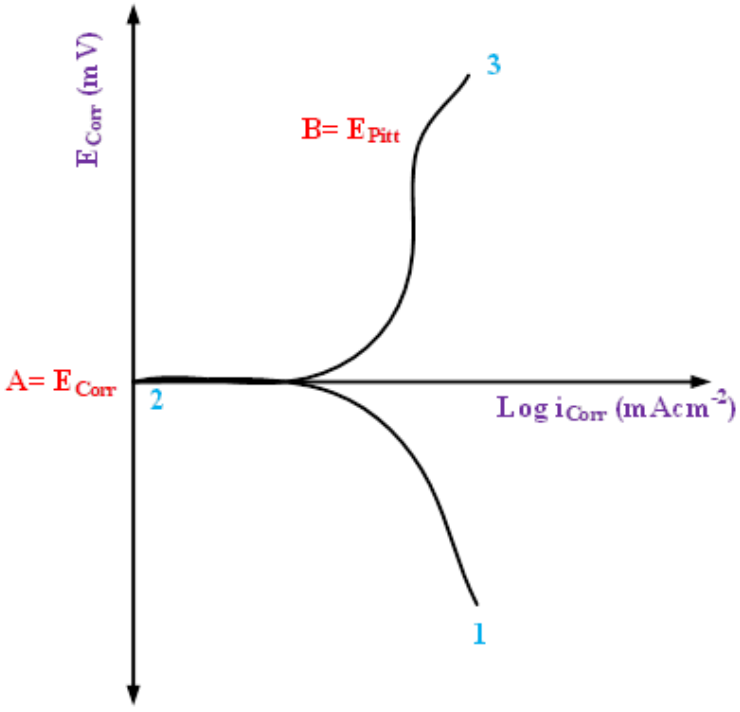

Figure 3-10: An example of E vs log i_{Corr} plot for stainless steel in Hank's solution (pH 7.3).

Figure 3.10 depicts the corrosion potential (E_{Corr}, mV) vs Corrosion current density (Log i_{Corr}, $mAcm^{-2}$) obtained from the test also called a potentiodynamic polarisation curve (PPC). PPC is a standard method to analyse the corrosion behaviour of any material. It is a very common practice to treat current densities value to be considered as positive [20]. The region from 1-2 is the cathodic region (first half cell) and from 2-3 is the anodic region of the other half of the cell. In the plot, an area up to B is considered as a passive region which defines the capability of material to form a passive layer (thin oxide layer of about 1-4 nm). Point B in the plot indicates E_{Corr} which can be found at the intersection of the cathodic (oxygen consumption) and anodic (metal dissolution) line of the curve [20].

Many metals tend to form metal oxides by reacting with the solution. These passive oxide layers provide self-protection from localised corrosion in a corrosive environment (aqueous). Also, in this region the i_{Corr} value measured constant and very low. Once the layer breakdown occurs, the corrosion potential and current increases suddenly and reaches to its high value. The reason is called pitting potential in that at this point, the surface forms pits and as the voltage increases the pitting also increases. In some metal, also transpassive region can be observed after breakdown of the first passive layer.

3.2.8. **Raman Spectroscopy**

The Raman analysis were performed using a Horiba-Jobin-Yvon HR800 integrated Raman spectrometer fitted with a green laser (λ = 532 nm) to obtain the oxides and metal oxynitride composition formed after dry sliding wear tests and corroded surface. The laser was focused on the targeted area of the sample surface in a 1 µm diameter spot through a standard 100x microscope objective. The spectra were recorded from 200 to 1500 cm-1 and fitted by gaussian and Lorentzian peaks. To acquire a targeted Raman spectrum various transmission filter were used (from 20 % to 100 % of the total laser power).

References

[1] Biswas Barnali, “Growth defects in CrN/NbN coatings deposited by HIPIMS/UBM techniques,” 2017, [Online]. Available: http://shura.shu.ac.uk/18154/.

[2] A. A. Sugumaran, “Development of nanostructured PVD Coatings for Total Knee Replacement Joints using HIPIMS,” Sheffield Hallam University, 2014, ProQuest Number: 10694168.

[3] F. E. Zink, “X-ray tubes.,” *RadioGraphics*, vol. 17, no. 5, pp. 1259–1268, 1997, doi: 10.1148/radiographics.17.5.9308113.

[4] M. F. C Ladd and R. A. Palmer, *Structure Determination by X-ray Crystallography*, Second edition. 1979. https://doi.org/10.1007/978-1-4614-3954-7.

[5] S. OKUR, “Structural, compositional and mechanical characterization of plasma nitrided CoCrMo alloy.”, December, 2009. http://openaccess.iyte.edu.tr/xmlui/bitstream/11147/3036/1/T000079.pdf

[6] K. Shukla, A. A. Sugumaran, I. Khan, A. P. Ehiasarian, and P. E. Hovsepian, “Low pressure plasma nitrided CoCrMo alloy utilising HIPIMS discharge for biomedical applications,” *J. Mech. Behav. Biomed. Mater.*, vol. 111, p. 104004, Nov. 2020, doi: 10.1016/j.jmbbm.2020.104004.

[7] S. K. Kulkarni, *Nanotechnology: Principles and Practices*. 2015.

[8] A. Nanakoudis, “SEM: Types of Electrons and the Information They Provide,” *Thermo Fisher Scientific*. https://www.thermofisher.com/blog/microscopy/sem-types-electrons-and-the-information-they-provide/.

[9] D. Arnell, “2 - Mechanisms and laws of friction and wear,” in *Tribology and Dynamics of Engine and Powertrain*, H. Rahnejat, Ed. Woodhead Publishing, 2010, pp. 41–72.

[10] K. Kato and K. Adachi, “Wear Mechanisms,” *Mod. Tribol. Handbook. Vol 1*, p. 28,

2001, doi: 10.1201/9780849377877.ch7.

[11] R. P. Nair, D. Griffin, and N. X. Randall, “The use of the pin-on-disk tribology test method to study three unique industrial applications,” *Wear*, vol. 267, no. 5–8, pp. 823–827, 2009, doi: 10.1016/j.wear.2009.02.026.

[12] B. Bhushan, Bharat Bhushan, and B. K. Gupta, *Handbook of tribology : materials, coatings and surface treatments*. McGraw-Hill.

[13] I. Hutchings and P. Shipway, *Tribology: Friction and wear of engineering materials: Second Edition*, 2017. https://www.elsevier.com/books/tribology/hutchings/978-0-08-100910-9.

[14] A. C. Fischer-Cripps, *Nanoindentation*, Third. New York, NY: Springer New York, 2011.

[15] I. Campos-Silva, D. Bravo-Bárcenas, H. Cimenoglu, U. Figueroa-López, M. Flores-Jiménez, and O. Meydanoglu, “The boriding process in CoCrMo alloy: Fracture toughness in cobalt boride coatings,” *Surf. Coatings Technol.*, vol. 260, pp. 362–368, 2014, doi: 10.1016/j.surfcoat.2014.07.092.

[16] O. Al-Mana, M. S. J. Hashmi, and B. S. Yilbas, “Laser nitriding of titanium alloy and fracture toughness measurement of resulting surface,” *Adv. Mater. Res.*, vol. 445, pp. 615–620, 2012, doi: 10.4028/www.scientific.net/AMR.445.615.

[17] S. Zhang, D. Sun, Y. Fu, and H. Du, “Toughness measurement of thin films: a critical review,” *Surf. Coatings Technol.*, vol. 198, no. 1–3, pp. 74–84, Aug. 2005, doi: 10.1016/j.surfcoat.2004.10.021.

[18] F. Sergejev, “Comparative study on indentation fracture toughness measurements of cermets and hardmetals,” *Euro PM 2006 - Powder Metall. Congr. Exhib.*, vol. 1, pp. 43–48, 2006.

[19] P. Pedeferri, *Corrosion Science and Engineering*. 2018. https//doi/ 10.1007/978-3-319-

97625-9.

[20] Trethewey, K R, & Chamberlain, J. *Corrosion for science and engineering, second edition*. United States.

Chapter 4
HIPIMS Low-Pressure Plasma Nitriding

The effect of nitriding voltage (from -500 V to -1100 V) on the structural, microstructure and chemical composition of the specimens are discussed in the first part of this chapter. The second part of the chapter examines mechanical, tribological and electrochemical properties of the untreated and HIPIMS plasma-nitrided specimens (except the samples treated at -500 V). Samples nitrided at -500 V showed an undesirable coating structure which makes it unsuitable for the desired application.

4.1. Microstructural Analysis

The phase composition of the nitrided layers and the untreated surface was investigated by glancing angle X-ray diffraction (GAXRD) at 2° incident angle (figure 4.1). XRD data of the untreated CoCrMo substrate showed a predominantly face-centred cubic (FCC) structure, called γ austenite phase (PDF No: 01-071-4651) with peaks around 44.5° and 51.4° along with a hexagonal closed-packed (HCP) structure, called ε phase (ICDD Powder Diffraction File No: 04-004-4360). It has been reported that both FCC and HCP structures coexist in CoCrMo alloys. However, generally at room temperature the FCC structure is predominant [1 In the case of -500 V, the XRD pattern showed the (111) and (200) reflections of the FCC structured CrN/NbN at 36° 2θ and 42° 2θ respectively, as well as a reflection from Cr_2N at 62.5°. This analysis revealed that at low nitriding voltage (-500 V), a thin (Cr-Nb)-nitride layer was deposited on the sample surface despite intensive re-sputtering of the bombarded surface. It can be stated however that at - 500 V, a nitrided layer is also formed, as revealed by the presence of a higher angle substrate diffraction peak at around 75 °2θ, which corresponds to the ε (110)/

γ (220) phase mixture. On the other hand, samples treated at higher bias voltages (from -700 V to -1100 V) showed γN (111) and γN (200) peaks corresponding to an expanded austenite phase which are shifted to lower 2θ angles compared to the as polished untreated substrate. This shift is mainly due to the expansion of the FCC lattice by the insertion of nitrogen in the octahedral sites of such structure during nitriding, even though residual stress and stacking faults can also cause such lattice expansion. It is important to note that the XRD data of -1000 V and -1100 V also showed traces of CrN and Cr_2N compounds unlike -700 V and -900 V samples. It has been already reported that the precipitation of chromium nitride compounds was observed when the nitriding was carried out at 520 °C [2].

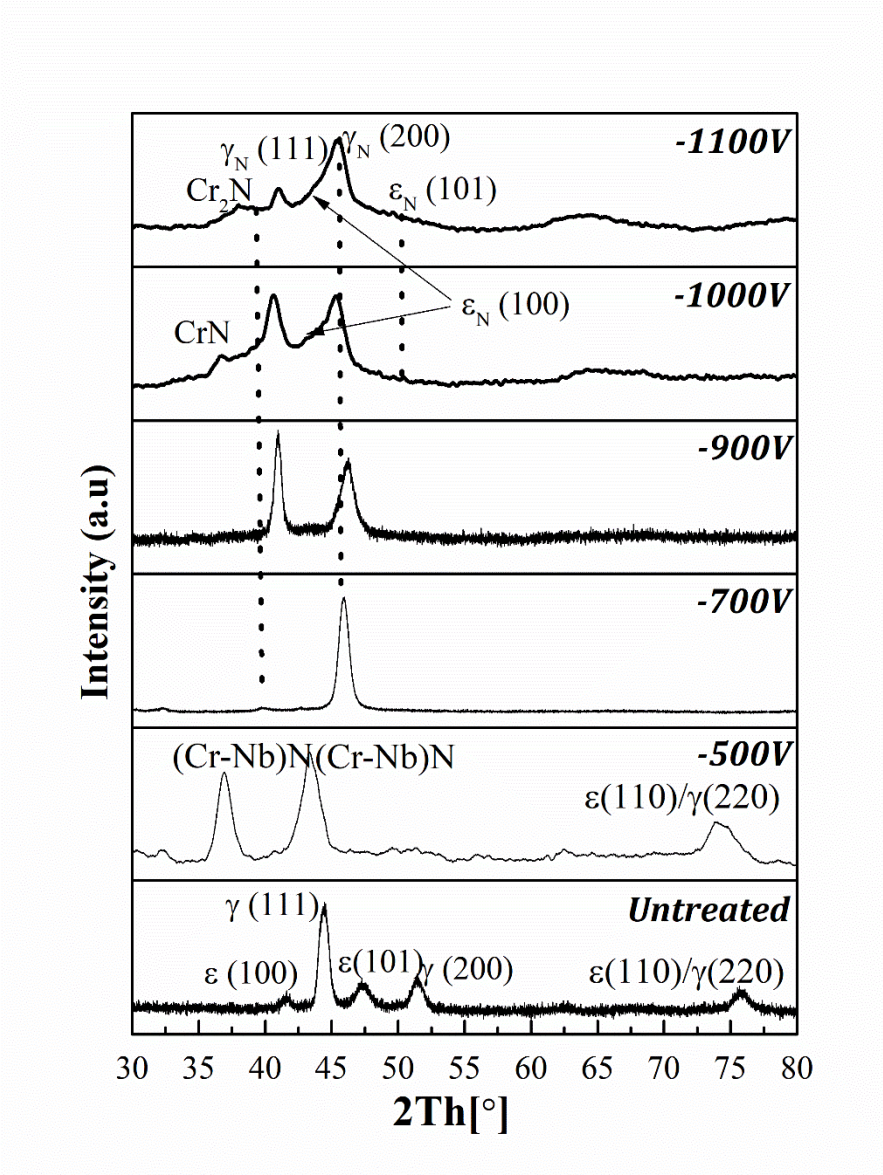

Figure 4-1: X-ray diffraction data of untreated and nitrided samples at various bias voltages.

In this research, during the nitriding of -1000 V and -1100 V samples, the actual process temperature increased up to 510 °C because of the intense ion bombardment due to high bias voltages, even though the set value was much lower at about 400 °C. In the case of -700 V and -900 V samples, the actual process temperature was around 430° C, hence no chromium nitride compound precipitation. Table 4.1 shows peak positions, the calculated interplanar distances (d), lattice parameters (a) and lattice expansions ($\Delta a/a_0$) from the (111) and (200) peaks for the γN phases in the various (nitrided and untreated substrate) samples. The (111) peak in the sample nitrided at -1100 V exhibited a maximum shift of about 3.5° 2θ and the (200) peak in

the -900 V sample showed about a 6° 2θ shift as compared to the substrate peaks. In the [111] direction, the lattice parameter (a) increased significantly from 0.368 nm to 0.384 nm while increasing the bias voltage from -700 V to -1000 V. However, it decreased to 0.370 while further increasing the bias voltage to -1100 V. It is important to highlight that the lattice parameter (a) for austenite cubic (111) phase in equilibrium state is 0.374 according to the Co-N phase diagram. The highest lattice expansion, ($\Delta a/a_0$) of 9.40 % was observed for samples treated at -1000 V as compared to the untreated sample. Therefore, it can be argued that lattice expansion has reached saturation point at -1000 V. In [200] direction, the maximum lattice expansion was found to be 12.99 % for the sample treated at -1000 V as compared to the untreated sample. The lattice expansion, ($\Delta a/a_0$) in [200] direction was found to be higher as compared to [111] direction for all nitrided samples. Similar behaviour was observed by Ozturk et al. [3] for 316 stainless steel alloy. The sample treated at - 1100 V exhibited the highest difference of about two-fold while comparing the lattice expansion in [111] and [200] directions.

Texture coefficient, (T*) was calculated using the following equation, [4]:

$$T^* = \frac{I_{hkl}/R_{hkl}}{(1/n)\sum_0^n (I_{hkl}/R_{hkl})}$$ **Equation 4-1**

Where I(hkl) is the measured peak intensity from the (hkl) reflections, R(hkl) is the reference standard (random) peak intensity from the (hkl) reflections and n is the number of reflections considered. The results from these calculations for all nitrided samples are listed in Table 4.1. The texture analyses revealed that at a lower bias voltage of -700 V, the predominant crystallographic orientation of the nitrided layer is (200) whereas at higher bias voltages (from -900 V to -1100 V), the layer developed mixed (111) and (200) texture.

Table 4-1
d spacings, T* and lattice parameters of untreated, and HIPIMS nitrided at different bias voltage: -700V, -900V, -1000V and -1100V. Note: sample nitrided at -500 V is not included here due to presence of coating phases (Cr-Nb)N. The parameters calculated and presented in table 4-1 only for nitrided layer only.

Sample ID	**2θ°**		**d (nm)**		**a (nm)**		$\frac{\Delta a}{a_0}$***100 (%)**		**T*(%)**	
	γ_N **(111)**	γ_N **(200)**	**(111)**	**(200)**	**(111)**	**(200)**	**(111)**	**(200)**	**(111)**	**(200)**
Untreated	γ (44.53)	γ (51.43)	0.203	0.177	0.351	0.354			-	-
-700V	39.84	45.88	0.213	0.197	0.368	0.394	5.10	11.29	1.51	98.48
-900V	40.91	46.17	0.220	0.196	0.381	0.392	8.56	10.73	43.54	56.45
-1000V	40.57	45.05	0.222	0.200	0.384	0.4	9.40	12.99	33.83	66.16
-1100V	41.05	45.32	0.214	0.199	0.370	0.398	5.41	12.42	28	72

In summary, XRD measurements revealed that the use of HIPIMS discharge with various combination of nitriding voltage has led to changes in phase composition of the nitrided layer. It also confirms that the optimum combination of process parameter provides favourable conditions to develop mix phase nitrided layer [γ_N**(111):** γ_N**(200), 43.54:56.45**].

4.2. Secondary Electron Microscope Study:

4.2.1. **Plan View:**

Figure 4.2a shows the SEM image of the untreated CoCrMo (F75) alloy microstructure. The structure consists of a metastable f.c.c austenite (γ) and h.c.p (γ) phase matrix with a random distribution of metal carbide dendrites [5][6]. To understand the metal carbide composition in depth, EDS (energy dispersive spectroscopy) analysis of the untreated alloy was performed. Results showed that the carbide phases consisted of a mixture of metals (Co, Cr, Mo and Mn) of around 66.7 at% in total with a carbon concentration of around 33.3 at %.

Figure 4.2b shows the carbide phase at high magnification (indicated by a square inset in figure 4.2a) and the chemical composition of the carbide phase (inset table).

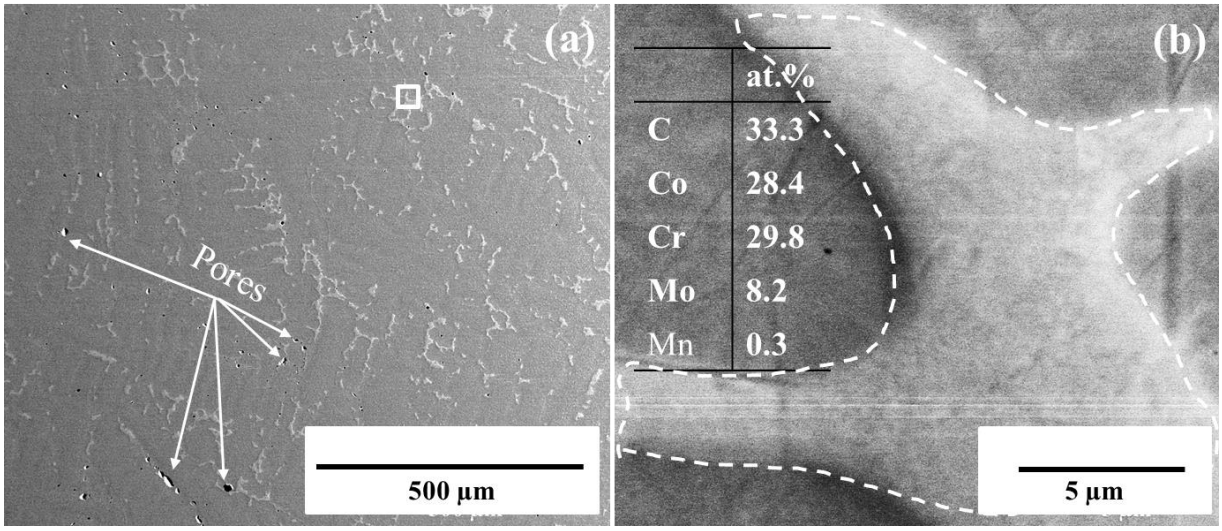

Figure 4-2: (a) Low magnification image of the microstructure of CoCrMo (F75) alloy in plan-view. (b) Selective area EDS analysis of the carbide phase and the results obtained from the compositional EDS analyses.

The metal carbides can be found in different shapes and sizes depending on the crystal structure of the phase. These finely distributed carbides can be identified as $M_{23}C_6$, however the size, transformation (into M_6C) and distribution of this phase can vary based on the manufacturing process and the composition [7][8]. As exhibited in figure 4.2(a), the carbide phases in the microstructure of the alloy used in this study had irregular shapes and sizes. Moreover, they had a dense and blocky appearance which is typical for $M_{23}C_6$ type of metal carbide [7]. Apart from the carbides, porosity (indicated by the circular inset in figure 4.2a) resultant due to the breaking of brittle carbide phases during polishing could also be observed.

Figure 4.3 (a-d) shows the microstructures of the specimens nitrided at different voltages in a plan view. As observed in figure 4.3(a-b) and the XRD results the microstructure of the nitrided layers (-700 and -900 V specimens) consisted of a mixture of equiaxed and elongated grains of γ_N phase and randomly distributed carbides (mainly $M_{23}C_6$ phases) within the γ_N phase. Presence of equiaxed grains of the ϵ_N phase was also visible. Interestingly, γ_N phase dominated the microstructure in the case of the two specimens nitrided at lower voltages.

Microstructure of the specimens treated at higher nitriding voltages (-1000 V, and -1100 V), figure 4.3(c-d), also exhibited equiaxed grains of γ_N phase along with the random distribution of $M_{23}C_6$ carbides. However, a striking difference in the microstructure for these specimens was the presence of ε plates and deformation twins within the γ_N phase grains (inset image of figure 4.3c). In this case, deformation twins were visible at high magnification with the distance between two lines in the range of 60-80 nm. No deformation twins were visible in the case of -1100 V. However, the number of ϵ_N plates within the γ phase increased substantially (figure 4.3d). This implies that higher nitriding voltages (>1000 V and -1100 V in this case) promoted the formation of ϵ_N phase, which makes the surface much harder. Earlier work on HIPIMS plasma nitriding on CoCrMo alloy [9] showed that the texture of these nitrided specimens changed from a predominant (200) orientation (-900 V nitrided specimen) to a mixture of (111) + (200) orientations (-1100V nitrided specimen).

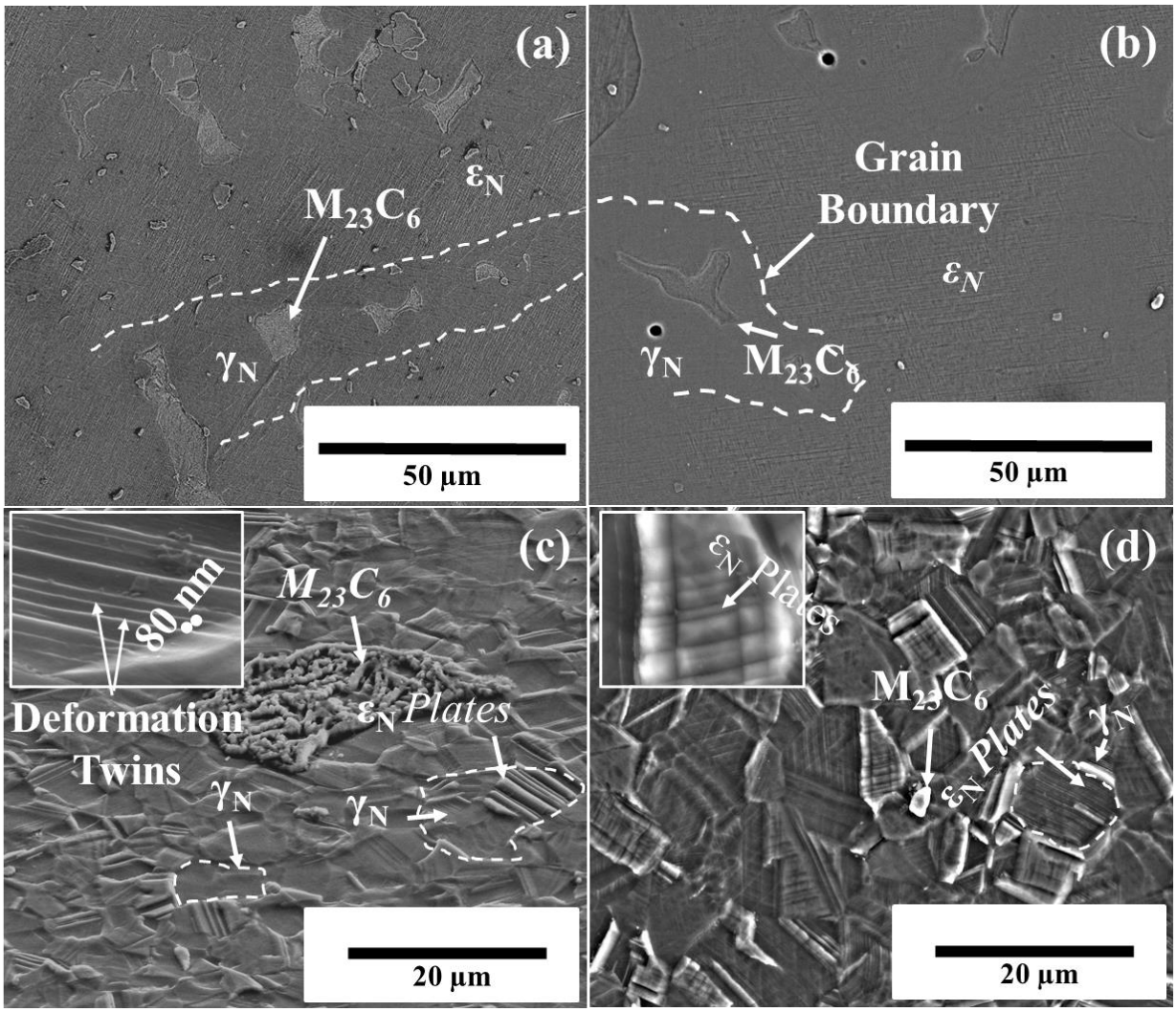

Figure 4-3: SEM microstructure of plasma nitrided CoCrMo alloy at (a) -700 V (b) -900 V (c)-1000 V and (d) -1100 V. Inset images in (c) and (d) show a selected area at a higher magnification with deformation twins and ϵ_N plates respectively.

4.2.2. **Cross-Sectional Analysis:**

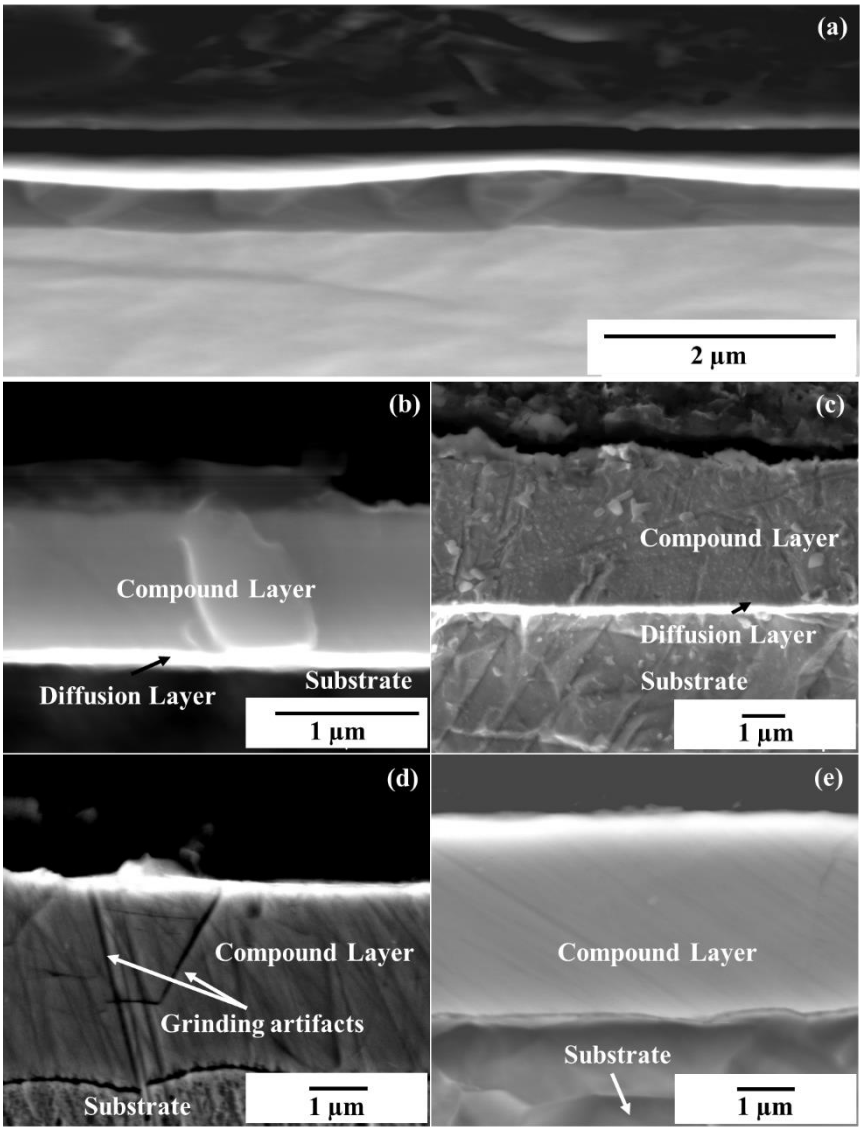

Figure 4-4: Cross-Section SEM images of nitrided samples at various bias voltages (a) -500 V (b) -700 V (c) -900 V (d) -1000 V and (e) -1100 V. (Note: Wight layer indicates diffusion layer, Co_4N and Thick Gray layer indicates compound layer, $Co_{2\text{-}3}N+Co_4N$)

Cross-section SEM images of CoCrMo samples nitrided at various bias voltages are depicted in Figure 4.4a-e. The formation of both compound and diffusion layers can be clearly seen in -700 V and -900 V samples whereas -1100 V and -1000 V sample showed only a compound layer. The diffusion depth measurements using SEM also showed that the depth increased with increasing bias voltage. Maximum depth of about 3.7 µm was observed for the sample treated with -1100 V followed by 3.3 µm, 1.8 µm and 0.97 µm for -1000 V, - 900 V and - 700 V

respectively. EDS analysis (not shown) of these samples showed the absence of target material, Nb in these layers which indicated that these layers are nitrided layers, not (Cr-Nb)N coating.

The sample treated at - 500 V (figure 4.4a) showed a highly dense layer with a unique microstructure as compared to the other samples. EDS analysis of this sample showed that the layer is comprised of Cr, Nb and a small amount of nitrogen. However, it was impossible to establish with EDX that the detected Cr was mainly due to the deposition of (Cr-Nb)N coating as this layer was very thin at approximately 0.97 µm and the substrate also contained a substantial amount of Cr. But the presence of Nb indicated that the deposition of target material has also taken place.

The diffusion depth was roughly estimated because it is not possible to image the whole diffusion layer using SEM. Nevertheless, these values when further defined by EDS corroborated the findings from XRD and SIMS, GDOES analysis.

In summary, SEM analysis revealed that the change in nitriding voltage influences the depth and microstructure of the nitrided layer. It was evident from the analysis that the layer combination changes from mixture of diffusion/compound layer [Co_4N+$Co_{2-3}N$, -700 V and -900 V] to pure compound layer [$Co_{2-3}N$+Cr_2N, -1000 V and -1100 V]. Also, increase in bias voltage increases the thickness of nitrided layer significantly. Therefore, effect of bias voltage on microstructure and thickness was investigated.

4.3. Elemental Depth Analysis (SIMS and GDOES):

Generally, duplex nitrided layers such as diffusion layer (Co_4N) and compound layer ($Co_{2-3}N$) are formed during the nitriding of CoCrMo alloy [10][11]. According to the Co-N equilibrium phase diagram, at 400 °C, Co_4N is formed when the concentration of N is about 20 at. % [12]. Further increase in the nitrogen concentration will lead to the formation of other under-stoichiometric Co based nitrides such as Co_3N and Co_2N followed by the stoichiometric

CoN when the concentration of N is 50 at. % [11]. The elemental depth profiles of treated samples obtained using glow discharge optical emission spectroscopy (GDOES) are depicted in figure 4.5(a-b). Generally, nitrogen depth profile exhibits plateau-type shapes with sharp leading edges [10]. For samples treated at higher bias voltages (from -700 V to -1100 V),

initially, the concentration of nitrogen was about 40 at. % and stable up to a certain depth which then gradually decreased to the lowest value before remaining almost constant.

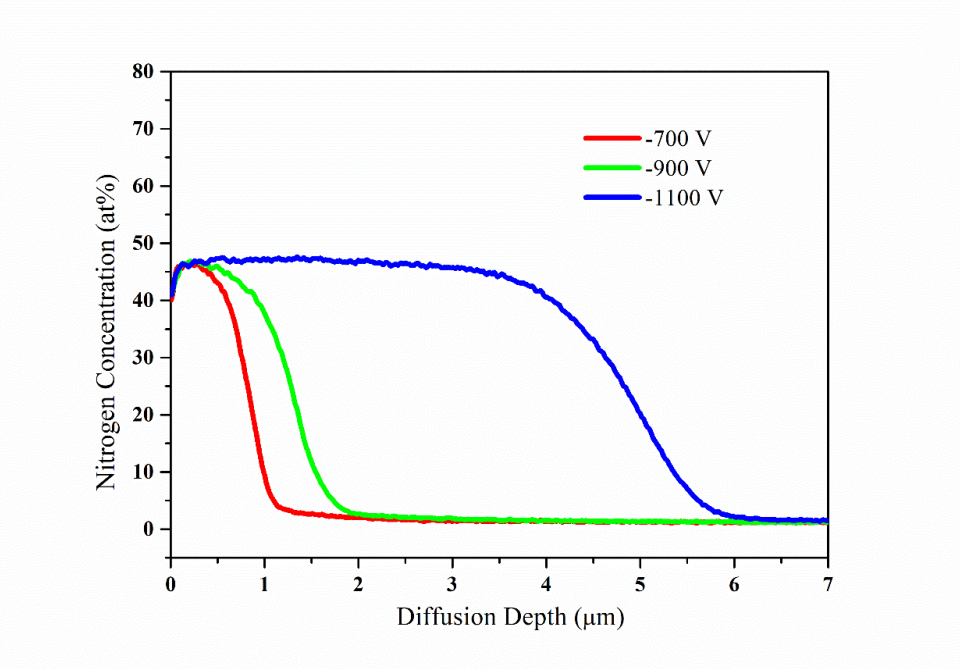

(a)

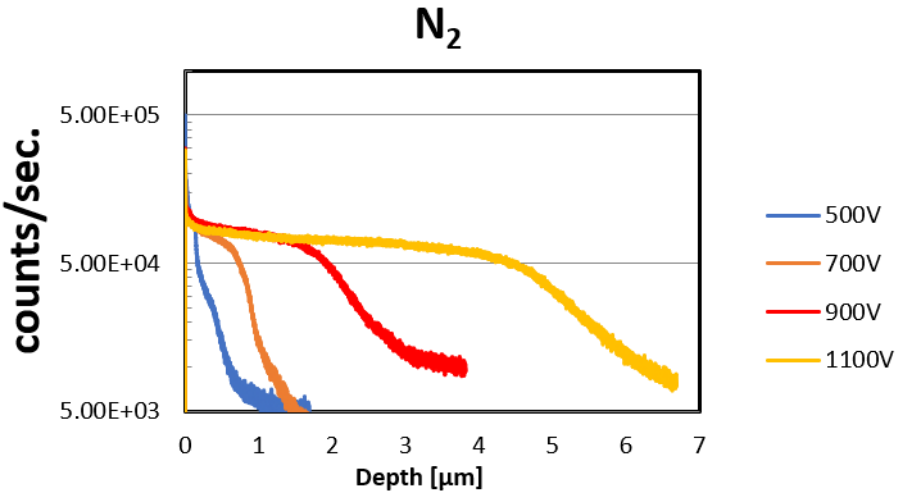

(b)

Figure 4-5: (a) GDOES nitrogen depth profile of -700 V, -900 V and -1100 V (b) SIMS nitrogen depth profiles of nitrided samples at various bias voltages including -500 V.

The diffusion depth was found to be increased while increasing the bias voltage from -700 V to -1100 V. It has been reported that the optimum energy needed to form a deep nitrided layer was of about 1 keV. In this study, the sample with the highest bias voltage of 1100 V (1.1 keV) showed the maximum diffusion depth of about 6 µm. At this energy level, the density of N^{2+} and N^{+} ions was found to be increased threefold as compared to 0.5 keV as evidenced by the corresponding increase in substrate bias current. Constant currents and voltages at the cathodes indicated a constant plasma density was generated in the chamber. The substrate bias currents (both average and peak) were proportional to the bias voltage due to the increased area of collection by each sample associated with an increased sheath width. The data confirms our earlier plasma density measurements in the same operating range [13]. Additionally, the intensive ion bombardment generates defects on the surface for these ions to diffuse faster, (ion irradiation enhanced diffusion). The dissociation of neutral N_2 into ions was also achieved by igniting Cr and Nb targets using HIPIMS/UBM sources at low power densities. The diffusion depth of the other two samples with bias voltages of -700 V and - 900 V was 1.2 µm and 2 µm respectively.

The formation of these layers can be explained by the diffusion model proposed for stainless steel by Williamson et al, 1992 [14] due to the similarity of CoCr to stainless steel [15]. According to this model, the Cr atoms act as trapping sites for N and inhibit the diffusion until all Cr trap sites are occupied, resulting in a nitrogen rich compound layer. Subsequently, further incoming N diffuses freely through the compound layer into the substrate, producing transition and diffusion zones, respectively. Also, this model was further refined by Parascondola et al. [16] which included a thermal de-trapping mechanism of N from trap sites with detrapping activation energy of 1.45 eV. Akvile Petraitiene et al. [15] adapted this model for CoCr which consisted of nitrogen adsorption on the surface, nitrogen concentration dependent diffusion coefficient of nitrogen and alloy's swelling processes.

The sample treated at -500 V showed a slightly different (very thin plateau) profile with highest nitrogen concentration of about 40 at. % up to ~200 nm depth which then sharply decreased to 25 at. % before gradually reducing to the lowest level shown in figure 4-5a. Notably, the concentration of Cr increased sharply up to 18 at. % before following the similar trend observed for the other treated samples. Also, it is important to highlight that the concentration of target material, Nb, was found to be approx. 13 at. % in this region unlike the other nitrided samples. Therefore, this thin layer can be attributed to the deposition of a thin (Cr-Nb) N coating. Also, it can be argued that diffusion of nitrogen has also taken place since the nitrogen concentration didn't reduce to zero immediately after the coating and this can be correlated with XRD data obtained for this sample. (Refer section 4.1).

In summary, utilisation of HIPIMS discharge led to diffusion of nitrogen faster and deeper with change in bias voltage. The amount of nitrogen diffused within the compound layer was found to be twice the value reported in literatures. Note: concentration of nitrogen and other elements were compared with standards to conclude the quantitative analysis. Further, GDOES and SIMS data were compared to stablish the contribution of each element mainly nitrogen within layer.

4.4. Surface Roughness Analysis:

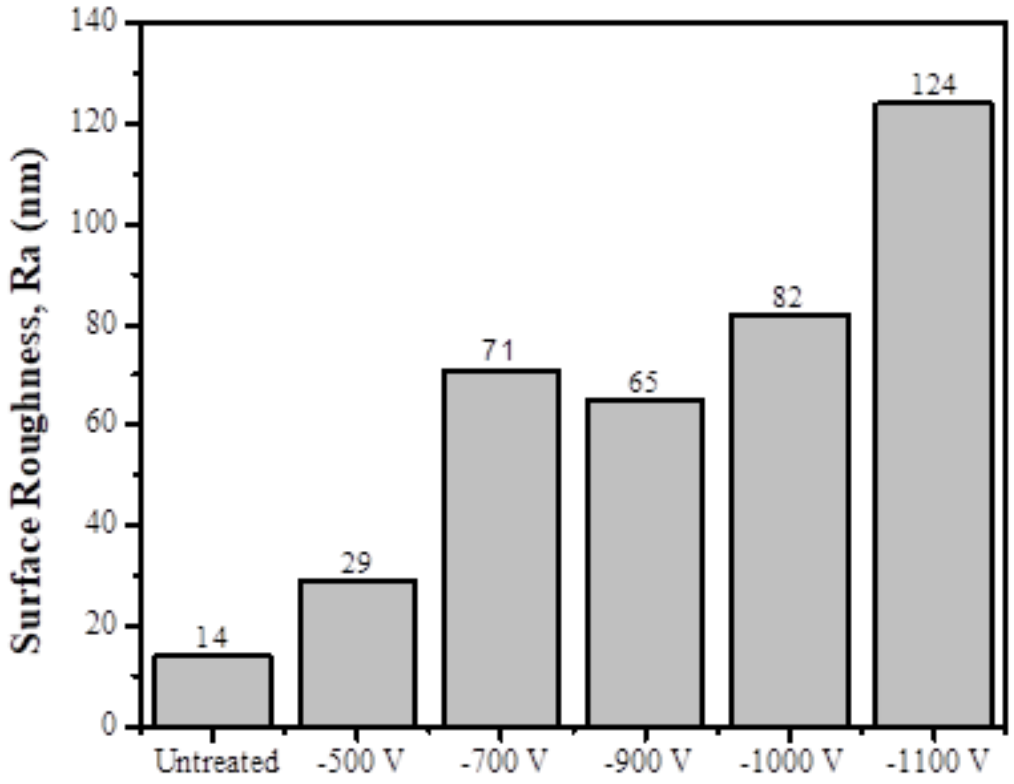

Figure 4-6: Surface roughness values of the untreated and nitrided specimens.

A Dektak profilometer was used to measure the surface roughness of the samples. As can be seen from figure 4.6, the Ra value of the untreated sample was in a range of 15 nm to 20 nm after polishing with (1 µm) diamond slurry. The lowest R_a value of 29 nm was recorded for the sample that was partially nitrided at -500 V whereas the -1100 V sample showed the highest value of 124 nm. The roughness value of the samples treated with -700 V, - 900 V and -1000 V was found to be 71 nm, 65 nm, and 82 nm respectively. It is important to note that the roughness value increased two-fold while increasing the bias voltage from -900 V to -1100 V. The increase in roughness value can be attributed to the intense bombardment of highly energetic N/H and metal ions at higher bias voltages which produces a significant surface sputtering effect. The roughness will be further influenced by the lattice volume expansion due

to the incorporation of nitrogen into the metallic lattice during the nitriding process. The results summarised in Table 4-1 clearly demonstrate this trend where the lattice expansion ($\frac{\Delta a}{a_0}$) for both (111) and (200) orientations follow the increase of the nitriding voltage.

4.5. Mechanical Studies

This section discusses in detail mechanical properties such as microhardness, nanohardness, fracture toughness, impact load fatigue, toughness etc. of the untreated and nitrided specimens. Sample nitrided at -500 V has been excluded from the study such as fracture toughness and impact fatigue analysis as it is coating and does not fit the requirement of the application.

4.5.1. **Microhardness Analysis**

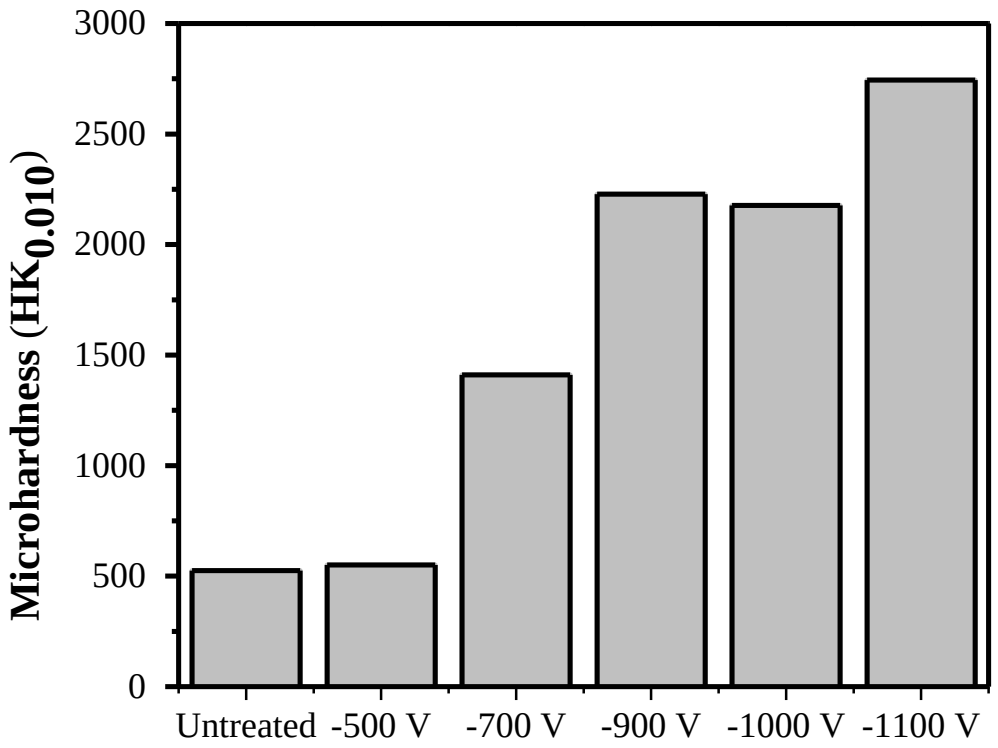

Figure 4-7: Microhardness value of the untreated and nitrided specimens. Note: Observed error was around 10 %.

Figure 4.7 shows the surface microhardness data of untreated and nitrided CoCr samples at various bias voltages. To measure only the microhardness of the nitrided layer eliminating the substrate effect, the applied load was kept fixed to 10 g. The surface hardness of treated samples with high bias voltages (from -700 V to -1100 V) increased considerably as compared to untreated CoCr alloy due to the formation of expanded austenite phase. The maximum hardness value of about 2750 $HK_{0.010}$ at 10 g applied load was observed for the sample treated at -1100 V which was about five orders of magnitude higher that of the untreated sample, 525 $HK_{0.010}$. The samples treated with -700 V, -900 V and -1000 V exhibited hardness values of 1410 $HK_{0.010}$, 2230 $HK_{0.010}$ and 2180 $HK_{0.010}$ respectively for the same applied load. The increase in microhardness while increasing the bias voltage could be attributed to the increase in nitriding depth and the compressive stress in (γ_N) phase due to high ion bombardment [8][10][17]. On the other hand, the surface hardness of the sample treated with relatively low bias voltage, -500 V exhibited a very low hardness of 550 $HK_{0.010}$, even at a low load of 10 g due to the very thin nitrogen diffusion layer at this voltage which allows for substrate hardness interference.

4.5.2. **Fracture Toughness (K_{Ic}) Analysis:**

To evaluate the fracture toughness value K_{Ic} of the relatively thin nitrided layer, an alternative method based on vickers indentation was used on HIPIMS nitrided and the untreated alloys [18]-[22]. In this indentation based method, the contact pressure is independent of the indentation size (IDS) and the quality of the indentation is evaluated in terms of plastic deformation and crack propagation from the edges and corners of the residual indentation impression. A STRUERS microhardness tester equipped with a pyramidal shape Vickers indenter was used to make indentations. A fixed and excesivelly high penetration load of 50 kgf was applied irrespective of the nitrided layer thickness in order to promote crack initiation.

Figure 4.8 shows the calculated K_{Ic} value for the untreated and the nitrided specimens at different nitriding voltages. K_{Ic} value for the untreated specimen was around 906.9 MPamm$^{1/2}$ a relatively high value as expected for the softer base material, (figure 4.7). The highest K_{Ic} value of 1011.7 MPamm$^{1/2}$ was found for the -700 V specimen. A further increase in the nitriding voltage (-900 V) deteriorated the K_{Ic} value to 872.9 MPamm$^{1/2}$. However this value increased further as the nitriding voltage increased from -900 V to -1100 V, as shown in figure 8. The change in K_{Ic} value could be linked to the change in the texture of the compound layer [23]. The texture analyses of the specimen nitrided with -700 V showed that the predominant crystallographic orientation of the compound layer was (200). Whereas, at higher nitriding voltage from -900 V to -1100, the compound layer developed a mixed texture of (111) and (200). As the volume fraction of (200) texture increased from 56.42 % (-900 V) to 72 % (-1100 V), the fracture toughness value showed an increment accordingly (prefer Table 4-1).

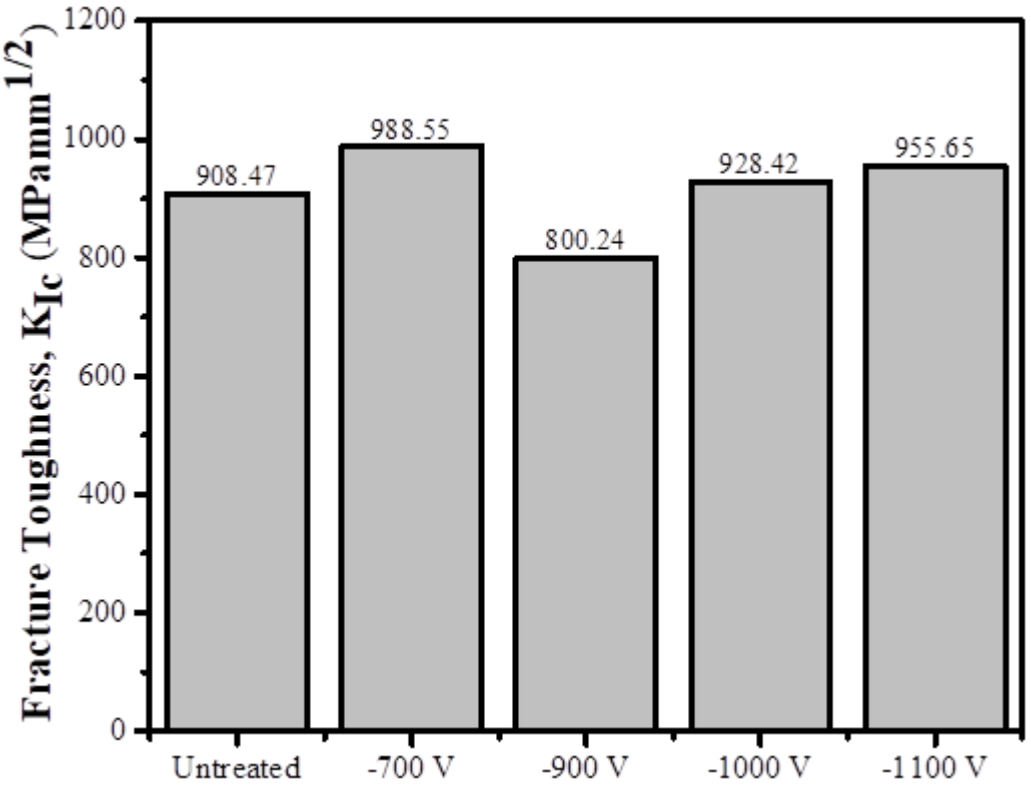

Figure 4-8: Calculated fracture toughness (*KIc*) values of the untreated and specimens nitrided at −700 V to −1100 V (Note: the error was within ±10 %) .

Investigation of the surface morphology of the impression after indentation is also essential in order to evaluate the resistance of the nitrided alloys against cracking. In the Vickers indentation method, usually, two kinds of crack modes namely Palmquist and radial cracking along the edges of the indenter, can be observed [21]. As per the formula (equation 3-10), K_{Ic} is inversely proportional to the crack length formed along the edges of the indentation after unloading. Figure 4.9(a-c) shows the indentation impression on the surface of the untreated specimen for a fixed normal load of 50 kgf. No evidence of any types of cracks along the edges of the square impression due to a fracture was evident in the SEM studies. This suggested that the untreated alloy had high resistance against cracking as expected for a lower hardness and high plasticity material. However, high magnification SEM analysis showed shear cracking along the diagonals of the impression (figure 4.9b).

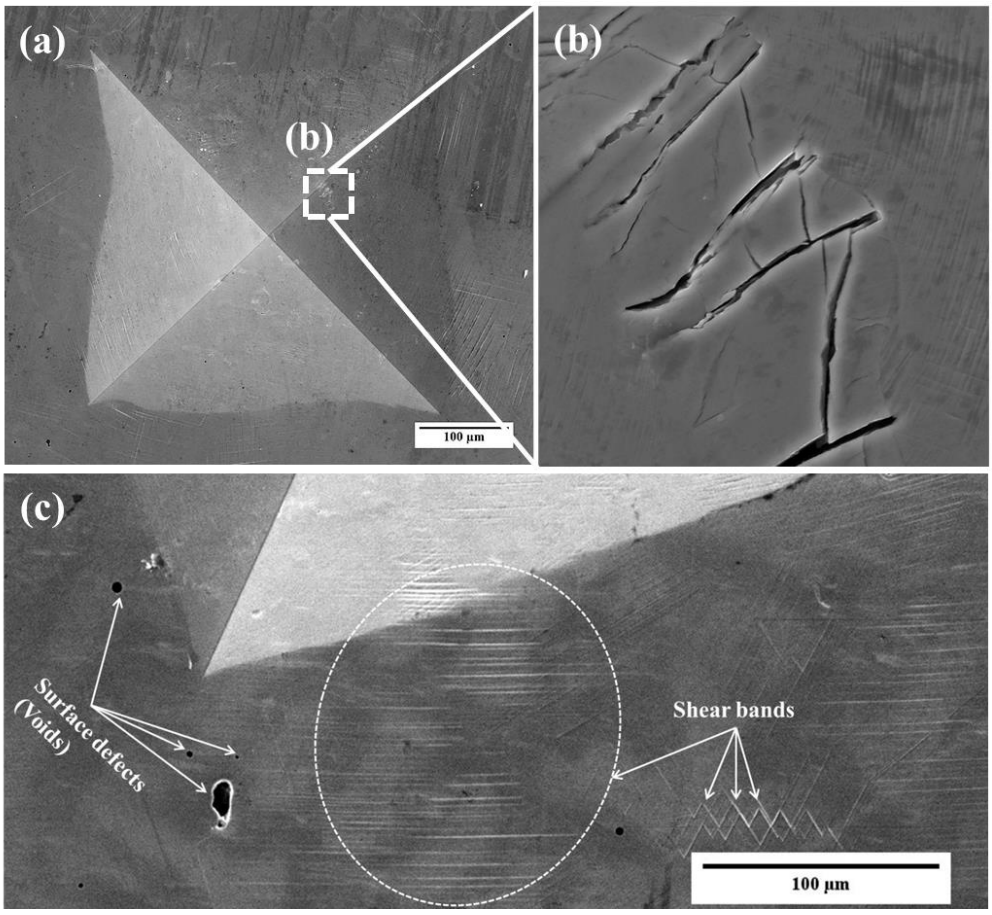

Figure 4-9: SEM images of microindanatation on the untreated specimen (b) a high magnification image of the deformed area along the diagonal and (c) area near the edge and corner of the square impression.

Formations of such crack can be attributed to the manufacturing defects (micro-voids) and the associated localised strain around them. Further analysis of the area around the indentations showed that the surface deformed plastically during the loading-unloading cycle, which was also made evident due to the presence of shear bands, [24] around the indentation (figure 4.9c).

In this case, the area around the square edges and corresponding corners of the impression were found crack free which indicates a good fracture toughness of the nitrided layer. However, further detailed surface analyses revealed interesting features of the deformation behaviour of such layers. For example, shear cracks were found in the areas near to the intersection of the diagonals (figure 4.10b) and very adjacent to the diagonals formed due to the point load concentration and high strain rates. Figure 10c shows the area where the diagonals meet at one of the corners of the square impression. In this image, shear bands along with the cracks and the surface texture of the nitrided surface were prominantly evident.

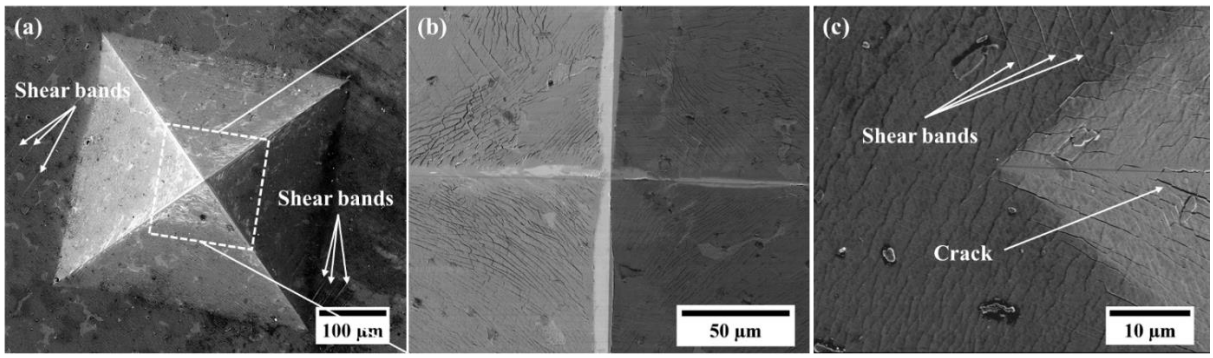

Figure 4-10: (a-c) shows the indentation made on the specimen nitrided at -700 V.

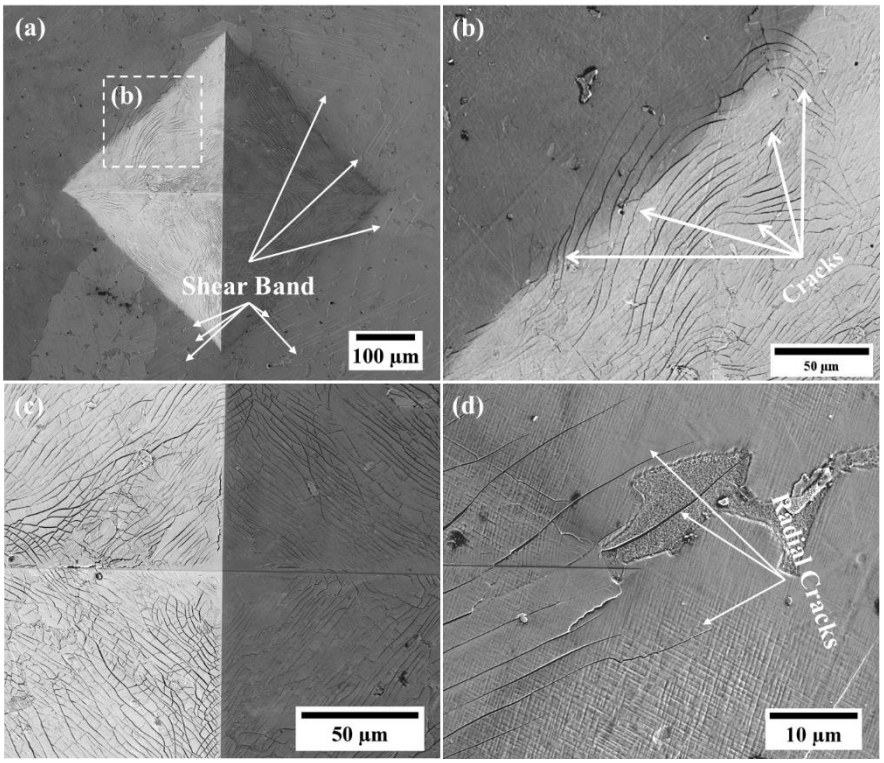

Figure 4-11: SEM images of (a) the indent on the surface of the specimen nitrided at −900 V (c) high magnification image of center of the impression and (d) one ofvthe edges of the square impression.

For specimens at higher nitriding voltages of -900 V, -1000 V and -1100 V, both Palmquist and radial mean type cracks were detected. Most of these cracks had their origin and extinction within the faces of the impressions, which followed the direction of loading. For specimens nitrided with -900 V, initiation and propagation of these cracks (Palmquist and radial) can be seen in figure 4.11(a-d). They were predominantly present around the boundary of the square impression (figure 4.11(a-b)). Similar to -700 V specimen, the cracks within the center of impression (figure. 4.11c) were found, but with higher density. Figure 11(d) shows a high magnification image of the radial cracks near the edges of the square. Apart from these cracks, shear bands which were further forced away from the indentation were also found (Fig. 11a). It is considered that hemispherical plastic zone (or semi-circular plastic zone) and radial stresses are responsible for the formation of these primary shear bands during the indentation [25][26][27].

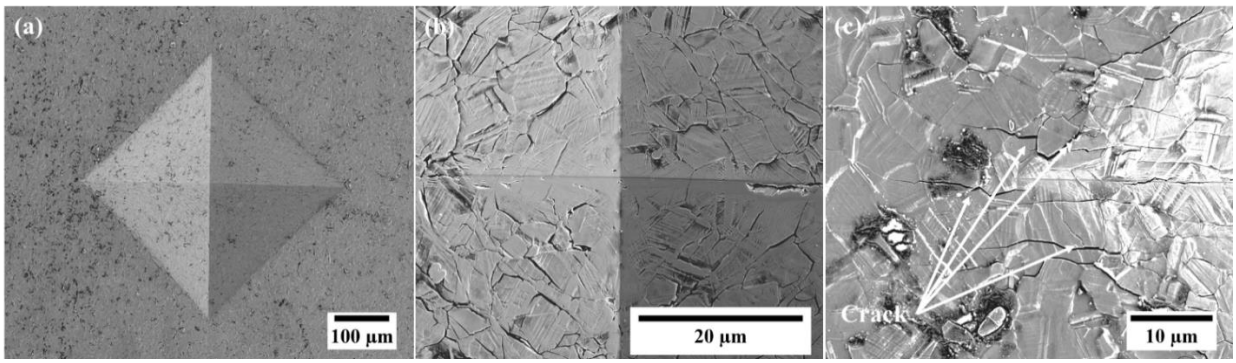

Figure 4-12: SEM images of (a) indents on the surface of the specimens nitrided at -1000 V (b) high magnification image of center of the impression and (c) one of the edges of the square impression.

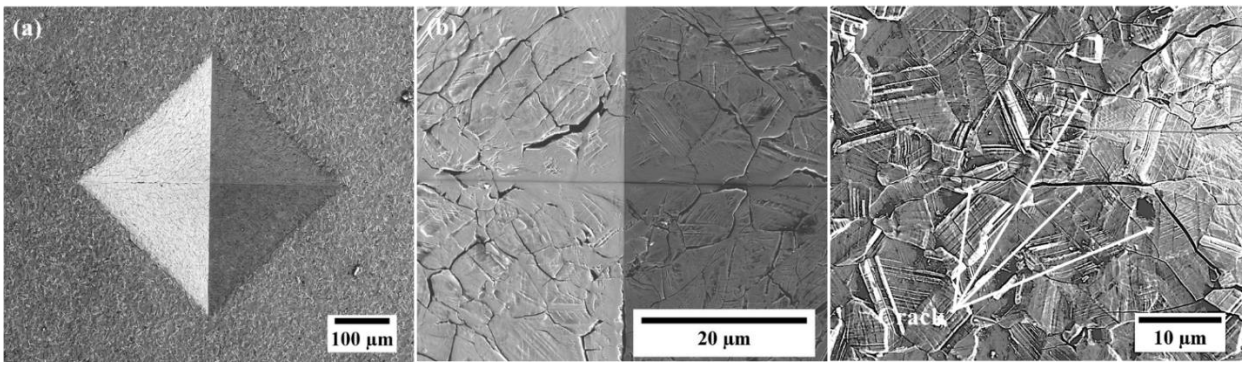

Figure 4-13: SEM images of (a) indents on the surface of the specimens nitrided at −1100 V (b) high magnification image of center of the impression and (c) one of the edges of the square.

Figures 4.12(a-c)-4.13(a-c) exhibit the impression after indentation on the specimens treated at -1000 V and -1100 V respectively. It can be concluded from the above images that as nitriding voltage increased from -1000 V to -1100 V, the number of radial cracks along the edges and around the corners decreased while the cracks within the impression (pyramidal faces) increased in population and became wider and symmetrical.

Table 4-2

Nanohardness (Hp). Young's modulus (E), Indentation depth after unloading (I_d), calculated elastic (H/E) and plastic (H^3/E^2) index of the untreated and nitrided specimens.

Sample ID	Hp (GPa)	E (GPa)	I_d (nm)	H^3/E^2 (GPa)	H/E (GPa)
Untreated	8.0	249±5.0		0.01	0.03

-700	22.0	266±4.0	21	0.15	0.08
-900	23.0	290±4.0	22	0.14	0.08
-1000	21.0	272±14.0	32	0.13	0.08
-1100	23.0	343±31.0	22	0.1	0.07

The difference in the fracture behaviour of the layers nitrided at lower voltages (-700 V, - 900 V) as compared to those produced at higher nitriding voltagees, (- 1000 V, - 1100 V) can be explained on the basis of specific hardness to Young's modulus ratios. A layer with a high value of H^3/E^2 ratio designates the surface to be of a high toughness with reduced plastic deformation. Also, a high H/E ratio defines the crack density, which means specimens with a high H/E ratio will have less crack population than the specimen with the lower value of H/E [28]. In our work, we also found similar trends where H/E (table 4-2) ratio decreased with an increase in nitriding voltage. Hence in this work, -700 V specimen was found to be having the best K_{Ic} value since it had the least crack population (Palmquist and Radial) despite being the thinnest of all nitrided layers. However, when compared to the untreated alloy properties the HIPIMS plasma nitrided layers consistently showed a significant hardness increase and significant increase of the H^3/E^2 values in some cases up to almost two orders of magnitude, (see Table 4.2) and therefore enhanced fracture toughness.

It has been widely reported that state of the art nitriding improves hardness, but results in surface embrittlement [29][30]. In our case, similar hardness increase was observed associated with the changes in the phase composition of the nitrided layer. However, in this work, we found that as the nitriding voltage increased the number of the shear band (after impact load tests) decreased which evidenced an improvement in the fracture toughness of the treated layers. In addition to the above made argument regarding increased K_{Ic} values, it can be speculated that this unusual behaviour is also due to structure specific properties namely

nitrided layer density. This is expeted to be much higher thanks to the high energy ion bombardment, (ion peening) achieved with utilisation of the highly ionised HIPIMS discharge.

4.5.3. **Load Macro Impact Fatigue Analysis:**

In order to evaluate the effectiveness of the nitriding process, the impact resistance response of the specimens was tested using a dedicated impact load tester. In this test, a fixed normal load of 500 N was applied, whereas the number of total impacts was varied to better trace the impact size progression with time. For each specimen, the test was interrupted initially after 250 impacts and then progressed to 1×10^6 impacts. The profile of the resulted crater were studied using a Dektak Stylus profilometer by conducting a linear scan across the crater after each stage.. The values of the initial crater depth (d_i) after 250 impacts and final, crater depth (d_f) after 1×10^6 impacts are shown in figure 4.14.

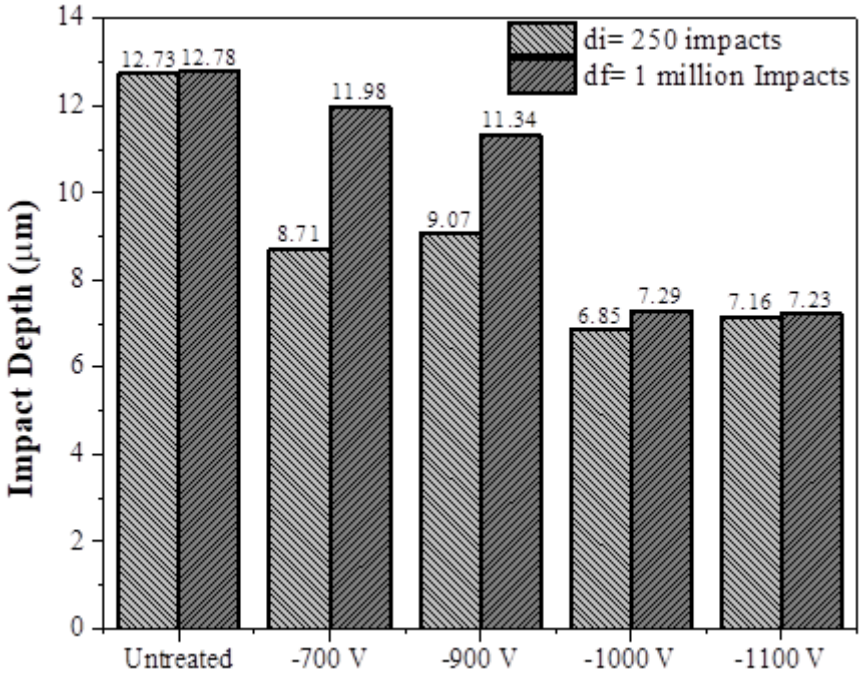

Figure 4-14: Impact crater depth values of the untreated and the nitrided specimens after initial impacts (250) and final impact (one million impacts).

From figure 4.14, it is apparent that the deepest crater, after both, 250 and 1×10^6 impacts were observed for the untreated alloy, which was around 12.73 µm. The HIPIMS plasma nitrided specimens showed a better response against both initial and final impacts compared to

the untreated specimen. In the case of the specimen nitrided at -1100 V, the values of d_i= 7.16 µm and d_f = 7.23 µm observed respectively were the lowest values amongst the specimens investigated. The steady decrease in both d_i and d_f values with an increasing nitriding voltage demonstrated that nitriding significantly improved the impact load resistance of the surface of the CoCrMo alloy.

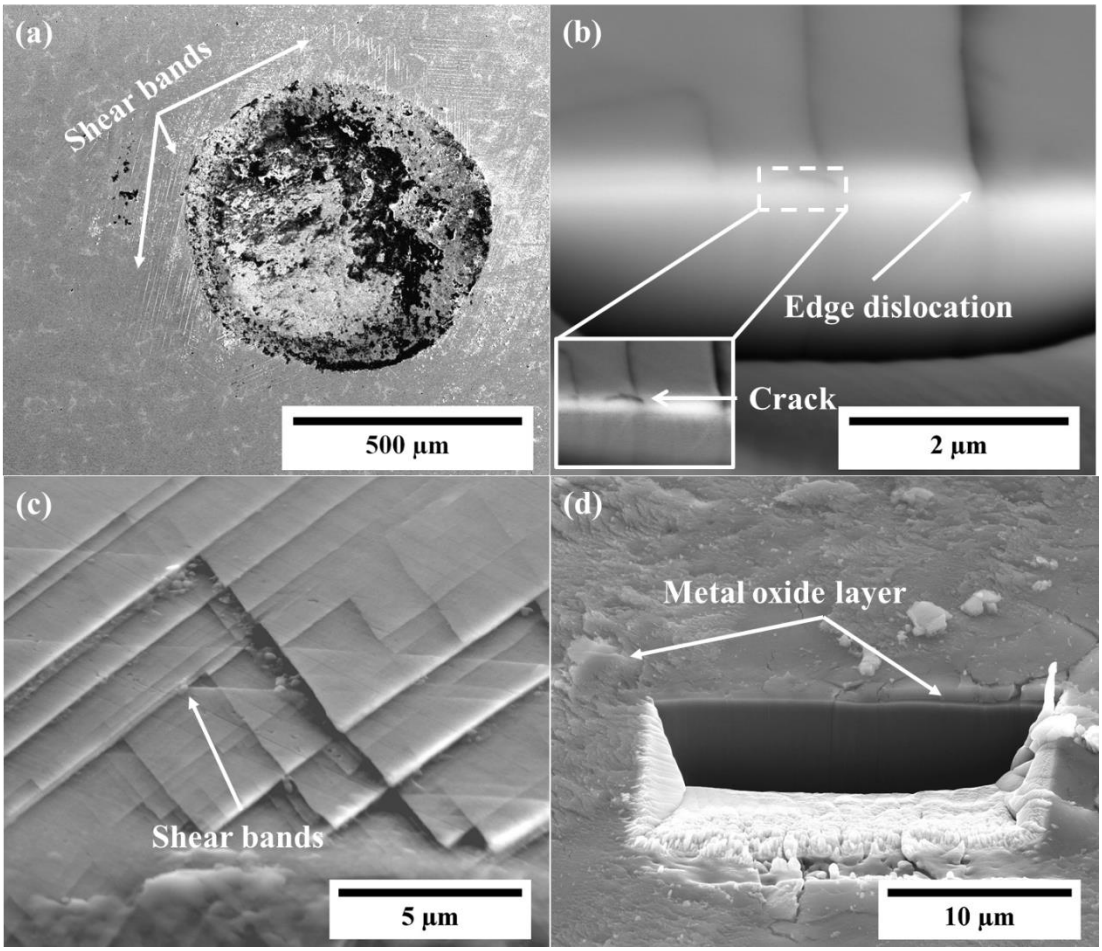

Figure 4-15: SEM images (a) impact crater on the untreated alloy after 1.106 impacts, (b) FIB cross-section near shear bands (SB) (c) SB near the impact crater and (d) FIB-CS in zone 2 (middle) of the impact crater.

Figure 4.15(a), shows the crater surface morphology of the untreated alloy after one million impacts. The impact area can be divided into two different zones; Zone 1: the area around the periphery of the crater and Zone 2: middle of the crater. Zone-1 distinctively showed an accumulation of wear debris displaced from the impact crater. High magnification SEM image of zone-1 revealed that the surface deformed via a continuous formation of shear bands

(parallel to each other). These bands appeared to criss-cross each other, as shown in figure 4.15(c). Also, cracks near the bottom of these shear bands were detected in the *FIB-CS* ((Focused Ion Beam-cross section), figure 4.15b). On the other hand, in zone 2, the crater was found with islands of metal oxides adhered to the base metal which had a thickness of about 0.7 µm confirmed via *FIB-CS* and *EDS* (Energy Dispersive Spectroscopy) elemental mapping (figure 4.15d and 4.17 respectively). Despite the high number of impacts of one million, no evidence of any crack formation in the underneath material was observed in this zone. It is believed that plastic deformation, oxidation of the surface followed by subsequent removal of these oxides due to cracking seemed to be the main mechanism of crater formation.

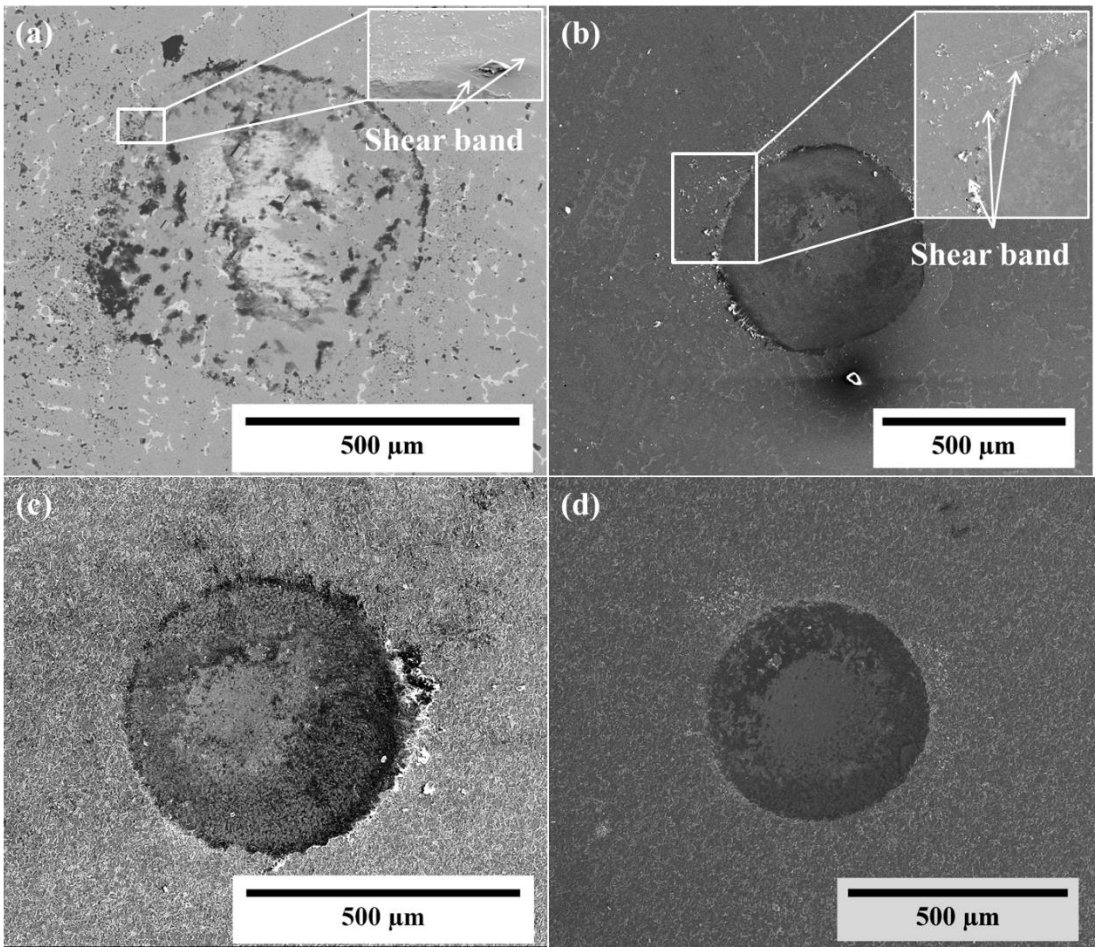

Figure 4-16: SEM images of impact craters on the specimens nitrided at (a) -700 V (b) -900 V (c) -1000 V and (d) -1100 V after one million impacts.

The impact crater surface analysis of specimen nitrided at -700 V to -1100 V revealed that in this voltage range the diameter (and consequently the depth of the craters) reduced with higher rate from 575 µm for -700 V to 518 µm for -1100 V as shown in figure 4.16 and 4.14. However, in all cases the increase in nitriding voltage resulted in an improvement in impact resistance of the nitrided layer which can be attributed to the synergistic effect of the changes in thickness, surface texture, microstructure, phase composition and hardness on the increase in the shock-absorbing capacity of the nitrided layer.

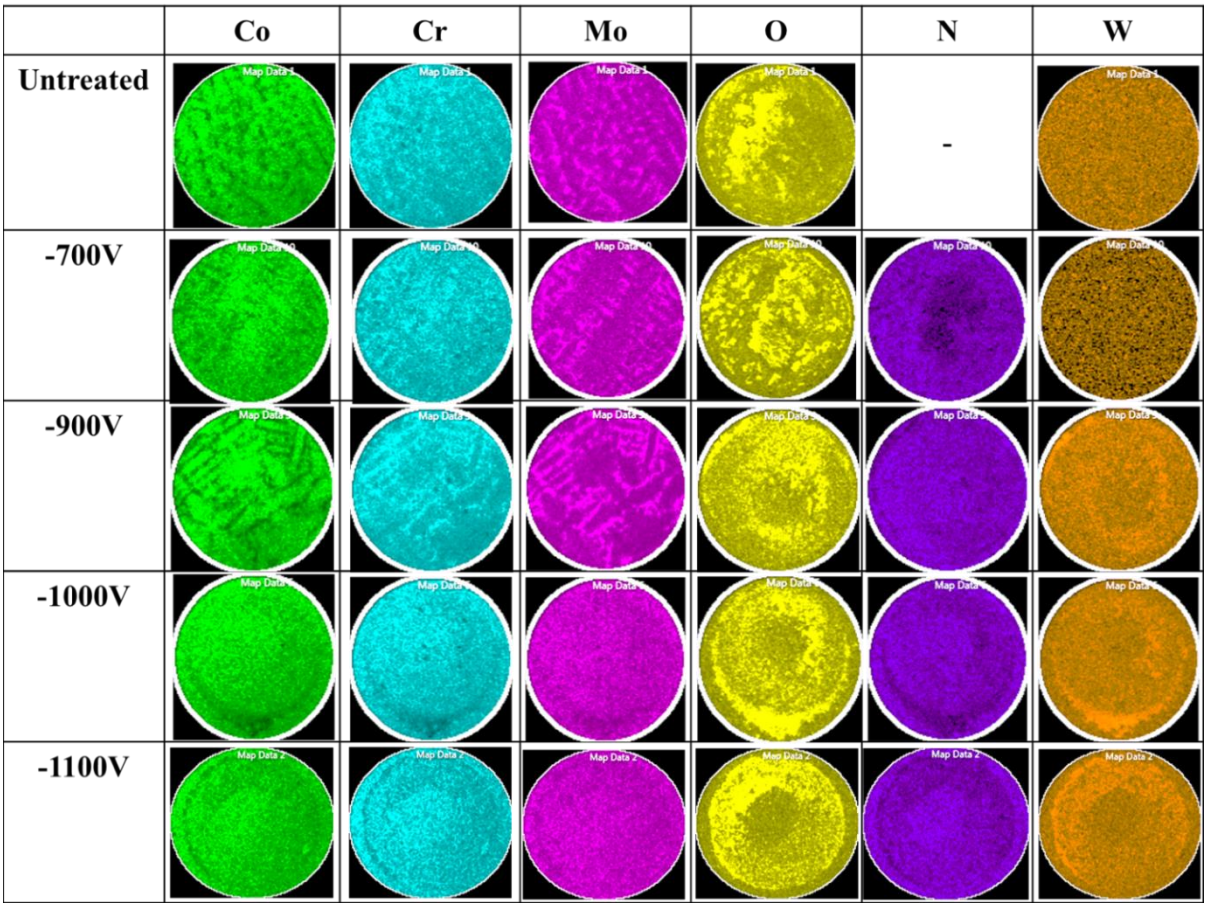

Figure 4-17: EDS elemental mapping of impact craters on the untreated and plasma nitrided specimens at -700 V to -1100 V.

EDS elemental mapping was performed to better understand the chemistry of the various compounds formed on the surface of the craters. The colour coded EDS elemental maps are shown in figure 4.17. In general, the brighter the colour (assigned to an element) in the map, the higher is the concentration of that element. In addition to the main elements such as

Cobalt (Co), Chromium (Cr) and Molybdenum (Mo) of the alloy and Nitrogen (N) due to the treatment, the elements Oxygen (O) and Tungsten (W) were also investigated to reveal the effect of the surrounding environment (impact due to oxidation) and potential material transfer due to the impact wear of the WC counterpart. The analyses showed that the crater surface of the specimen nitrided at -700V was fully covered with an oxide layer. The amount of oxide formation reduced gradually as the voltage increased from -900 V to -1100 V, as shown in figure 4.17 and FIB-CS images, figure 4.18(c-d). One possible reason for this behaviour could be the increase in the amount of CrN/Cr_2N in the nitrided layers. In concurrence, the material transfer from the WC counterpart also increased. This behaviour can be attributed to the overall increased hardness and toughness of the nitrided layer.

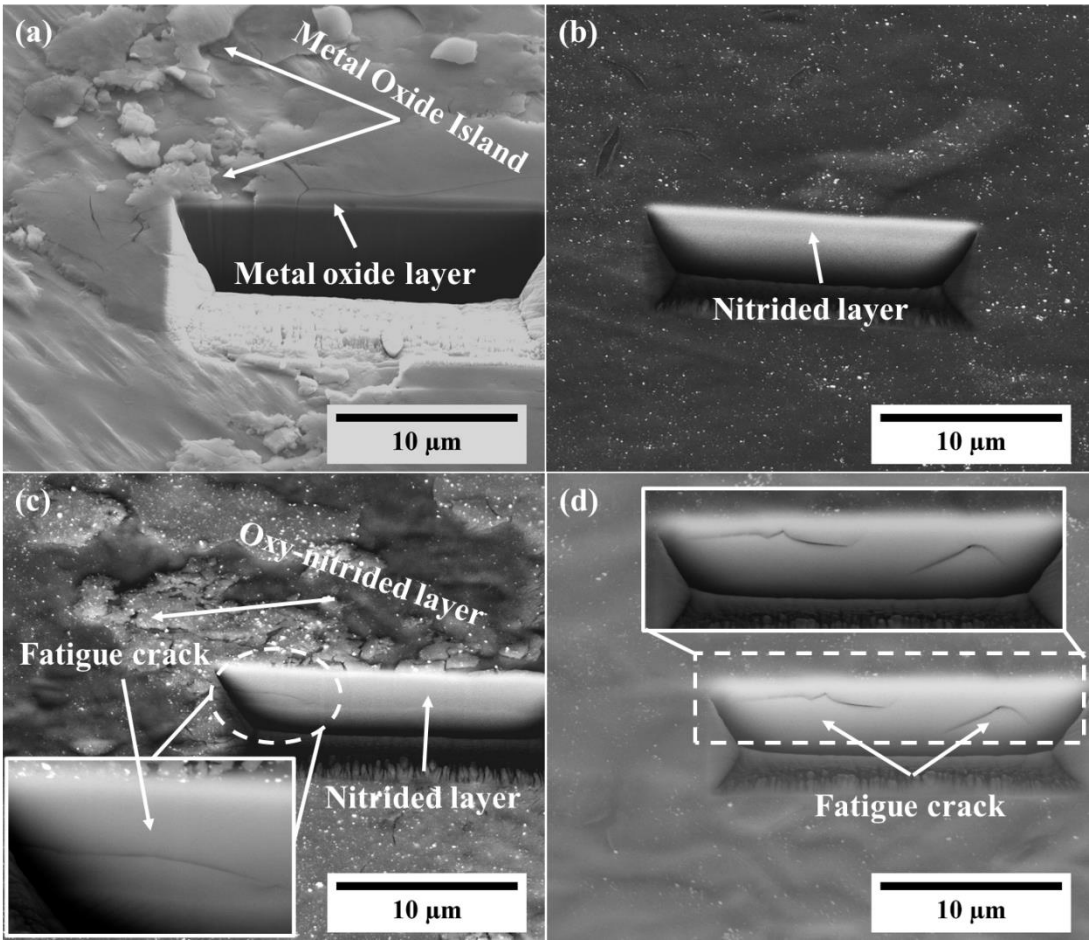

Figure 4-18: Sub-surface SEM micrographs of impact craters on the specimens nitrided at (a) -700 V (b) -900 V (c) -1000 V and (d) -1100 V.

The sub-surface microstructure of the material beneath the impact craters of the nitrided specimens was investigated by FIB-SEM analyses, figure 4.18. In the case of specimens nitrided at -1000 V and -1100 V (figure 4.18c-d), fatigue cracks within the base metal beneath the nitrided layer were observed. Interestingly, no such cracks were observed in -700 V and -900 V specimens. In this study, the nitrided layers formed at -900 V showed the best combination of oxidation resistance and impact energy damping capability. Whereas, in the case of -1000 V to -1100 V, impact energy absorbed by nitrided layers has transferred to the base metal resulting in crack formation.

An important correlation between the plasticity index, H^3/E^2 and impact response was presented by Chen and co-workers in 2011 where they found that the specimen with higher plasticity index, (H^3/E^2) was found to have a better response against nano impact [19].

Table 4.1 and 4.2 summarises the data regarding the surface nanohardness (H), elastic modulus (E), texture coefficient (T*), elastic index (H/E) and plasticity index (H^3/E^2). It can be stated that whilst the hardness values of the nitrided layers produced at different nitriding voltages were found approximately similar, the E values showed an increase from 265.5 GPa for -700 V to 343.1 GPa for -1100 V. This is reflected by the values of the plasticity index where the maximum plasticity index, H^3/E^2 (H= 22 GPa and E= 265.5 GPa) value of 0.15 was observed for specimen nitrided at -700 V whereas it decreased to 0.10 (H= 23 GPa and E= 343.1 GPa) for specimen nitrided at -1100 V. Hence specimens nitrided with -700 V and -900 V demonstrated the best impact energy damping capability therefore resulting in excellent resistance against impact fatigue cracking, even though the nitrided layer thickness was much lower as compared to the specimens treated at -1000 V and -1100 V. It is believed that the impact energy was transferred from nitrided layer to the base metal, thereby leading to an increase in the fatigue crack density (within and beneath the compound layer). Thus impact test

results suggest that -900 V, despite the thinner layer, shows the best combination of high oxidation resistance and high value of the plasticity index H^3/E^2.

In summary, overall surface hardness of the CoCrMo alloy increased significantly due to nitriding at higher bias voltage which directly led to increase in toughness, fracture toughness amd endurance limit of the base metal. No cracks beneath and within the nitrided layer indicates the treatment at -700 V and -900 V samples have high load imoact fatigue limit then the one treated at higher nitriding volatges.

4.6. Tribological Analysis

In this section, analysis of friction and wear mechanisms of the untreated and nitrided specimens are discussed in detail. To understand the wear mechanism such as failure mode, and oxide formation of the untreated specimen, four different sliding distance (0.5, 1.0, 1.5 and 2.0 km) were selected. For nitrided specimens, two different sliding distances (0.5 km and 2.0 km) were selected to explore the failure mode and oxidation behavior of the nitrided layer formed at different nitriding voltage.

4.6.1. Effect of tribo-layer formation on the tribological properties of untreated CoCrMo alloy

Figure 4-19 shows the friction curves of untreated CoCrMo alloys obtained from pin on disc dry sliding tests run at various sliding distances. The wear coefficient (K_C) was calculated using the wear volume measured by the Dektak profilometer.

0.5 km sliding distance:

The friction curve for the sample tested at 0.5 km sliding distance, (figure 4.19a) exhibited two different regions: a run-in period followed by the first steady state region. At the start of the run-in period, the friction coefficient was very low for a short duration due to the presence of an ultra-thin initial oxide layer, which then slowly increased to 0.75 and remained in that range for a while in the first steady state region. This increase in friction coefficient may be attributed to the interaction of the asperity contacts present on the CoCrMo substrate with alumina ball after the removal of the initial oxide layer. Subsequently, the asperity contacts are broken down into fine debris and further fragmented, leading to three body abrasion. The wear coefficient was about $1.1\pm0.35\times10^{-13}$ $m^3N^{-1}m^{-1}$ in this region. The nature of the sliding contact determines the wear regime such as severe and mild. The severe wear observed during the run-

in period and first steady state period was due to the direct alumina-CoCrMo metallic contact made in the absence of an oxide film.

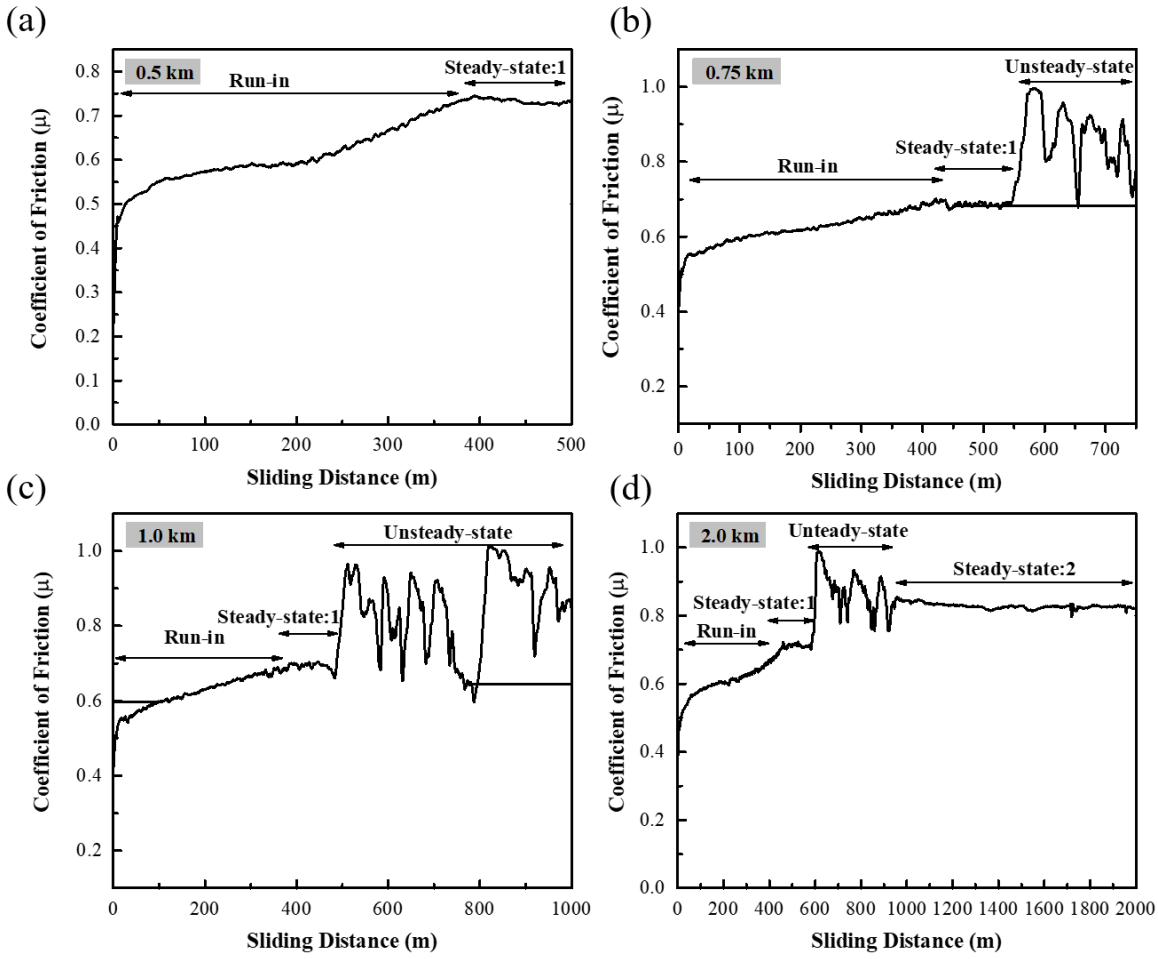

Figure 4-19: Friction curves of CoCrMo alloy with various sliding distances a) 0.5 km, b) 0.75 km, c) 1 km, d) 2 km.

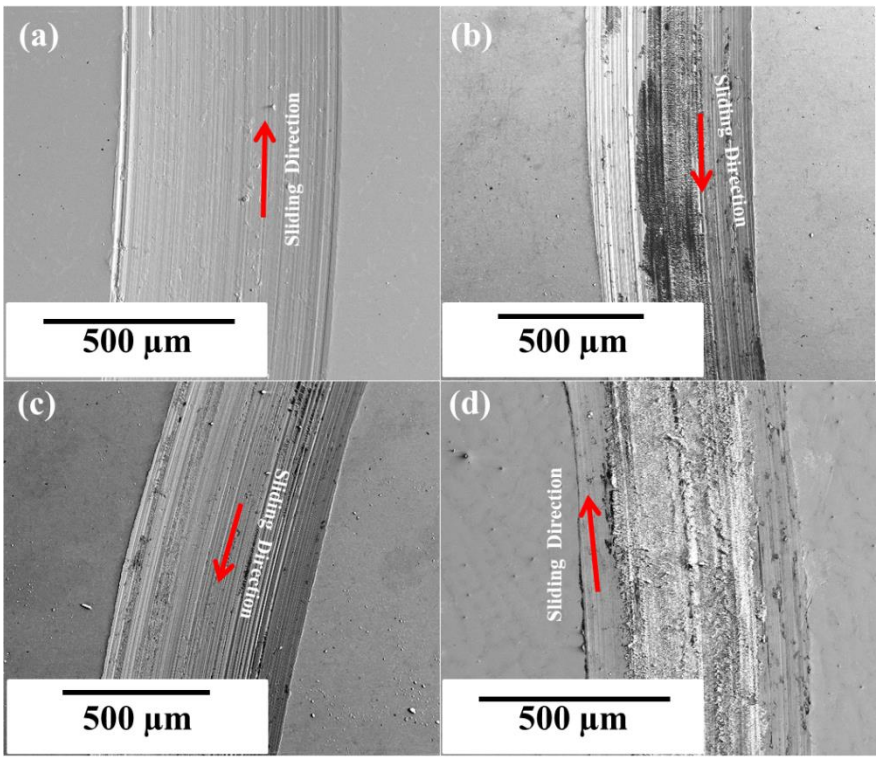

Figure 4-20: Plan view SEM images of worn surfaces of untreated CoCrMo alloy a) 0.5 km, b) 0.75 km, c) 1 km, d) 2 km.

The plan-view SEM micrograph of this sample, figure 4.20a, shows the wide and deep grooves formed due to ploughing, parallel to the sliding direction during abrasive wear (red arrow in the figure indicates the sliding direction). Also, these grooves are found to be filled with pulverized asperity contact wear debris due to their smearing by the stationary counterpart. Generally, the oxidized area looks brighter during SEM observation due to electric charge accumulation as a result of reduced electric conductivity of such a surface. In this sample, the worn area looked little brighter as compared to the unworn area. However, the energy dispersive X-ray (EDX) analysis revealed only the presence of the main alloy elements Co, Cr and Mo but didn't detect any oxide formation in the wear track at this stage.

0.75 km and 1 km sliding distance

The friction curve at the longer sliding distance of 0.75 km (figure 4.19b) showed three distinct regions namely run-in, with continuously increasing friction coefficient; steady state where the coefficient of friction remained almost constant followed by an unsteady state region where huge variations of the friction coefficient were observed. The length of the unsteady state region further increased for the sliding distance of 1 km (figure 4.19c). It is important to highlight that the maximum value of μ in this region was found to be around 1. Generally, the wear debris generated during the run-in period are further compacted into very fine agglomerates while increasing the sliding distance. The volume of the wear debris also increases but more importantly they also intensively oxidize due to the high flash temperatures at the asperity contacts. At the same time, a thin oxide film also grows on the clean worn CoCrMo surface, which is periodically removed, and a fresh clean surface is exposed on each wear traversal. This oxide layer, along with the above said wear debris particles, is then fragmented and compacted onto the worn surface to form slightly raised 'islands'. The area, number and thickness of these islands increases with increasing sliding distance. The complex and repeated interactions between the wear debris, oxide layer and oxide islands with the alumina ball could be the reasons for the unsteady state region with huge fluctuation in friction values. In this region, a transition from a severe to a mild wear regime was observed depending on the extent of the oxide layer formation. The wear coefficient of 0.75 km test was found to be $9\pm0.31\times10^{-14}$ $m^3N^{-1}m^{-1}$ when the worn surface is dominated by non-continuous 'raised islands'. The Kc further decreased to $6.4\pm0.22\times10^{-14}$ $m^3N^{-1}m^{-1}$ when the continuity and compactness of these islands further increased while increasing the sliding distance to 1 km.

Plan-view SEM image (figure 4.20b) of the wear track of 0.75 km sample confirmed that the wear surface was only partially covered with compacted wear debris forming isolated “islands” whereas the remaining surface showed morphology of fine grinding which is typical

for three-body sliding contact wear. Also, figure. 4.20c confirmed the formation of a compacted, non-continuous layer when increasing the sliding distance from 0.75 km to 1 km. The worn surfaces appeared to be relatively rough with distinct dark and bright areas (most likely due to the formation of oxides). The observation of oxygen along with the substrate constituents by EDX analysis confirmed that these worn surfaces were in fact oxidized. Cross-section SEM analysis (figure 4.21a and b) revealed that the thickness of the islands (0.75 km) and the compacted layer (1 km) was 0.3 µm and 0.7 µm, respectively.

2 km sliding distance

In the second steady state region figure. 4.19d, the friction coefficient value dropped considerably to 0.85 immediately after 1 km and continued to slowly drop further with very little variation while increasing the sliding distance to 2 km. The mean µ value was found to be 0.83 and this drop could be attributed to a smooth, near-continuous oxide layer formed as the extent of this layer is further increased in this region. Hence, the CoCrMo substrate made occasional contact with the alumina counterpart, resulting in a very low Kc value of 2±0.17 $\times 10^{-14}$ $m^3N^{-1}m^{-1}$.

The worn surface was found to be much brighter as compared to its counterparts, clearly demonstrating that the surface is heavily oxidized (figure 4.20d). This oxide layer appears to be uniform, compact and near-complete without any interruptions. The EDX analysis also confirmed that this layer is a mixture of oxygen and other substrate elements. The thickness of this layer was about 1.2 µm (figure 4.21c).

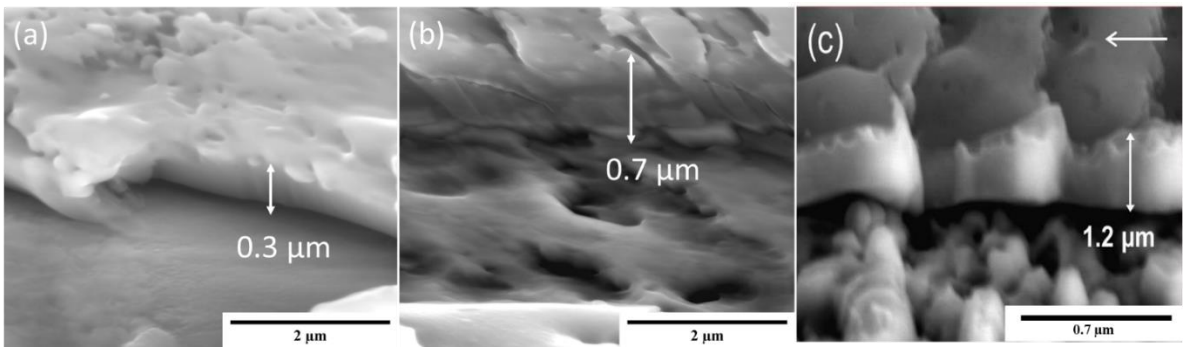

Figure 4-21: Cross-section SEM images showing tribolayers on the worn surfaces of untreated CoCrMo alloy a) 0.75 km, b) 1 km, c) 2 km.

In summary, the friction coefficient value increased sharply after 0.5 km and remained high for a while, which then considerably decreased as the sliding progressed. The friction behaviour and the coefficient of friction values in the above explained individual regions remained almost unchanged for all the four sliding distances. All four curves showed an almost identical run-in period of about 400 m length followed by the first steady state region of about 100 m length. Usually, the friction coefficient tends to be lower in the mild wear regime than that observed in the severe wear regime. However, it has been reported that the oxide layers do not always reduce the friction coefficient [31]. In this study, the friction coefficient in the mild wear regime is found to be higher than that in severe wear. Nevertheless, the growth of the oxide layer decelerated the wear of untreated CoCrMo alloy. The characteristic dry sliding wear mechanisms involving adhesion, abrasion, severe plastic deformation along with oxide tribolayer formation determined the wear behaviour of the CoCrMo alloy at the various stages of sliding test.

4.6.2. **Dry sliding wear and friction mechanism of nitrided CoCr alloys:**

Figure 22 shows the friction coefficient curves of CoCrMo alloy nitride at various bias voltages after sliding for 0.5 km and 2 km respectively. Table 4.3 lists the thickness, microhardness, average coefficient of friction (µ) and coefficient of wear values (Kc) of all samples for both sliding distances. As expected, the µ and Kc values decreased while increasing

the sliding distance from 0.5 km to 2 km. However, these values from 2 km tests were considered for the discussion since the effect of the oxide tribo layer is more pronounced at such a long sliding distance. The wear behaviour of nitrided metallic alloys depends on the type (compound and/or diffusion), hardness and thickness of the nitrided layers along with the characteristics of the tribo layer. It is expected that a hard and thick nitrided layer along with a well-adhered smooth top oxide layer would exhibit better wear performance during sliding. In the case of nitrided stainless steel alloys, it has been reported that the diffusion zone is solely responsible for the wear resistance, fatigue strength and the load bearing capacity of steel components in the absence of a compound layer [32].

Table 4-3

Nitrided layer thickness, microhardness, coefficient of friction (μ) and wear coefficient (Kc) of the untreated and nitrided specimens.

Sample	Thickness μm	Microhardness HK	Friction Coefficient (μ)		Wear Coefficient (Kc) $m^3N^{-1}m^{-1}$	
			0.5 km	2 km	0.5 km	2 km
Untreated			0.76±0.008	0.8±0.01	0.5 $\times10^{-15}$	2 km$\times10^{-15}$
-700V	1	1400	0.72±0.01	0.61±0.01	4.2±0.15	2.18±0.09
-900V	1.8	2230	0.65±0.004	0.62±0.01	1.98±0.06	1.11±0.35
-1000V	3.3	2180	0.60±0.005	0.58±0.005	7.38±0.31	4.02±0.09
-1100V	3.7	2750	0.65±0.01	0.59±0.005	8.58±0.2	4.42±0.19

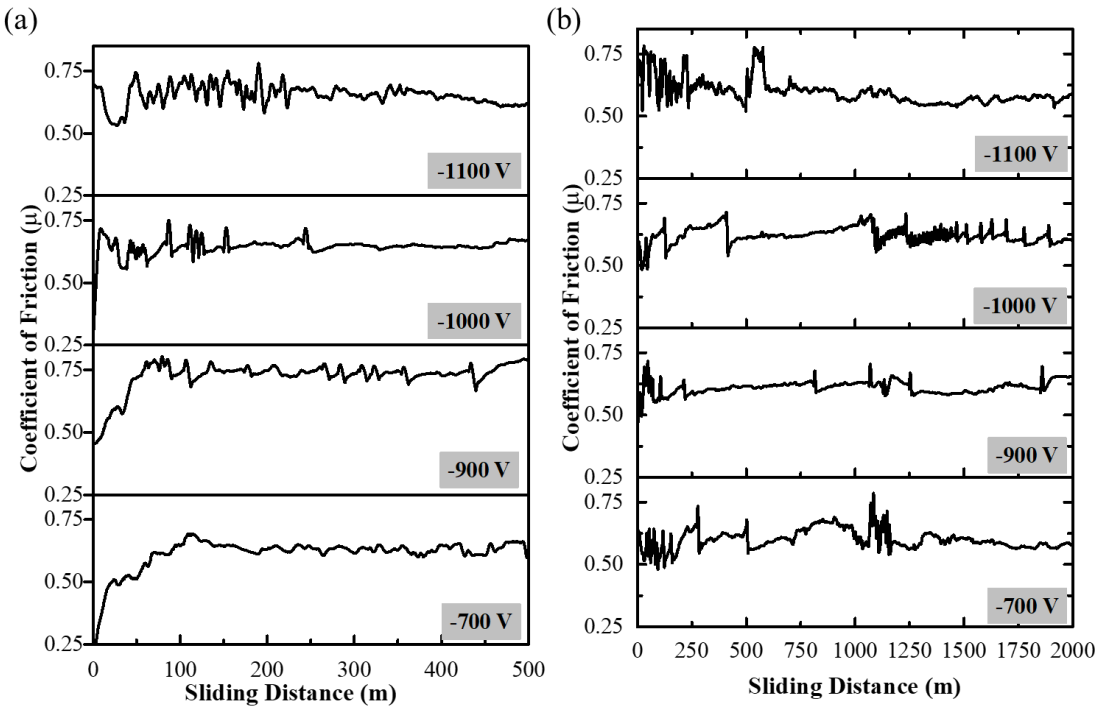

Figure 4-22: Coefficient of friction curves of various nitrided alloys a) 0.5 km b) 2 km.

As anticipated, all nitrided samples showed increased wear resistance due to increased hardness as compared to untreated CoCrMo alloy. In all the cases, the wear debris generated from the nitrided case participated in the wear process rather than that of inert alumina counterpart as it did not undergo severe wear [Refer Sec. 4.6.3]. The lateral crack observed at the nitrided layer/CoCrMo substrate interface in -700 V sample, (figure 4.23a) could be attributed to the fatigue failure at the interface due to tensile stresses developed in the CoCrMo base material during the sliding test since this is the thinnest nitride layer among the four samples of about 1 μm, including a very thin diffusion layer. The micro hardness of this sample was also found to be very low, in the range of 1400 HK. This sample exhibited the μ and Kc values of 0.61±0.01 and $2.18\pm0.09\times10^{-15}$ $m^3N^{-1}m^{-1}$, respectively. Despite showing few typical surfaces and/or subsurface cracks, the sample nitrided at -900 V exhibited the lowest Kc of about $1.11\pm0.35\times10^{-15}$ $m^3N^{-1}m^{-1}$ with μ of 0.62±0.01. The microhardness, 2230 HK, of this sample is much higher than that of -700 V sample. Thus, the smooth oxide tribolayer formed

on the worn surface is well supported by the underlying 1.8 µm thick hard nitrided layer. It is important to reiterate that this sample generated more nanoscale debris during the asperity contact at the beginning of the wear process due to smooth surface morphology rather than large scale wear debris particles which facilitate severe wear. Hence, in this case, it can be argued that the oxidative mild wear appears to be the dominating wear mechanism rather than micro abrasion. Also, this sample showed a distinct bright, relatively thick diffusion layer beneath the compound layer and clearly enhanced ductility as discussed in section 4.6.2.1. The enhanced ductility of the nitride zone in this case provides for the increased load bearing capacity of such material. Therefore, the synergy between the oxidative mild wear and the enhanced load bearing capacity of the nitrided layer is seen as a main reason for the low Kc value determined for this case.

It is well understood that using higher nitriding voltages such as -1000 V and -1100 V results in the formation of a thicker nitrided layer with increased hardness along with increased residual stress. The increase in the hardness could also be attributed to the formation of Cr_2N compounds (observed by XRD, see section 4.1) at such high voltages. The thickness of the nitrided case was found to be 3.3 µm for bias voltage of -1000 V and 3.7 µm for bias voltage of -1100 V. The -1100 V sample showed the highest hardness value of 2750 HK. However, the microhardness value observed for HIPN-1000V sample, 2180 HK was found to be slightly lower than that of -900 V sample. These samples showed a similar coefficient of friction µ value of about 0.59±0.005. The wear coefficient of -1000 V and -1100 V samples was found to be $4.02\pm0.09\times10^{-15}$ $m^3N^{-1}m^{-1}$ and $4.42\pm0.19\times10^{-15}$ $m^3N^{-1}m^{-1}$, respectively, which represents a nearly four-fold increase as compared to the -900 V sample. As explained in Raman and XRD (section 4.6.3), these coatings produced large scale wear debris particles at the beginning of the wear process as they are very rough, brittle and fragile due to increased hardness and residual stress. These large-scale wear particles further aggravated the wear loss as the sliding

progressed. Even though the -1000 V and -1100 V samples showed almost a factor of two thicker nitrided case compared to -900 V sample, the wear behaviour was dominated by the combined effect of higher surface roughness, hardness and residual stress levels which lead to poor wear resistance due to the operation of a severe three body micro abrasion wear mechanism rather than oxidative wear despite the formation of oxide tribolayer during sliding.

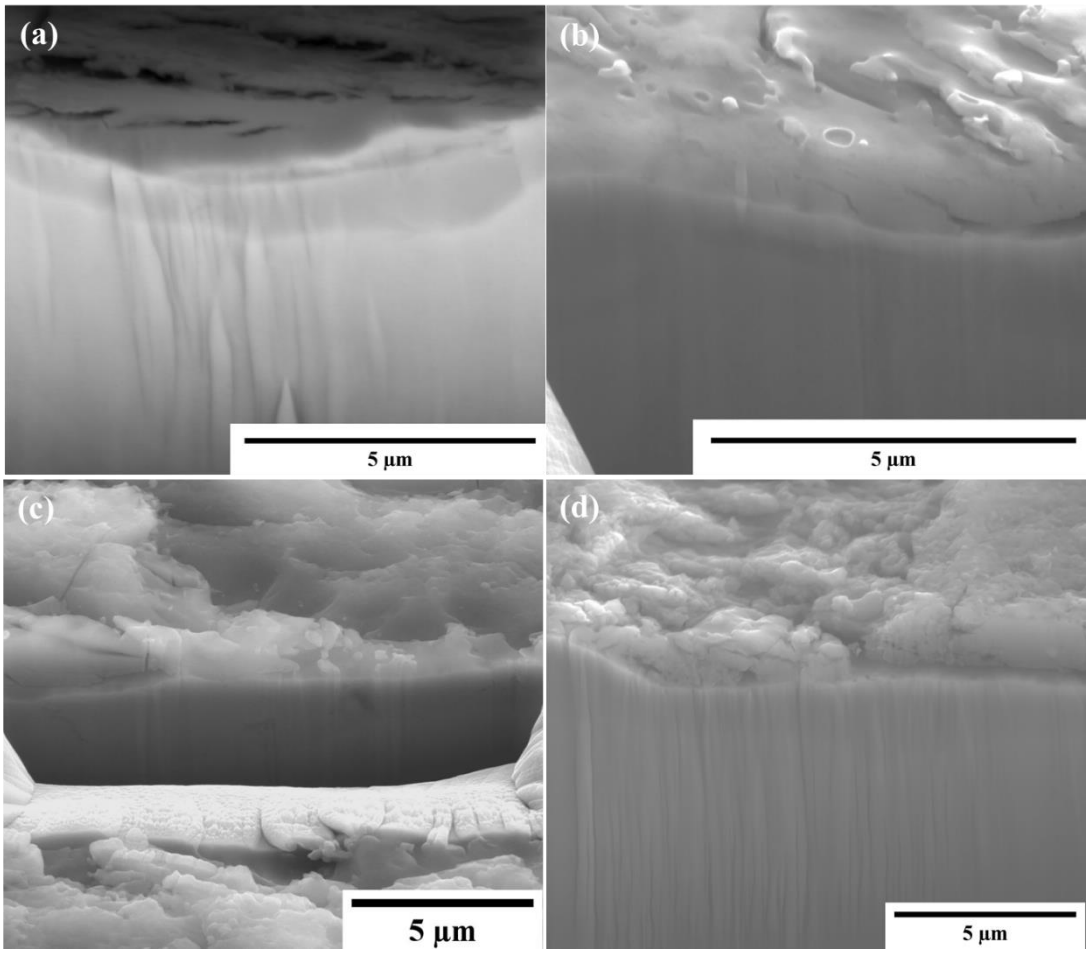

Figure 4-23: FIB cross-section SEM images showing tribolayers formed on the worn surfaces of CoCrMo alloy (sliding distance: 2 km) nitrided at various bias voltages a) -700 V, b) -900 V, c) -1000 V, d) -1100 V.

4.6.2.1. Surface morphology of wear track:

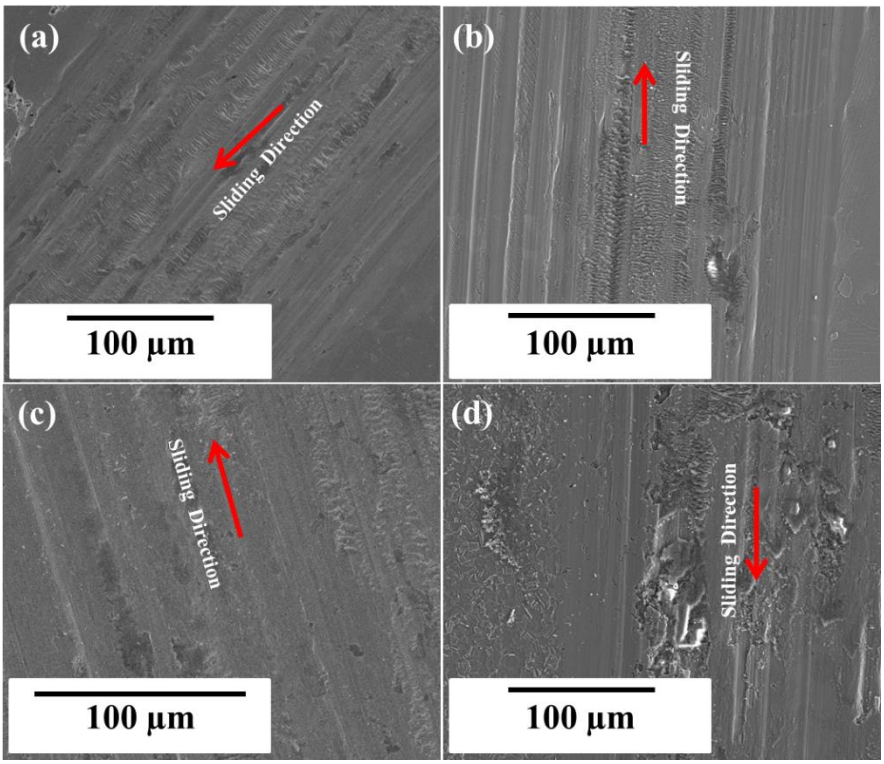

Figure 4-24: Plan view SEM images showing worn surfaces of CoCrMo alloy (sliding distance: 0.5 km) nitrided at various bias voltages a) -700 V, b) -900 V, c) -1000 V, d) -1100 V.

The wear scars generated during these tests were analysed using scanning electron microscopy. The plan view SEM images of the wear tracks of all nitrided samples after sliding for 0.5 km are shown in figure 4.24. As explained in Section 4.6.1, during the initial stages of the tribo-test, the asperities on the surface are ground out and the wear debris oxidized under favourable conditions after the removal of the initial air-formed film. Subsequently, a tribolayer is formed due to the adherence of wear particles to the parent worn surface through the process explained in section 4.6.1. When imaged using SEM, the surface also exhibited dark and bright areas (electric charge due to oxygen). The wear scars of the samples treated with -700 V and -900 V showed a relatively smooth surface, characterised with shallow grooves and very fine micro cracks, which is typical for fine polishing. This wear behaviour could be due to the initial smooth surface morphology of these samples with roughness (Ra) values of about 71 nm and 65 nm when nitrided at bias voltages of -700 V and -900 respectively. In this case, it can be

argued that due to the small size of the wear debris, they do not inflict severe damage by micro-cutting but are mostly compacted onto the worn surface of the parent material in the tribocontact to form very thin layers. Therefore, it is believed that the predominant wear mechanism in this case is two-body rather than three-body even though the wear debris are still generated. In contrast, the deformation grooves found in the wear tracks on the other two samples nitrided at higher bias voltage of -1000 V and -1100 V were wider and deeper when compared to -700 V and -900 V samples. This difference is attributed to the higher initial surface roughness obtained when higher nitriding bias voltages are applied. The increased roughness in these conditions results from the more intensive bombardment of the nitrided surface by highly energetic N/H and metal ions which produce a significant surface sputtering effect. The roughness is further influenced by the lattice volume expansion due to the incorporation of nitrogen into the metallic lattice during the nitriding process. It was found that the sample nitrided at - 1000 V with a relatively higher roughness value of Ra = 82 nm showed moderate damage, and no formation of any largescale wear debris was observed for this case. However, further increase of the surface roughness to Ra = 124 nm due to the application of higher nitriding bias voltage of -1100 V, resulted in severe wear damage due to the operation of three body contact abrasive wear mechanism, figure 4.24d. The wear scar in this case was very rough with debris of different shapes as reported by Li et al. [33].

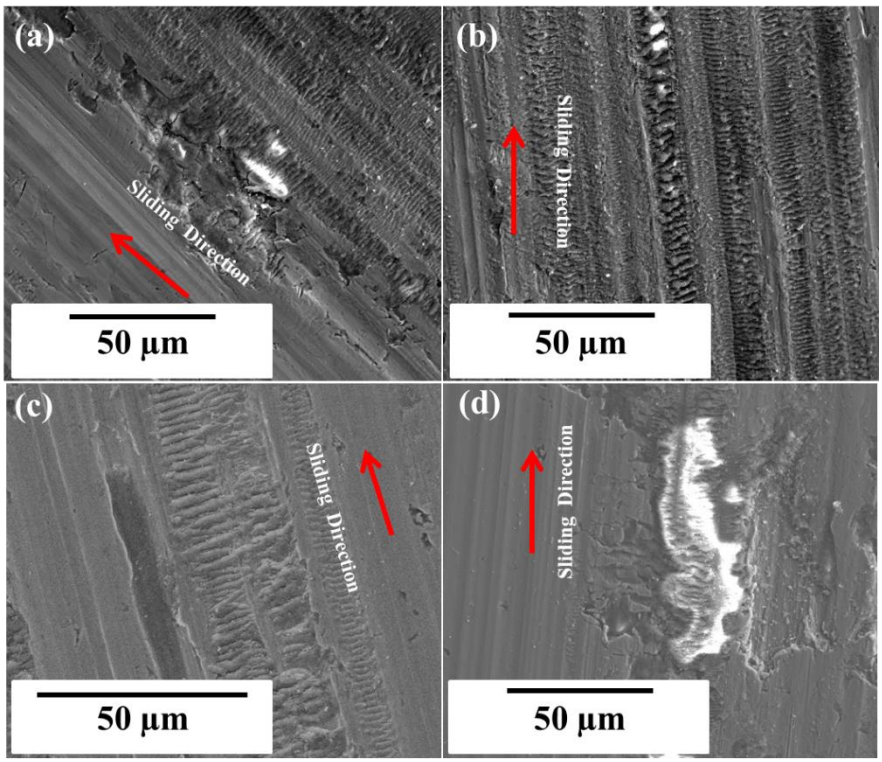

Figure 4-25: Plan view SEM images showing worn surfaces of CoCrMo alloy (sliding distance: 2 km) nitrided at various bias voltages a) -700 V, b) -900 V, c) -1000 V, d) -1100 V.

Figure 4.25 summarises the SEM images of the worn surfaces of all nitrided samples after sliding for 2 km. As expected, the extent of the wear damage and oxidation has increased with increasing sliding distance for all four samples. Low magnification images in figure 4.26 also show the surface morphology over a large area of the worn surface.

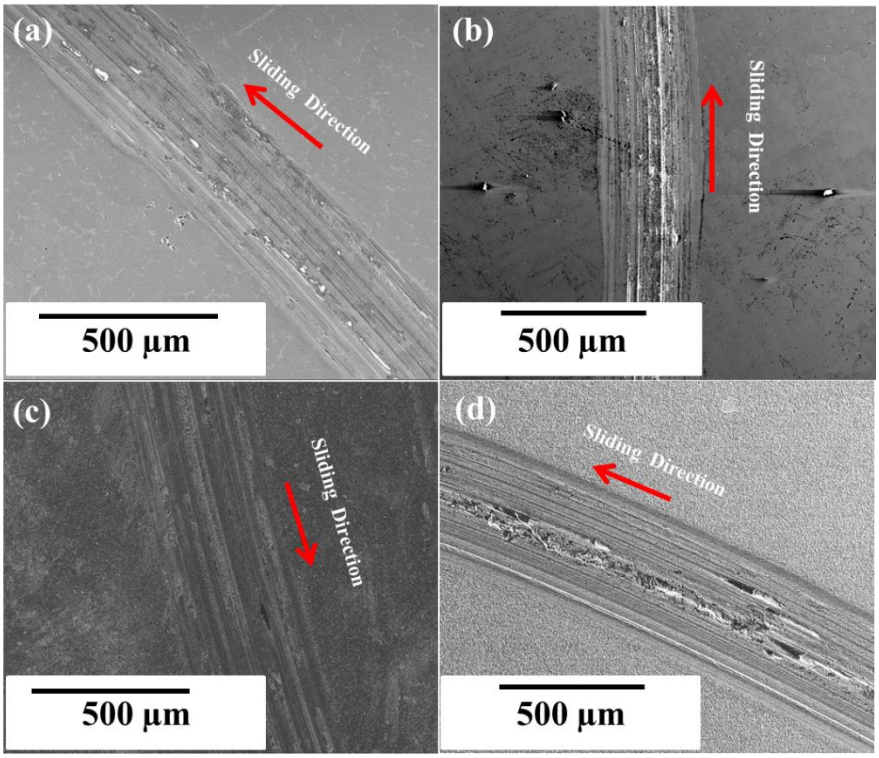

Figure 4-26: Low magnification plan view SEM images showing worn surfaces of CoCrMo alloy (sliding distance: 2 km) nitrided at various bias voltages a) -700 V, b) -900 V, c) -1000 V, d) -1100 V.

4.6.2.2. Sub-surface analysis of worn surface:

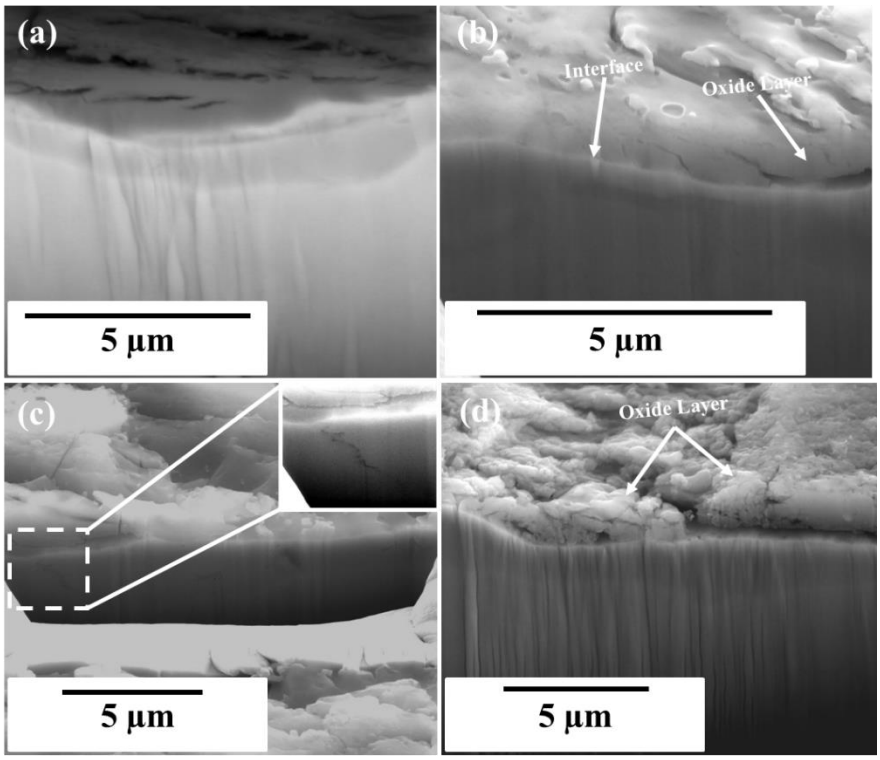

Figure 4-27: FIB cross-section SEM images showing tribolayers formed on the worn surfaces of CoCrMo alloy (sliding distance: 2 km) nitrided at various bias voltages a) -700 V, b) -900 V, c) -1000 V, d) -1100 V.

The subsurface structure of all nitrided samples after sliding for 2 km was investigated using a Focused Ion Beam milling (FIB) enabled Scanning Electron Microscope. The distinct tribolayers formed on the worn surface of all nitrided samples can be clearly seen in figure 4.27. The tribolayer formed on -700 V sample is comprised of semi-compacted, coarse, small scale wear debris particles generated during dry sliding (figure 4.27a). On the contrary, the tribolayer formed on -900 V sample appears to be fully compacted, relatively smooth without any coarse wear debris particles (fig. 27b). The -1000 V and -1100 V samples showed a tribolayer with an extremely rough surface which consisted of largescale wear debris particles [figure 4.27 (c & d)].

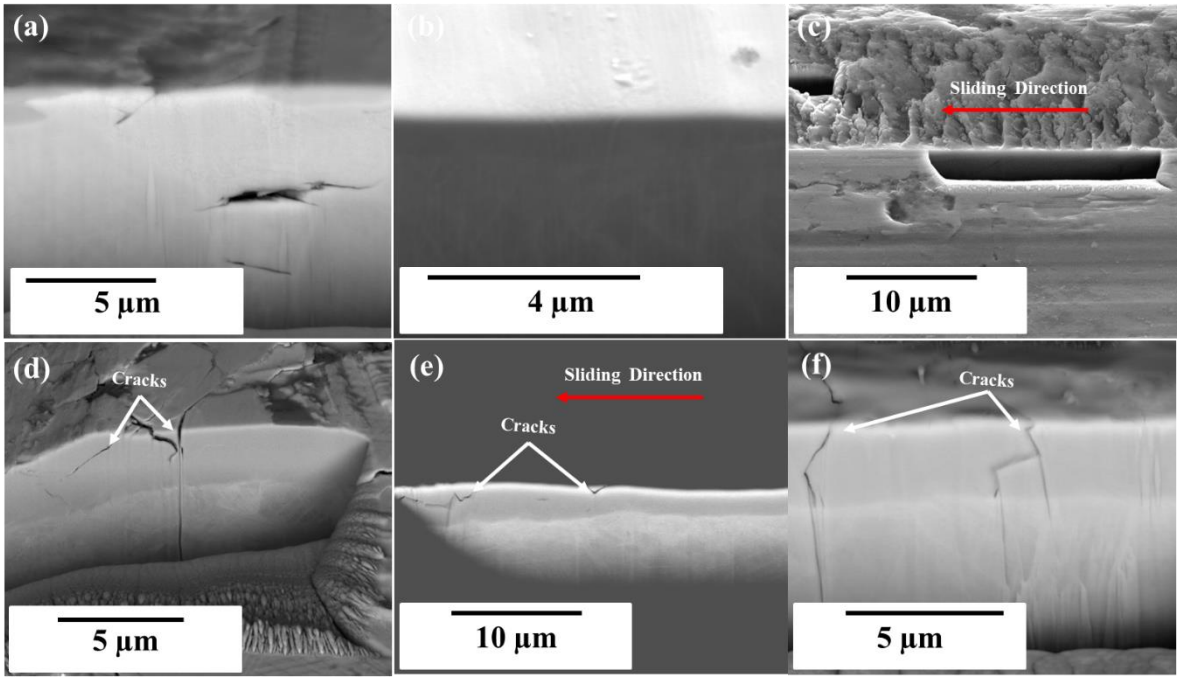

Figure 4-28: FIB cross-section SEM images showing surface and subsurface morphology of worn areas of CoCrMo alloy (sliding distance: 2 km) nitrided at various bias voltages a) -700 V, b) -900 V, c)-900 V (longitudinal), d) -1000 V, e) -1100 V, f) -1100 V (longitudinal).

Figure 4.28a shows a micro crack initiated on the worn surface of the sample (where the tribolayer appears to be thin) nitrided at -700 V and its propagation towards the soft CoCr substrate. A micro void parallel to the surface can also be seen formed close to the nitrided case-substrate interface. In contrast, no surface initiated, or subsurface micro cracks were found in this particular worn area for the -900 V sample (figure 4.28b). A thorough investigation of

the entire wear track by longitudinal FIB cross sectioning discovered only a small subsurface crack parallel to the sliding direction, formed due to the shear deformation of the nitrided layer (figure 4.28c). In comparison with the nitriding at bias voltage of -700 V, the nitriding at higher bias voltage of -900 V has produced a layer with clearly enhanced ductility. However, the nitrided layer ductility deteriorated when the nitriding voltage was further increased. FIB cross sections of the wear track produced in both directions (longitudinal and perpendicular) to the sliding showed that the samples produced at nitriding voltage of -1000 V and higher were severely damaged with micrographs showing an increased number of surface cracks [figure 4.28 (d & e)] and cracks propagating through the entire nitride layer towards the substrate (figure 4.28f].

4.6.3. **Chemical and Phase analysis of oxide layer formed on worn surfaces:**

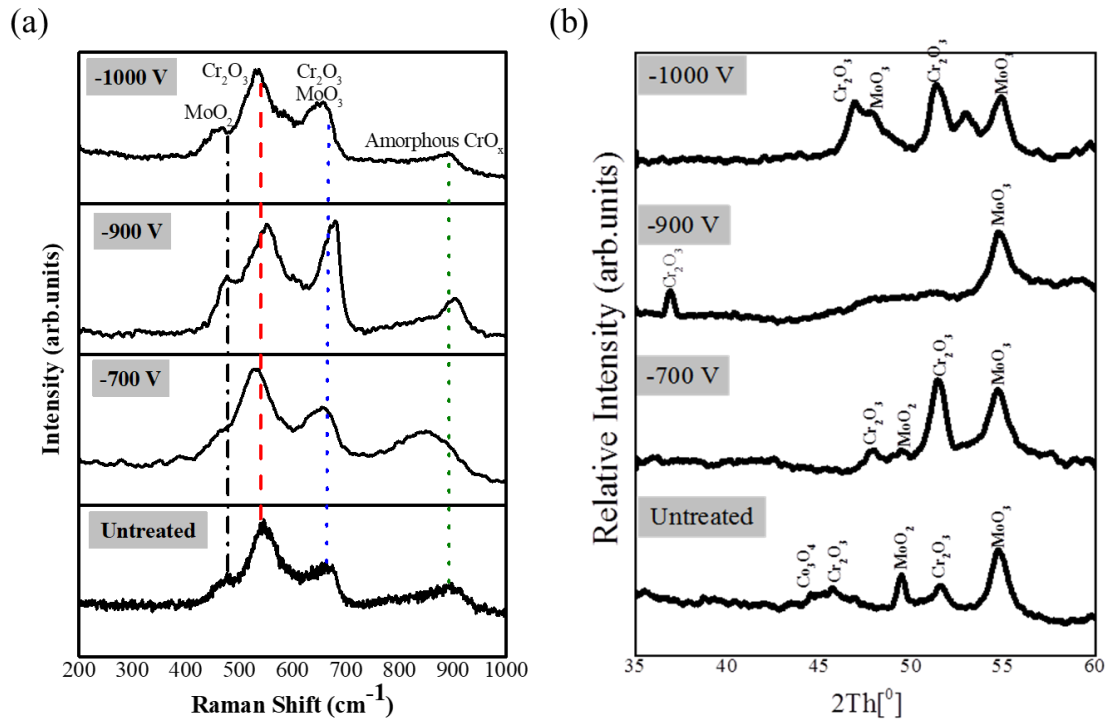

Figure 4-29: (a) Raman spectra (b) X-ray diffraction spectra of worn surfaces of the untreated and various nitrided specimens. Note: The Raman and XRD spectra of -1100 V was found similar to that of -1000 V.

X-ray diffraction and Raman analysis were used to investigate the phase composition of the wear debris formed on the worn surfaces of the untreated CoCrMo substrate and nitrided

samples after sliding for 2 km. The Raman spectra of the worn surfaces are shown in figure 29a. All the samples showed Raman peaks originating from chromium and molybdenum-based oxide compounds, however, with slight shift in their positions. Table 4.4 lists the assignment of various Raman peaks to such oxide compounds. Raman peaks originating from MoO_2 were observed in the 455 cm^{-1} – 480 cm^{-1} regions. The characteristic Raman peak of Cr_2O_3 was observed in the range of 532 cm^{-1} to 551 cm^{-1} [34][35][36][37]. The peak observed between 650 cm^{-1} and 680 cm^{-1} could be originating from Cr_2O_3 and/or MoO_3 [38][39]. Also, a peak observed between 800 cm^{-1} and 900 cm^{-1} was assigned to various chromium based oxides such as CrO_2, CrO_3 and Cr_8O_{21} as they overlap each other [40][41][42][43].

Table 4-4
Assignment of various Raman peaks to respective oxide compounds formed on the worn surfaces of untreated and nitrided alloys (sliding distance: 2 km).

Sample	Raman shift (cm^{-1})	Peak assignment
Untreated	457	MoO_2
	532	Cr_2O_3
	652	Cr_2O_3 and/or MoO_3
	800- 900	Cr based oxides
HIPN-700V	475	MoO_2
	544	Cr_2O_3
	679	Cr_2O_3 and/or MoO_3
	800- 900	Cr based oxides
HIPN-900V	463	MoO_2
	534	Cr_2O_3
	657	Cr_2O_3 and/or MoO_3
	800- 900	Cr based oxides
HIPN-1000V	475	MoO_2
	551	Cr_2O_3
	667	Cr_2O_3 and/or MoO_3
	800- 900	Cr based oxides

Figure 4.29b shows the XRD patterns of worn surfaces after sliding for 2 km. Table 4.5 shows peak positions and their assignment to respective oxides. Diffraction peaks due to the formation of Cr and Mo based oxide compounds were observed for all the samples including

untreated CoCrMo substrate. However, the diffraction patterns of nitrided samples showed significant differences between them in the peak number, peak position and the composition of oxide compounds formed on the worn surfaces. These differences could be mainly due to the degree of oxidation and the nature of the oxide compounds formed on the selected area of interest for the XRD measurement as only a fraction of the worn surface was analysed. The XRD pattern of the untreated CoCrMo substrate also revealed the formation of a Co (major substrate constituent) based oxide compound. These results, along with Raman analysis confirmed that the tribolayers formed on the worn surfaces are indeed oxidized compounds of CoCrMo alloy [44][45][46][47]. Also, it is important to that note that both Raman and XRD analyses did not detect alumina on the worn surfaces of the nitrided specimens. Hence it can be argued that the wear of inert alumina counterpart is marginal.

Table 4-5

Assignment of various XRD peaks to respective oxide compounds formed on the worn surfaces of untreated and nitrided alloys (sliding distance: 2 km).

Sample	Peak Position	Peak assignment
Untreated CoCrMo substrate	44.2°	Co_3O_4
	45.7°	Cr_2O_3
	48.3°	MoO_3
	52.7°	Cr_2O_3
	54.7°	MoO_3
HIPN-700V	47.4°	Cr_2O_3
	48.6°	MoO_3
	49.9°	MoO_3
	52.7°	Cr_2O_3
HIPN-900V	36.2°	Cr_2O_3
	55.2°	MoO3
HIPN-1000V	45.9°	Cr_2O_3
	46.7°	MoO3
	52.5°	Cr_2O_3
	55.2°	MoO3

In summary, all the nitrided samples exhibited enhanced wear resistance as compared to the untreated CoCrMo alloy. Among the three nitrided samples, the sample nitrided at -900 V was identified as the best with the lowest wear coefficient of $K_C = 1.11 \times 10^{-15}$ m^3 N^{-1} m^{-1} , thickness of 1.8 μm and Knoop microhardness of 2230 HK0.010. The wear resistance and the load bearing capacity of the nitrided layers are strongly influenced by its microhardness and ductility. In this case, the oxidative mild wear mechanism was identified as the dominant wear mechanism. The FIB-SEM analysis of the worn area of this sample showed near scratch-free surface and subsurface layers, indicating the enhanced ductility. The synergy of enhanced hardness, oxidative mild wear and ductility resulted in increased load bearing capacity which in turn enhanced the wear behavior.

4.7. Corrosion Study:

4.7.1. Electrochemical Analysis in 3.5 wt.% NaCl:

Figure 4.30a displays the evolution of OCP as a function of time. All the nitrided specimens exhibited a rapid increase in the potential values before reaching near-steady state values. The untreated CoCrMo alloy had the lowest rate of increase, which suggested a gradual passivation of the surface. The specimen nitrided at -900 V had the best OCP value followed by specimen nitrided at -700 V and -1000 V. Barring the -1100 V specimen, which exhibited a gradual drop in the curve after attaining a peak (around 750 seconds of recording), all the nitrided specimens performed better as compared to the untreated alloy. Smooth, unfluctuating, and continuous nature of the OCP curves suggests that the nitrided layers were homogenous, defect free and continuous in structure indicating a superior quality.

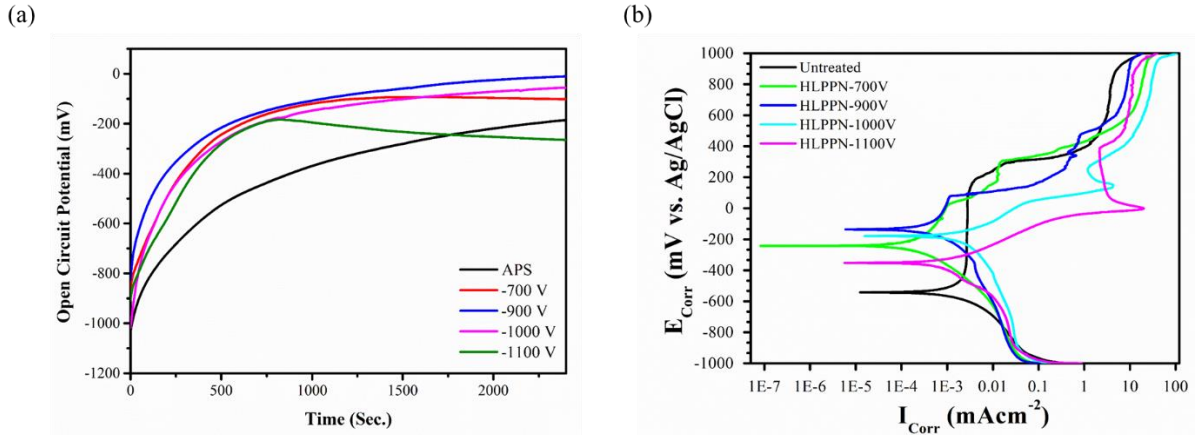

Figure 4-30: (a) Open circuit potential (OCP) and (b) Potentiodynamic polarisation curves of the untreated specimen and specimens nitrided at various bias voltage (-700 V to -1100 V) submerged in 3.5 wt.% NaCl solution.

The potentiodynamic polarisation curves of the untreated and nitrided specimens are shown in figure 30b. Corrosion current densities (I_{Corr}, $mAcm^{-2}$), corrosion potentials (E_{Corr}, mV) were extracted from the polarisation curves using standard Tafel analysis (using the Sequencer software-ACM instruments) and values are presented in Table 4.6. As evident, all the specimens showed a clear difference in terms of E_{Corr} values, anodic dissolution, passivation

and transpassivation domains and the significance of nitriding voltage and consequential microstructure in determining them was enormous. Amongst these, the shift in E_{Corr} values was noticeable. It is evident that, irrespective of the nitriding voltage, the improvement in corrosion resistance of the base CoCrMo alloy was significant. In comparison, the untreated CoCrMo alloy exhibited a clear and a stable passivation domain in the potential ranges of -380 mV to +100 mV. This passive behaviour has been attributed to the formation of Cr based oxides films (mainly to the formation of $Cr_2O_3/Cr(OH)_3$))formed in air which are difficult to remove [48][49]. Beyond +200 mV formation of Cr (VI) species in the passive layers, increasing fraction of CoO and Mo, dissolution of Co at higher anodic potentials, significant increase in the passive layer thickness and dissolution of these passive films along with the water oxidation reactions led to the rapid rise in the current values [34][37][48][52]. Despite a limited but a clear and stable passive domain, the bare alloy exhibited higher anodic currents and had the lowest E_{Corr} value (-527 mV) among the samples analysed thus implying a poor corrosion resistance.

Table 4-6

Corrosion analysis data obtained from the polarisation curves of the nitrided specimens and the untreated specimen when analysed against 3.5 wt% NaCl.

Electrolyte	**3.5 wt.% NaCl**					
Repetition	**SET-1**			**SET-2**		
Sample ID	**E_{Corr} (mV)**	**I_{Corr} ($mAcm^{-2}$)**	**OCP (mV)**	**E_{Corr} (mV)**	**I_{Corr} ($mAcm^{-2}$)**	**OCP (mV)**
Untreated	-591	$8.50E^{-5}$	-186	-601	$8.68E^{-06}$	-189
-700 V	-126	$1.35E^{-4}$	-13	-167	$1.51E^{-05}$	-31
-900 V	-133	$6.06E^{-5}$	-96	-179	$4.71E^{-05}$	-57
-1000 V	-158	$9.19E^{-5}$	-154	-177	$2.60E^{-04}$	-172
-1100 V	-351	$2.21E^{-4}$	-258	-335	$1.11E^{-04}$	-260

The sample nitrided with -900 V showed a significant upward shift to exhibit the best E_{Corr} value (-126 mV). The corrosion kinetics of this sample could be described as follows. After a brief passivation in the -150 mV to 60 mV polarisation interval, the polarisation curve indicated a high dissolution rate in the 60 mV to 260 mV interval, followed by the tendency of re-passivation in the potential range of around +250 mV to +460 mV. The microstructure of this specimen, figure 4-4c, predominately consisted of a distinct, uniform S phase band at the interface of the base alloy and a compound layer consisting of both $M_{2\text{-}3}N$ and M_4N (where M is mostly Co dominated). Several reports on nitriding of CoCrMo or Fe based alloys in the literature have attributed the improvement of corrosion resistance to the presence of the S phase structure [10][53][54]. On the other hand, structures dominated by Co based compounds have shown a poor corrosion performance due to the ready dissolution of the Co from these compounds [52]. Thus, consistent with the literature, the corrosion behaviour of the -900 V nitrided specimen seemed to be a weighted mixture of the corrosion performances of the two microstructures: namely the S phase and the Co based compounds. Improvement in the ECorr value and lower corrosion currents in the anodic ranges unto +60 mV could be attributed to the presence of a distinct but a homogenous S phase diffusion layer. The smaller repassivation attempt of the specimen above +250 mV (potentials between +250 mV and +460 mV) could be attributed to the passivation of Cr (either from the base alloy or dispersed Cr present in the nitrided layer). Beyond potentials of around + 460 mV, the polarisation curve was dominated by the dissolution of both Co and Cr [50]. The specimen nitrided at -700 V nearly mimicked the corrosion performance of the -900 V, except for a slight drop in the E_{Corr} value (-230 mV) and the repassivation potentials (a drop in value from +250 mV to around +180 mV). The microstructure of this specimen, figure 4.3a, essentially, also resembled to -900 V, albeit a thinner compound layer and a slimmer diffusion band consisting of the S phase structure. Thus, the reduction in E_{Corr} value of -700 mV sample was consistent with the microstructural changes.

In the case of -1000V and -1100 V specimens, figure 4-4 (d-e), the microstructures were made up of relatively thicker compound layers which consisted of a mixture of both $M_{2-3}N$ and M_4N compounds and were also estimated to have a thin S phase diffusion band at the interface between nitrided layer and the base alloy. XRD results (figure 4.3(e)) also showed peaks pertaining to precipitation of CrN (-1000 V) and Cr_2N (-1100 V) phases as a result of temperature rise leading to a localised heating (for e.g., temperatures reached 520 °C in the case of nitriding with -1100 V) due to the intense bombardment of the ions. Despite having thicker compound layers, the corrosion performance of -1000 V and -1100 V specimens, in general, was inferior compared to -700 V and -900 V specimens. The E_{Corr} value of -1000 V specimen (-158.17 mV) and -1100 (-351.33 mV) was lower to -700 V (-126.28 mV) and -900 V (-133.39 mV) specimens, but higher than the untreated base alloy (-590.63 mV). The anodic domains of these were identical as far the shape is concerned and showed a high dissolution (one of the highest I_{Corr} values in this study), with no tendency to passivate until potentials of around +140 mV for -1000 V specimen and around +20 mV for -1100 V specimen. The clear difference in performance between the -1100 V specimen and other specimens is the observation of a broader passive domain, albeit higher corrosion currents, between potentials +20 mV and +370 mV and could be attributed to the limited passivation, in this case, offered by the thinner S phase layers and to some extent by the Cr precipitates [50][55]. The disadvantages of Cr precipitates in the nitrided microstructure was consistent with those reported earlier [56][52].

Thus, in this study, when analysed against 3.5 % NaCl, the corrosion performance of the nitrided specimens showed a strong dependency on the microstructure. A clear passivating behaviour of the untreated CoCrMo alloy (because of the readily available Cr from the metal matrix composite) was lost to the nitriding process. However, this loss appeared to be compensated by the S phase structure and the metal nitrides (mostly Co) obtained by nitriding;

evident in terms of higher E_{Corr} values and lower I_{Corr} values in most anodic domains for -700 V and -900 V nitrided specimens.

4.7.2. **Electrochemical Analysis in Hank's solution:**

CoCrMo alloy has been widely used in medical implant applications such as hip replacement. The body environment is considered to be very complex and contains various salts, amino acids, lipids and proteins [57]. Once the implant submerges in the body fluids such as saliva and buffer solution, the behaviour of the material changes exceedingly changes due to corrosion process [58][59][60]. Hence, analysis of the untreated and nitrided specimens for its corrosion behaviour in simulated body fluid (SBF) was deemed essential. In this study, Hank's solution was chosen as the SBF and the composition of Hank's solution is presented in table 4.7.

Table 4-7

Composition of Simulated body fluid (Hank's Solution).

Inorganic Salts	**Concentration (mg/L)**	**Amino Acids**	**Concentration (mg/L)**
$CaCl_2$-$2H_2O$	185	L-Arginine hydrochloride	126
$MgCl_2$-$6H_2O$	100	L-Cystine	21
$MgSO_4$-$7H_2O$	100	L-Glutamine	292
KCl	400	L-Histidine hydrochloride-H_2O	42
KH_2PO_4	60	L-Isoleucine	52
$NaHCO_3$	350	L-Leucine	52

NaCl	8000	L-Lysine hydrochloride	73
Na_2HPO_4	48	L-Methionine	15
Glucose-D	1000	L-Phenylalanine	32
		L-Threonine	48
		L-Tryptophan	10
		L-Tyrosine	36

Figure 4.31a shows the OCP curves recorded as a function of time. Similar to the NaCl results, all the nitrided specimens exhibited a rapid increase in the potential values with time before reaching near-steady state values. However, in the case of the untreated alloy, the potential rose gradually to a near-steady state suggesting that passive layer formation was less effective in retarding the corrosion currents as compared to the nitrided specimens. A clear hierarchy in the OCP values was observed where the specimen nitrided at -900 V had the noblest OCP value followed by those nitrided at -700 V, -1000 V and -1100 V respectively. Table 4.8 provides the corrosion parameters such as I_{Corr} (corrosion current density, mAcm-2), E_{Corr} (corrosion potential, mV) deduced from these polarisation curves.

Figure 31b shows the polarisation curves recorded for the specimens when tested against Hank's solution. In the case of the untreated alloy, similar to the performance against 3.5% NaCl solution, a stable passive domain was observed until potentials of around +150 mV. However, the E_{Corr} value was found to be significantly lower, at around -789 mV, which suggested an inferior corrosion performance as compared to against 3.5% NaCl solution.

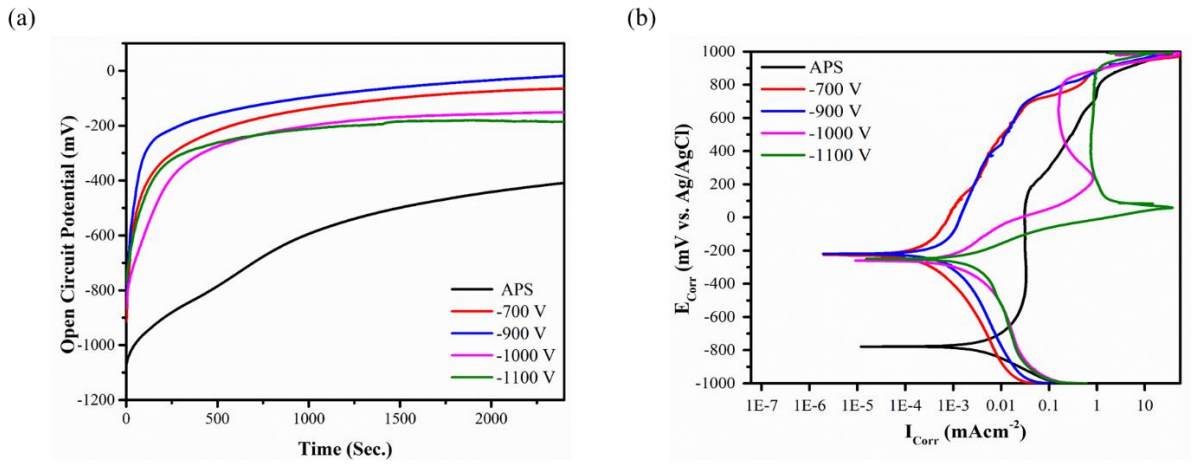

Figure 4-31: (a) Open circuit potential curve and (b) Potentiodynamic polarisation curves of the untreated specimen and specimens nitrided at various bias voltage (-700 V to -1100 V) in Hank's solution.

Dissolution of CoCrMo alloy has been considered sensitive to a number of factors such as the type of BSF, it's pH value, protein build-up, oxidation reactions and consequent changes in electrochemical potentials [50][58][61]. Literature suggests that, on immersion in Hank's solution, Co from the alloy readily undergoes dissolution by the outward migration through the passive layers [52][62]. A number of corrosion studies on CoCrMo alloys against serum solutions also suggest that passive layer formation based on Co does not occur and in turn retards the formation of Cr based passive layers [58][52]. Thus, it can be inferred that Co dissolution starts as soon as specimens are immersed into the solution due to the complex organic molecular structure. There is a consensus among researchers that Cr based oxide layers (mainly Cr_2O_3 along with some Mo oxide) once formed remain stable when in contact with the serum and only dissolve gradually [63]. Thus, the observed complex behaviour of the untreated CoCrMo alloy, consisting of stable passive domain but a higher dissolution current observed in this study against Hank's solution, could be attributed to the passive layers based on Cr but along with the dissolution of Co. In the transpassive region (beyond +150 mV), the rapid rise in the corrosion current could be attributed to a number of complex phenomena consisting of formation of Cr (VI) species in the passive layers, increasing fraction of CoO and Mo (up to

around 0.79 mV), dissolution of Co beyond 0.79 mV, significant increase in the passive layer thickness and water oxidation reactions [48][50][51].

Figure 4.32 shows the surface of the untreated CoCrMo alloy after the potentiodynamic polarisation tests against Hank's solution. Figure 4.32a shows the optical microscopic image of a partially exposed and partially unaffected (which was masked) as-polished surface. Porosity associated with the manufacturing technology of the alloy could be observed prominently in both the areas. The area exposed to the solution (figure 4.32a and 4.32b) during the test clearly showed a preferential dissolution of the ε and γ phases (as compared to the carbides) along with the eventually protruded but somewhat less corroded $M_{23}C_6$ carbide dendrites. Thus, the Cr oxide based passive layers along with the relatively inert $M_{23}C_6$ offered some protection from corrosion. Raman analysis of this exposed area confirmed the formation of Cr and Mo based oxides (figure 4.36). These results were found to be consistent with the literature and with the higher anodic tranpassive dissolution currents recorded in this study. SEM images (figure 4.32c and d) show this exposed area at higher magnification. No pitting was found within the exposed area.

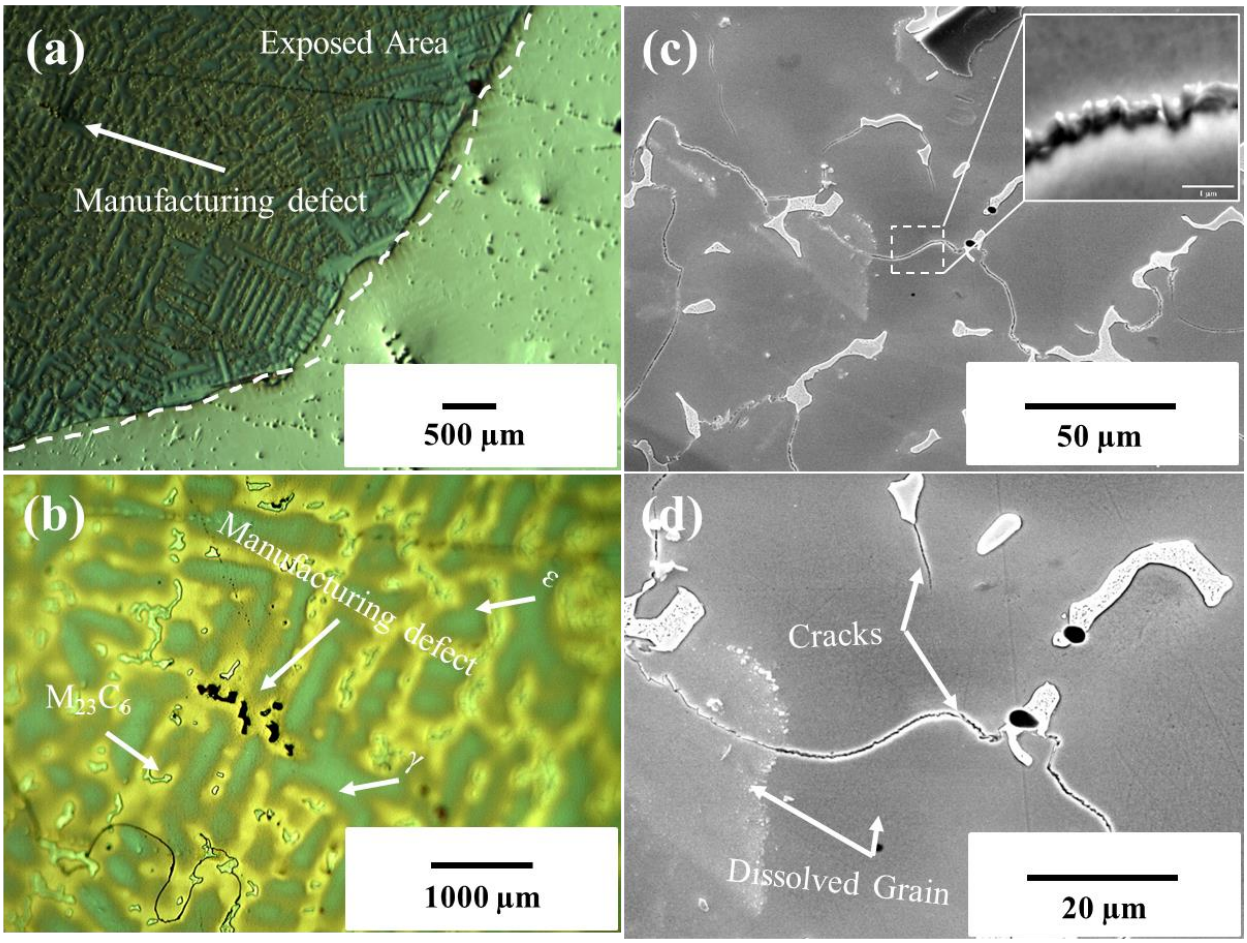

Figure 4-32: (a-b) Optical micrographs (c-d) SEM plan view of exposed area of the untreated alloy in Hank's solution at room temperature. It seems (a) has 1000 µm scale bar, while (b) has 500 µm

However, transgranular micro-cracks, presumably abetted by stress-corrosion (due to residual stress), linking the spaced-out metal carbides within the grains could also be observed in both these images. The presence of these cracks suggests that apart from matrix dissolution, abrupt removal of more corrosion resistant carbides due to matrix cracking could also act as an additional material removal mechanism. It is worth mentioning, that these cracks appear thicker than the passive layers, which are estimated to be a few manometer thick, suggesting that they ran deeper into the underneath grains.

Table 4.8 provides the E_{Corr} and the I_{Corr} values extracted from the polarisation curves of all the specimens when analysed against Hank's solution. A substantial improvement in E_{Corr} values of the nitrided specimens (in the range of 500 mV noble compared to untreated alloy)

could be observed clearly. Contrary to the results obtained against 3.5% NaCl solution, nitriding voltage did not show a clear bearing on the improvements in the E_{Corr} values. In general, the shape of the polarisation curves, especially samples nitrided at the higher voltages (-1000 V and -1100 V) mostly resembled with those obtained against the NaCl solution.

Table 4-8

OCP and polarisation data obtained from the polarisation curves of the nitrided specimens and the untreated specimen in Hank's solution (0.9 wt.% NaCl). All the electrochemical potentials reported are with respect to Ag/AgCl reference electrode.

Electrolyte	**SBF (Hank's Solution)**					
Repetition		**SET-1**			**SET-2**	
Sample ID	**E_{Corr} (mV)**	**I_{Corr} ($mAcm^{-2}$)**	**OCP (mV)**	**E_{Corr} (mV)**	**I_{Corr} ($mAcm^{-2}$)**	**OCP (mV)**
APS	-776	$2.42E^{-03}$	-777	-763	$2.50E^{-03}$	-738
-700 V	-223	$1.63E^{-04}$	-62	-231	$1.52E^{-04}$	-62
-900 V	-218	$4.12E^{-04}$	-19	-205	$3.18E^{-04}$	-56
-1000 V	-260	$6.58E^{-04}$	-149	-243	$6.92E^{-04}$	-155
-1100 V	-250	$4.00E^{-03}$	-183	-240	$3.61E^{-03}$	-197

A significant influence of the nitriding process (voltage and hence microstructure) can be observed on the corrosion currents recorded. According to the corrosion currents recorded until around +800 mV, the results could be divided into two categories: (1) results which had significantly lower anodic corrosion currents for specimens nitrided at low voltages (-700V and -900V); and (2) results which show higher corrosion currents amid a stable passivation domain for samples nitrided at higher voltages (-1000 V and -1100V).

As described in section 4.2.2, the microstructure of nitrided layer for -700 V and -900 V samples [figure 4.4 (b,c)] predominately consisted of a distinct, uniform S phase band at the interface of the base alloy followed by a compound layer consisting of both $M_{2\text{-}3}N$ and M_4N (where M is mostly Co dominated) amid slight differences in thickness. Despite the solution being made up of several inorganic salts and aggressive chloride and sulphate ions, the

beneficial effect of the diffusion- based S phase and the $Co_{2\text{-}3}N$ + Co_4N compound layer in retarding the dissolution of the passive layers and the outward diffusion of Co were clearly evident from the polarization curves. Figure 4.33 shows SEM images of the corroded surfaces of the samples nitrided at -700 V and -900 V specimens.

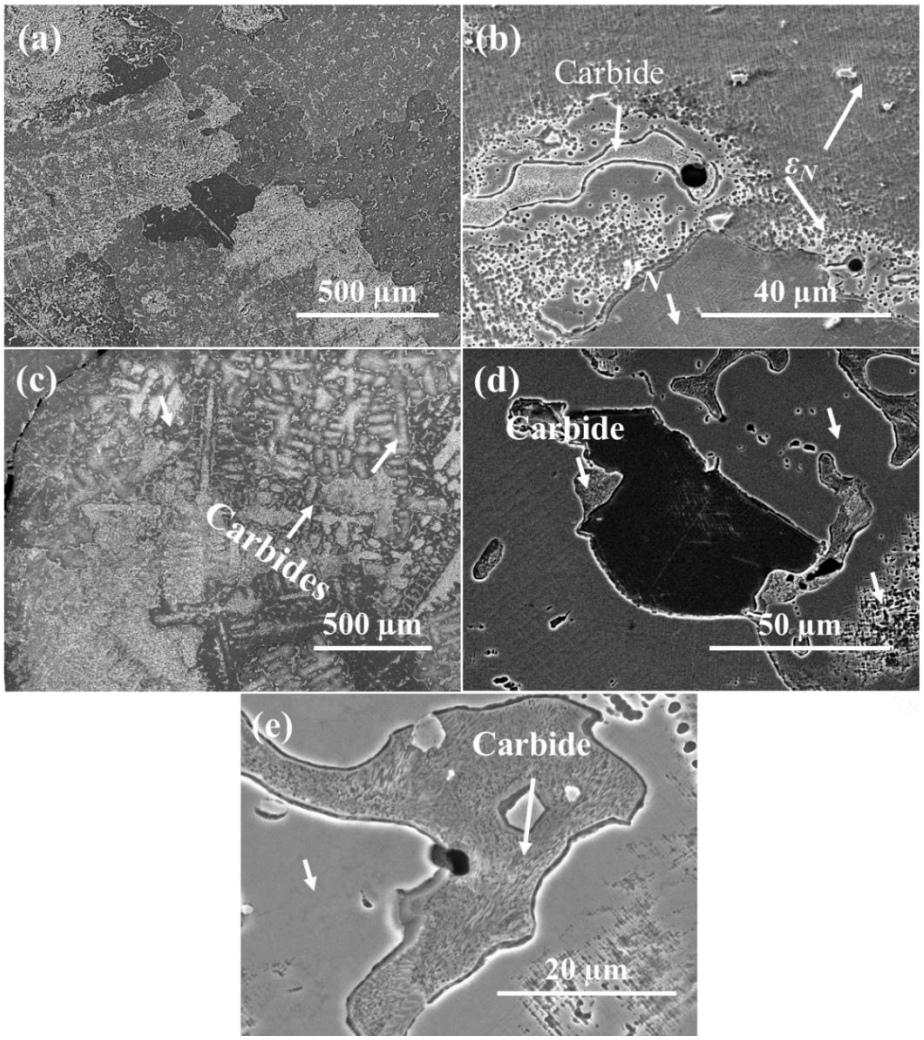

Figure 4-33: SEM plan view images of the corroded areas (a) -700 V sample: centre of the exposed area (b) high magnification image of corroded metal carbide (c) -900 V sample (d-e) area depicting the intersection of γ_N and metal carbide after potentiodynamic polarisation test in Hank's solution.

The low magnification SEM image of the corroded surface of the -700 V nitrided sample (figure 4.33a) shows different grains with a varying degree of corrosion intensity, however, exposing the partially dissolved metal carbides, most of them protruding prominently from the surrounding matrix, irrespective of their concentration in the grains. Figure 4.33b shows the corroded surface at a higher magnification of the same sample. The image focuses

on a metal carbide surrounded by a ϵ_N and a γ_N grain. Extensive preferential dissolution of a ϵ_N grains (grain boundary) and the metal carbide interface could be observed along with extensive micro pitting in the ϵ_N grain in the immediate vicinity of the metal carbide. Similar results of preferential dissolution of grain boundaries surrounding the metal carbides (due to Cr denudation leading to enhanced galvanic effects) have been reported earlier [64]. Inherent porosity arising from the manufacturing technology could also be observed. In general, the γ_N grains exhibited negligible changes in spatial features suggesting a gradual corrosion of these which was consistent with the gradual rise in the corrosion currents observed in the polarisation curve recorded for this sample. Figure 4.33(c-e) shows the corroded surface of the -900 V nitrided sample. In this case as well, preferential dissolution of the ϵ_N grains resulting in the carbides being exposed (figure 33c), preferential dissolution of the interface of metal carbide and ϵ_N grain (figure 4.33(d-e)) could be observed prominently. Table 4.9 gives the atomic percentage (at%) of Cr and N measured in the γ_N and the ϵ_N grains of the uncorroded nitrided specimens in this study with the help of the EDS technique. The results suggest that the ϵ_N grains are depleted of Cr as compared to the γ_N grains. This could explain the preferential dissolution of the ϵ_N since they lose out on the protective Cr oxide based passive layer formation [65]. The lower corrosion rate of the -700V and -900 V nitrided samples as compared to the untreated could be thus attributed to corrosion resistant γ_N grains and to some extent to the thicker 'S' phase diffusion layer (around 123-283 nm).

Table 4-9

Elemental composition in terms of Cr and N content measured in the γ_N and the ε_N grains with the help of EDX technique.

Sample ID		**Phases (at. %)**	
		γ_N	ε_N
-700 V	**Cr**	24.9 ± 0.34	23.6 ± 0.32
	N	26.9 ± 0.26	29.13 ± 0.03

-900 V	**Cr**	25.5 ± 0.15	24.4 ± 0.21
	N	26.5 ± 0.08	23.2 ± 0.17
-1000 V	**Cr**	24.3 ± 0.14	23.9 ± 0.16
	N	24.7 ± 0.28	25.6 ± 0.50
-1100 V	**Cr**	26.16 ± 0.14	24.2 ± 0.19
	N	20.56 ± 0.21	25.23 ± 0.19

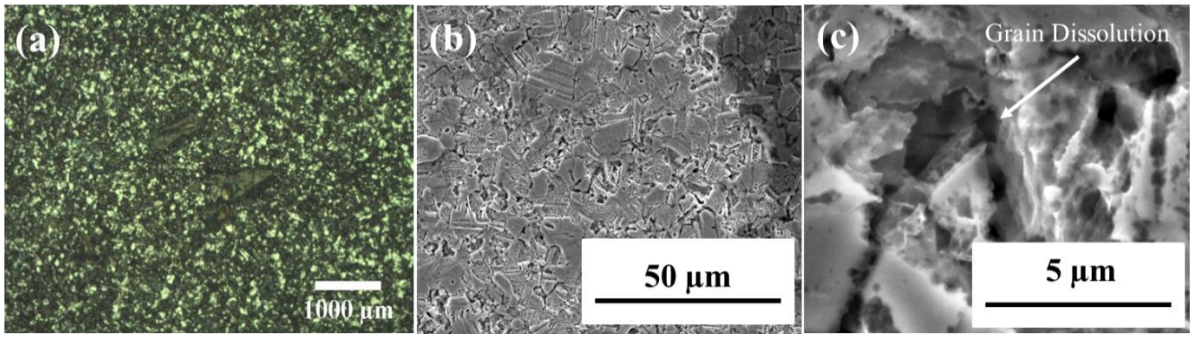

Figure 4-34: (a) Bright field optical micrograph of the -1000 V sample (b) SEM plan view of centre of exposed area of sample and (c) SEM plan view of dissolved grain boundary area along the ϵ_N grains at higher magnification.

Figure 4.34 shows the exposed surface area of sample nitrided at -1000 V after potentiodynamic polarisation test in Hank's solution. At low magnification, the microstructure of the sample showed random distribution of fine grains of ϵ_N (dark constrast) γ_N (bright contrast) phases (figure 4.34a). The dark contrast in the bright field optical image was due to the scattering of light associated with roughness due to corrosion. Figure 4.34 (b) shows the SEM image of this corroded area at higher magnification. On a closer look, significant dissolution of the grain boundaries, preferably along the ϵ_N grains could be prominently observed. Literature suggests that any precipitation of CrN/Cr_2N will happen along the grain boundaries [66][67]. Figure 34c shows such a dissolved area near the grain boundaries at a higher magnification. It revealed that these terminate into pits which run deeper into the specimen, presumably breach the diffusion-based S phase layer and reach untreated alloy with the passage of time. It could also be speculated that, the application of higher nitriding voltages, results in S phase diffusion layer with higher defect densities due to the more intensive ion bombardment. XRD results also suggested that higher nitriding voltages (>1000 V and -1100

V in this case) promoted the formation of ϵ_N phase [1]. Thus, the poor corrosion resistance of the ϵ_N grains along with the amplified galvanic effects due to compositional changes associated with nitride precipitation along the grain boundaries could be attributed to the enhanced corrosion of these areas. This is consistent with the steep rise of corrosion currents recorded for this sample from the E_{Corr} to almost +200 mV (figure 4.31b). The sharp passivation domain seen from around +200 mV to around +800 mV could be thus attributed to the response from the corrosion resistant S phase [55] (albeit thinner than the previous two samples) and the freshly exposed base alloy.

Figure 4.35 shows the corroded areas of the sample nitrided at -1100 V. As evident from the bright and dark contrast areas in the optical image (figure 4.35(a)), the corrosion performance and mechanism of this sample resembled to that of the -1000 V. Figure 4.35(b), shows a pit formed at the junction of three different grains due to preferential dissolution. Apart from the grain boundary dissolution mechanism, intergranular cracks were also found for this sample. XRD results showed that this sample had the maximum lattice expansion due to higher nitrogen incorporation along with the preferred formation of ϵ_N phase[1]. Thus, the cracking could be attributed to higher intrinsic stress of the nitrided layer facilitated by corrosion (stress-corrosion), which in turn contributed to the higher corrosion currents by providing the solution a direct path to the areas below.

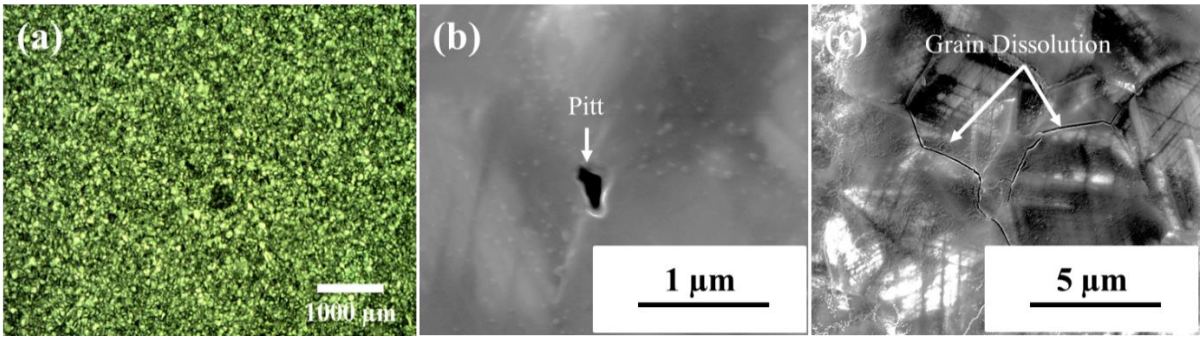

Figure 4-35: Corroded area of the sample nitrided at -1100 V; (a) Optical micrograph of the corroded area (b) SEM image of pit formed near the grain boundaries (c) Intergranular cracking.

Figure 4.36 exhibits the Raman spectra of the nitrided, and untreated specimens obtained from different section of the corroded area (which were peculiar and anticipated to be associated with the corrosion products). It was clear from the Raman spectra, that all the specimens indicated the formation of metal oxides (MOs) mainly based on Cr and Mo. No evidence of Co based oxides was found throughout the exposed area, which reiterated that Co did not form oxides which reaffirms results available through the literature.

From the figure 4.36, it could be seen that no phases of any MOs were observed in the frequency range of 200-400 cm^{-1} for untreated alloy. Above 400 cm^{-1} frequency, peaks related to CrO_2, MoO_2 (E_g band), Cr_2O_3 (both A_{1g} and E_g band), CrO_2 (B_{2g} band), CrO_3, Cr_8O_{21} and Mo_4O_{11} could be observed [61]-[72]. Most of these peaks originated from the areas near the γ_N and carbides. However, no clear peaks on ϵ_N phases were found. Even though the intensity of the Cr_2O_3 and CrO_2/MoO_2 peaks changed as the sample was scanned from different areas within the corroded portions, the nature and the combination of the phase remained the same.

Raman spectra obtained for nitrided specimen hinted the formation of different Cr and Mo oxides. As it could be seen form the figure 4.36, Cr_2O_3 phase dominated in all nitrided specimens. The highest intensity of Cr_2O_3 was observed in the case of -700 V which corresponded to Eg bending. Whereas, for -900 V sample, both A_{1g} and E_g bending of Cr_2O_3 contributed the most compared to other Cr and Mo oxide phases. Apart from these phases, spectra of nitrided specimens were also found to have three extra MO peaks which were observed at the start of the scan (200-400 cm^{-1}).

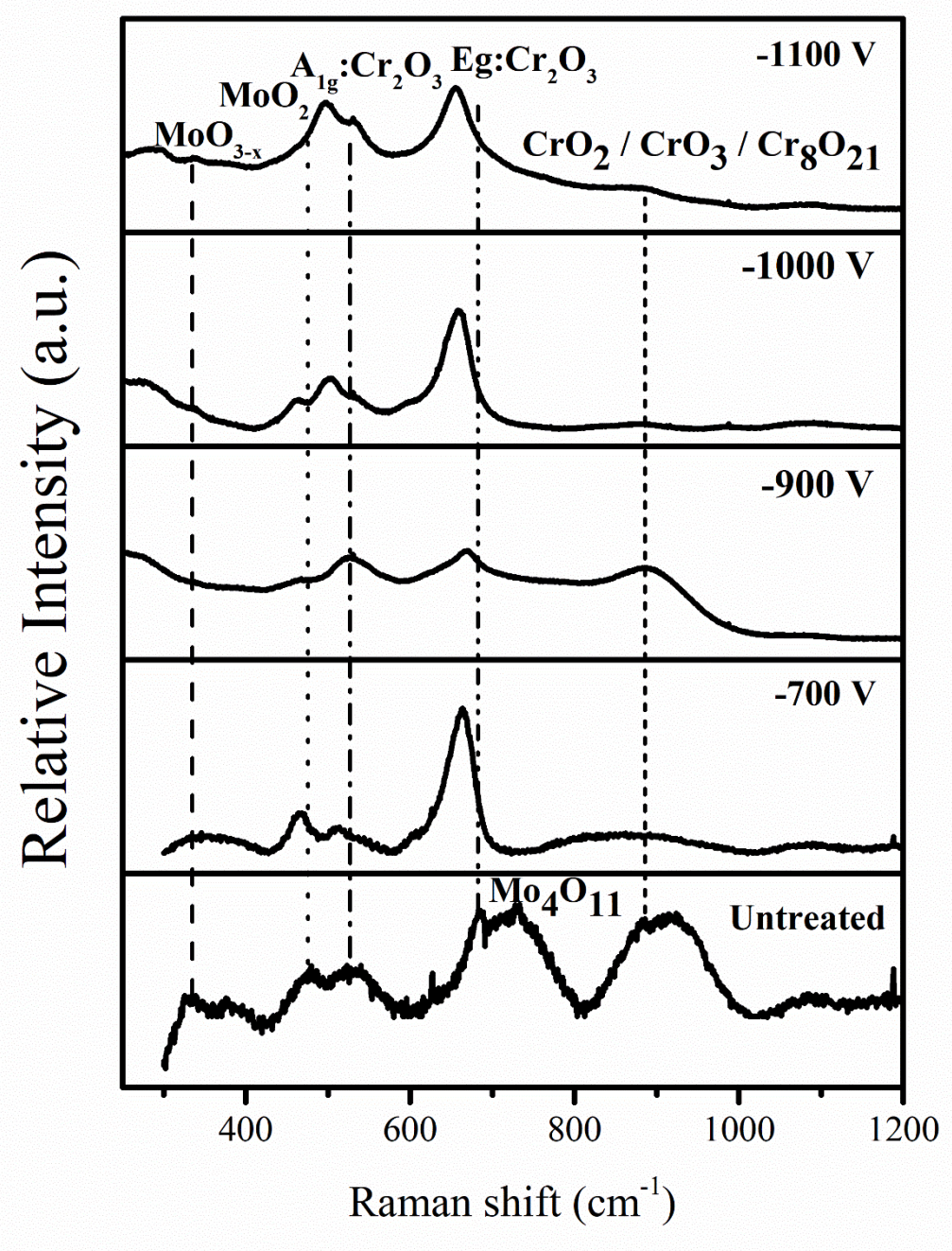

Figure 4-36: Raman spectra obtained from the corroded areas of the untreated and the nitrided alloys.

As presented in table 4.10, these peaks corresponded to the formation of MoO_3, CrO_4 and CrO_6 and correlates to the v_4 bending mode [68][69]. However, peak position of these phases were slightly shifted from the original position (285 cm^{-1} B_{2g}: δ O=M=O, wagging) [68]. Peak shifting is often associated with the roughness of the exposed area due to the multiple scattering of phonons. Surprisingly, both CrO_4 and CrO_6 phases were not observed for the -700 V and -1000 V samples. On the other hand, MoO_3 was observed for all sample nitrided at

higher voltage (≥ -900 V). At the same time, no evidence of CrO_2 (B_{2g}) and Mo_4O_{11} was found in any of the nitrided specimens. At the end of the spectra, a board peak (frequency range between 800 to 900 cm^{-1}) was observed which corresponded to amorphous Cr oxides.

Some of the peaks were found to have similar frequency as other phases such as CrO_3 or $Cr_8O_{21}$and Mo_4O_{11} which have orthorhombic crystal structure. The peak at 907 cm^{-1} corresponded to both CrO_3 and Mo_4O_{11}, whereas this peak (Mo_4O_{11}) was attributed to terminal Mo-O vibration. Interestingly, Raman peaks related to Co oxides (balanced element) were not found which indicated that Co mainly dissolves during the tests into electrolyte (Hank's solution). Likewise, CrO and MoO phases were absent and could not be indexed.

Table 4-10

Raman spectra obtained from the corroded area of the untreated and the nitrided alloys.

Type of Metal Oxide	APS	Sample A	Sample B	Sample C	Sample D
MoO_{3-x} **CrO_4 (v_4 bending)** **CrO_6 (v_4 bending)**			274.6	280.19	287.41
			335.53		337.93
			391.66		387.83
CrO_2 (E_g)	479.92	464.3	465.44	472.65	497.51
MoO_2 (E_g)	508.08	514.3		516.76	
Cr_2O_3 (A_{1g})	522.94		526.38		531.19
	540.15	540.9			
Cr_2O_3 (E_g)	626.98	627		609.78	
	634.81	663.8	668.32		654.59

	683.31	665.3		675.54	
CrO_2 (B_{2g})	702.86				
	709.09				
Mo_4O_{11}	733.37				
	746.68				
CrO_3 or Cr_8O_{21}	829.59	857			
	885.92	862.5	886.45	878.43	870.41
Mo_4O_{11}	907.82				
	923.47				

In summary, A significant improvement in the E_{Corr} values was observed irrespective of the nitriding voltage as compared to the untreated alloys. Microstructure played a significant role in determining the corrosion resistance, wherein the grains and the grain boundaries seemed to preferentially corrode as compared to the grains. Also, precipitation of Cr based nitrides (CrN and Cr_2N) observed for higher nitriding voltages of -1000 V and -1100 V deteriorated the corrosion resistance of the nitrided alloy. The nitrided alloy appeared to draw its corrosion resistance from the corrosion resistant grains and the diffusion-based S phase layers. CS-SEM studies revealed that this layer was thickest in the case of -900 V. The specimens nitrided at -900 V exhibited the best corrosion resistance followed by the those nitrided at -700 V in both test environments. This could be attributed due to right combination of a thicker S phase diffusion-based layer at the substrate interface and a compound layer ($M_{2-3}N$ and M_4N, where M is mainly Co dominated) which produced Cr + Mo based passive layers when subjected to corrosive conditions.

References:

[1] M. Jenko *et al.*, "Surface chemistry and microstructure of metallic biomaterials for hip and knee endoprostheses," *Appl. Surf. Sci.*, vol. 427, pp. 584–593, 2018, doi: 10.1016/j.apsusc.2017.08.007.

[2] J. A. Ortega-Saenz, M. A. L. Hernandez-Rodriguez, V. Ventura-Sobrevilla, R. Michalczewski, J. Smolik, and M. Szczerek, "Tribological and corrosion testing of surface engineered surgical grade CoCrMo alloy," *Wear*, 271 (9-10) 2011, pages: 2125-2131. doi: 10.1016/j.wear.2010.12.062.

[3] O. Öztürk, S. Okur, and J. P. Riviere, "Structural and magnetic characterization of plasma ion nitrided layer on 316L stainless steel alloy," *Nucl. Instruments Methods Phys. Res. Sect. B Beam Interact. with Mater. Atoms*, 267 (8-9) 2009, pages: 1540-1545 doi: 10.1016/j.nimb.2009.01.076.

[4] D. B. Lewis *et al.*, "The influence of the yttrium content on the structure and properties of Ti1-x-y-zAlxCryYzN PVD hard coatings," *Surf. Coatings Technol.*, vol. 114, no. 2–3, pp. 187–199, 1999, doi: 10.1016/S0257-8972(99)00047-X.

[5] J. V. Giacchi, C. N. Morando, O. Fornaro, and H. A. Palacio, "Microstructural characterization of as-cast biocompatible Co-Cr-Mo alloys," *Mater. Charact.*, vol. 62, no. 1, pp. 53–61, 2011, doi: 10.1016/j.matchar.2010.10.011.

[6] J. B. Park, K.-H. Jung, K. M. Kim, Y. Son, J.-I. Lee, and J. H. Ryu, "Microstructure of As-cast Co-Cr-Mo Alloy Prepared by Investment Casting," *J. Korean Phys. Soc.*, vol. 72, no. 8, pp. 947–951, 2018, doi: 10.3938/jkps.72.947.

[7] S. Mineta, Alfirano, S. Namba, T. Yoneda, K. Ueda, and T. Narushima, "Phase and morphology of carbides in ASTM F75 Co-Cr-Mo-C alloys formed at 1473 to 1623 K," *Mater. Sci. Forum*, vol. 654–656, pp. 2176–2179, 2010, doi:

10.4028/www.scientific.net/MSF.654-656.2176.

[8] A. Çelik, Ö. Bayrak, A. Alsaran, I. Kaymaz, and A. F. Yetim, “Effects of plasma nitriding on mechanical and tribological properties of CoCrMo alloy,” *Surf. Coatings Technol.*, vol. 202, no. 11, pp. 2433–2438, 2008, doi: 10.1016/j.surfcoat.2007.08.030.

[9] K. Shukla, A. A. Sugumaran, I. Khan, A. P. Ehiasarian, and P. E. Hovsepian, “Low pressure plasma nitrided CoCrMo alloy utilising HIPIMS discharge for biomedical applications,” *J. Mech. Behav. Biomed. Mater.*, vol. 111, no. August, p. 104004, 2020, doi: 10.1016/j.jmbbm.2020.104004.

[10] H. Dong, “S-phase surface engineering of Fe-Cr, Co-Cr and Ni-Cr alloys,” *Int. Mater. Rev.*, vol. 55, no. 2, pp. 65–98, Mar. 2010, doi: 10.1179/095066009X12572530170589.

[11] M. Berg *et al.*, “On plasma nitriding of steels,” *Surf. Coatings Technol.*, vol. 124, no. 1, pp. 25–31, 2000, doi: 10.1016/S0210-4806(00)72445-4.

[12] B. Predel, “Co-N (Cobalt-Nitrogen),” in *Ca-Cd -- Co-Zr*, O. Madelung, Ed. Berlin, Heidelberg: Springer Berlin Heidelberg, 1993, pp. 1–3.

[13] P. Hovsepian, G. Thompson. B. Lewis, A. Ehiasarian, and W.-D. Munz, *Performance of High-Precision Knife Blades Treated by Plasma Nitriding and PVD Coating*. 2003.

[14] D. L. Williamson, “No Title,” *mat. Res. Soc. Symp/SAVEProc*, p. 473.

[15] A. Petraitienė, “The Modeling of Nitrogen Mass Transport in CoCr Alloys,” *JELGAVA ISSN Rural Sustain. Res.*, 36 (331) 2016, pages: 19-26. doi: 10.1515/plua-2016-0010.

[16] S. Parascandola, W. Möller, and D. L. Williamson, “The nitrogen transport in austenitic stainless steel at moderate temperatures,” *Appl. Phys. Lett.*, vol. 76, no. 16, pp. 2194–2196, 2000, doi: 10.1063/1.126294.

[17] T. Balusamy, T. S. N. S. Narayanan, K. Ravichandran, I. S. Park, and M. H. Lee, “Plasma nitriding of AISI 304 stainless steel: Role of surface mechanical attrition

treatment," *Mater. Charact.*, vol. 85, pp. 38–47, 2013, doi: 10.1016/j.matchar.2013.08.009.

[18] O. Al-Mana, M. S. J. Hashmi, and B. S. Yilbas, "Laser nitriding of titanium alloy and fracture toughness measurement of resulting surface," *Adv. Mater. Res.*, vol. 445, pp. 615–620, 2012, doi: 10.4028/www.scientific.net/AMR.445.615.

[19] J. Chen, H. Li, and B. D. Beake, "Load sensitivity in repetitive nano-impact testing of TiN and AlTiN coatings," *Surf. Coatings Technol.*, vol. 308, pp. 289–297, 2016, doi: 10.1016/j.surfcoat.2016.05.094.

[20] ASTM E399 "Standard Test Method for Linear-Elastic Plane-Strain Fracture Toughness K Ic of Metallic Materials," 2010, doi: 10.1520/E0399-09E02.2.

[21] Q. Yao, J. Sun, G. Zhang, W. Tong, and H. Zhang, "Enhanced toughness of nitrided layers formed on Ti-6Al-4V alloy via surface mechanical attrition pre-treatment," *Vacuum*, vol. 142, pp. 45–51, 2017, doi: 10.1016/j.vacuum.2017.05.004.

[22] Q. Yao, J. Sun, Y. Fu, W. Tong, and H. Zhang, "An evaluation of a borided layer formed on Ti-6Al-4V alloy by means of SMAT and low-temperature boriding," *Materials (Basel).*, 9,(12) 2016, pages: 1-10. doi: 10.3390/ma9120993.

[23] S. Suwas and R. K. Ray, "Texture and Properties," in *Crystallographic Texture of Materials*, London: Springer London, 2014, pp. 207–223.

[24] P. Manda, U. Chakkingal, and A. K. Singh, "Hardness characteristic and shear band formation in metastable β-titanium alloys," *Mater. Charact.*, vol. 96, pp. 151–157, 2014, doi: 10.1016/j.matchar.2014.07.027.

[25] S. Jana, U. Ramamurty, K. Chattopadhyay, and Y. Kawamura, "Subsurface deformation during Vickers indentation of bulk metallic glasses," *Mater. Sci. Eng. A*, vol. 375–377, no. 1-2 SPEC. ISS., pp. 1191–1195, 2004, doi: 10.1016/j.msea.2003.10.068.

[26] M. Bagheripoor and R. Klassen, “The effect of crystal anisotropy and pre-existing defects on the incipient plasticity of FCC single crystals during nanoindentation,” *Mech. Mater.*, vol. 143, no. September 2019, p. 103311, 2020, doi: 10.1016/j.mechmat.2020.103311.

[27] Y. Kato, H. Yamazaki, S. Yoshida, and J. Matsuoka, “Effect of densification on crack initiation under Vickers indentation test,” *J. Non. Cryst. Solids*, vol. 356, no. 35–36, pp. 1768–1773, 2010, doi: 10.1016/j.jnoncrysol.2010.07.015.

[28] X. Chen, Y. Du, and Y. W. Chung, “Commentary on using H/E and H3/E2 as proxies for fracture toughness of hard coatings,” *Thin Solid Films*, volume: 688, 31 october 2019, pp.137265, doi: 10.1016/j.tsf.2019.04.040.

[29] Y. Sun, X. Li, and T. Bell, “Low temperature plasma carburising of austenitic stainless steels for improved wear and corrosion resistance,” *Surf. Eng.*, vol. 15, no. 1, pp. 49–54, 1999, doi: 10.1179/026708499322911647.

[30] T. Bell, “Surface engineering of austenitic stainless steel,” *Surf. Eng.*, vol. 18, no. 6, pp. 415–422, Dec. 2002, doi: 10.1179/026708402225006268.

[31] K. Chen, W. Jiang, X. Cui, and S. Wang, “Effect of nanoparticles on the tribo-layers and the tribology of a steel-on-steel couple,” *Proc. Inst. Mech. Eng. Part J J. Eng. Tribol.*, vol. 233, no. 1, pp. 30–40, Jan. 2019, doi: 10.1177/1350650118765005.

[32] E. J. Mittemeijer, “Fundamentals of Nitriding and Nitrocarburizing,” in *ASM Handbook: Steel Heat Treating Fundamentals and Processes*, vol. 4A, . Dossett and G.E. Totten, Ed. 2013, pp. 619–646.

[33] C. . Li and T. Bell, “Sliding wear properties of active screen plasma nitrided 316 austenitic stainless steel,” *Wear*, vol. 256, no. 11–12, pp. 1144–1152, Jun. 2004, doi: 10.1016/j.wear.2003.07.006.

[34] J. Singh, V. Verma, and R. Kumar, “Preparation and structural, optical studies of Al substituted chromium oxide (Cr2O3) nanoparticles,” *Vacuum*, vol. 159, no. July 2018, pp. 282–286, 2019, doi: 10.1016/j.vacuum.2018.09.033.

[35] M. Mohammadtaheri, Q. Yang, Y. Li, and J. Corona-Gomez, “The effect of deposition parameters on the structure and mechanical properties of chromium oxide coatings deposited by reactive magnetron sputtering,” *Coatings*, vol. 8, no. 3, pp. 1–14, 2018, doi: 10.3390/coatings8030111.

[36] L. Xin, Y. Lu, and T. Shoji, “The comparative study on nanostructured tribolayers of Alloy 690TT subjected to fretting wear under different oxygen contents,” *Mater. Charact.*, vol. 131, no. March, pp. 157–167, 2017, doi: 10.1016/j.matchar.2017.04.034.

[37] M. Roy, S. Ghosh, and M. K. Naskar, “Solvothermal synthesis of Cr2O3 nanocubes via template-free route,” *Mater. Chem. Phys.*, vol. 159, pp. 101–106, 2015, doi: 10.1016/j.matchemphys.2015.03.058.

[38] L. Kumari *et al.*, “X-ray diffraction and Raman scattering studies on large-area array and nanobranched structure of 1D MoO2 nanorods,” *Nanotechnology*, vol. 18, no. 115717, 2007, pp. 1-7, doi: 10.1088/0957-4484/18/11/115717.

[39] S. K. S. Patel *et al.*, “Synthesis of α-MoO3 nanofibers for enhanced field-emission properties,” *Adv. Mater. Lett.*, vol. 9, no. 8, pp. 585–589, 2018, doi: 10.5185/amlett.2018.2022.

[40] S. Kikuchi, K. Kawauchi, M. Kurosawa, H. Honjho, and T. Yagishita, “Non-destructive rapid analysis discriminating between chromium(VI) and chromium(III) oxides in electrical and electronic equipment using Raman spectroscopy,” *Anal. Sci.*, vol. 21, no. 3, pp. 197–198, 2005, doi: 10.2116/analsci.21.197.

[41] O. Monnereau *et al.*, “Chromium oxides mixtures in PLD films investigated by Raman

spectroscopy," *J. Optoelectron. Adv. Mater.*, vol. 12, no. 8, pp. 1752–1757, 2010.

[42] M. N. Iliev, A. P. Litvinchuk, H. G. Lee, C. W. Chu, A. Barry, and J. M. D. Coey, "Raman spectroscopy of ferromagnetic CrO2," *Phys. Rev. B - Condens. Matter Mater. Phys.*, vol. 60, no. 1, pp. 33–36, 1999, doi: 10.1103/PhysRevB.60.33.

[43] D. Stanoi *et al.*, "Chromium oxides thin films prepared and coated in situ with gold by pulsed laser deposition," *Mater. Sci. Eng. B Solid-State Mater. Adv. Technol.*, vol. 118, no. 1–3, pp. 74–78, 2005, doi: 10.1016/j.mseb.2004.12.016.

[44] P. Hones, M. Diserens, and F. Lévy, "Characterization of sputter-deposited chromium oxide thin films," *Surf. Coatings Technol.*, vol. 120–121, pp. 277–283, 1999, doi: 10.1016/S0257-8972(99)00384-9.

[45] P. Prieto, J. F. Marco, A. Serrano, M. Manso, and J. de la Figuera, "Highly oriented (111) CoO and Co3O4 thin films grown by ion beam sputtering," *J. Alloys Compd.*, vol. 810, no. 111, p. 151912, 2019, doi: 10.1016/j.jallcom.2019.151912.

[46] D. Wu *et al.*, "Mixed Molybdenum Oxides with Superior Performances as an Advanced Anode Material for Lithium-Ion Batteries," *Sci. Rep.*, vol. 7, no. March, pp. 1–9, 2017, doi: 10.1038/srep44697.

[47] I. Esparza *et al.*, "Solid State Reactions in Cr2O3-ZnO Nanoparticles Synthesized by Triethanolamine Chemical Precipitation," *Mater. Sci. Appl.*, vol. 02, no. 11, pp. 1584–1592, 2011, doi: 10.4236/msa.2011.211212.

[48] I. Milošev and H. H. Strehblow, "The composition of the surface passive film formed on CoCrMo alloy in simulated physiological solution," *Electrochim. Acta*, vol. 48, no. 19, pp. 2767–2774, 2003, doi: 10.1016/S0013-4686(03)00396-7.

[49] Y. S. Li, R. Wang, P. He, B. X. Huang, and P. Kovacs, "Surface-enhanced Raman spectroelectrochemical studies of corrosion films on implant Co-Cr-Mo alloy in

biosimulating solutions," *J. Raman Spectrosc.*, vol. 30, no. 2, pp. 97–103, 1999, doi: 10.1002/(SICI)1097-4555(199902)30:2<97::AID-JRS352>3.0.CO;2-X.

[50] N. Espallargas, C. Torres, and A. I. Muñoz, "A metal ion release study of CoCrMo exposed to corrosion and tribocorrosion conditions in simulated body fluids," *Wear*, vol. 332–333, pp. 669–678, 2015, doi: 10.1016/j.wear.2014.12.030.

[51] A. Bazzoni, S. Mischler, and N. Espallargas, "Tribocorrosion of Pulsed Plasma-Nitrided CoCrMo Implant Alloy," *Tribol. Lett.*, vol. 49, no. 1, pp. 157–167, Jan. 2013, doi: 10.1007/s11249-012-0047-0.

[52] M. Pourbaix, *Atlas of electrochemical equilibria in aqueous solutions. Houston:NACE International*. 1974.

[53] J. Lutz, C. Díaz, J. A. García, C. Blawert, and S. Mändl, "Corrosion behaviour of medical CoCr alloy after nitrogen plasma immersion ion implantation," *Surf. Coatings Technol.*, vol. 205, no. 8–9, pp. 3043–3049, Jan. 2011, doi: 10.1016/j.surfcoat.2010.11.017.

[54] R. Liu, "Surface Modification of ASTM F-1537 Co-Cr Alloy by Low Temperature Plasma Surface Alloying," The University of Birmingham, 2013.

[55] G. Aldrich-Smith, D. G. Teer, and P. A. Dearnley, "Corrosion-wear response of sputtered CrN and S-phase coated austenitic stainless steel," *Surf. Coatings Technol.*, vol. 116–119, pp. 1161–1165, 1999, doi: 10.1016/S0257-8972(99)00222-4.

[56] M. Aslan, O. Çomakli, M. Yazici, A. F. Yetim, Ö. Bayrak, and A. Çelik, "the effect of plasma oxidation and nitridation on corrosion behavior of cocrmo alloy in sbf solution," *Surf. Rev. Lett.*, vol. 25, no. 08, p. 1950024, Dec. 2018. doi: 10.1142/S0218625X19500240.

[57] A. Jain, "Body fluid composition," *Pediatr. Rev.*, vol. 36, no. 4, pp. 141–152, Apr. 2015,

doi: 10.1542/pir.36-4-141.

[58] F. Contu, B. Elsener, and H. Böhni, “Corrosion behaviour of CoCrMo implant alloy during fretting in bovine serum,” *Corros. Sci.*, vol. 47, no. 8, pp. 1863–1875, 2005, doi: 10.1016/j.corsci.2004.09.003.

[59] Y. N. Petrov *et al.*, “Influence of microstructural modifications induced by ultrasonic impact treatment on hardening and corrosion behavior of wrought Co-Cr-Mo biomedical alloy,” *Mater. Sci. Eng. C*, vol. 58, pp. 1024–1035, 2016, doi: 10.1016/j.msec.2015.09.004.

[60] K. Shukla, R. Rane, J. Alphonsa, P. Maity, and S. Mukherjee, “Structural, mechanical and corrosion resistance properties of Ti/TiN bilayers deposited by magnetron sputtering on AISI 316L,” *Surf. Coatings Technol.*, vol. 324, pp. 167–174, Sep. 2017, doi: 10.1016/j.surfcoat.2017.05.075.

[61] Y. Liu and B. Chen, “In vivo corrosion of CoCrMo alloy and biological responses: a review,” *Mater. Technol.*, vol. 33, no. 2, pp. 127–134, 2018, doi: 10.1080/10667857.2017.1408929.

[62] T. Hanawa, S. Hiromoto, and K. Asami, “Characterization of the surface oxide film of a Co-Cr-Mo alloy after being located in quasi-biological environments using XPS”, *Appl. Surf. Sci.*, vol. 183, no. 1–2, pages: 68–75, 2001.
doi: 10.1016/S0169-4332(01)00551-7.

[63] F. Contu and B. Elsener H Bhni, “Characterization of implant materials in fetal bovine serum and sodium sulfate by electrochemical impedance spectroscopy. I. Mechanically polished samples,” *J. Biomed. Mater. Res.*, vol. 62, no. 3, pages: 412–421, 2002. doi: 10.1002/jbm.10329.

[64] Y. Liu and J. L. Gilbert, “Effect of simulated inflammatory conditions and potential on

dissolution and surface oxide of CoCrMo alloy: In situ electrochemical atomic force microscopy study," *Electrochim. Acta*, vol. 262, pages: 252–263, 2018. doi: 10.1016/j.electacta.2017.12.151.

[65] A. Martinavičius *et al.*, "Nitrogen interstitial diffusion induced decomposition in AISI 304L austenitic stainless steel," *Acta Mater.*, vol. 60, no. 10, pages: 4065–4076, 2012. doi: 10.1016/j.actamat.2012.04.014.

[66] S. Mändl, R. Dunkel, D. Hirsch, and D. Manova, "Intermediate stages of CrN precipitation during PIII nitriding of austenitic stainless steel," *Surf. Coatings Technol.*, vol. 258, pp. 722–726, 2014. doi: 10.1016/j.surfcoat.2014.08.007.

[67] D. Manova, D. Hirsch, J. W. Gerlach, T. Höche, S. Mändl, and H. Neumann, "Nitriding of Fe-Cr-Ni films by low energy ion implantation," *Surf. Coatings Technol.*, vol. 202, no. 11, pp. 2443–2447, 2008. doi: 10.1016/j.surfcoat.2007.09.021.

[68] M. Dieterle, G. Weinberg, and G. Mestl, "Raman spectroscopy of molybdenum oxides - Part I. Structural characterization of oxygen defects in MoO3-x by DR UV/VIS, Raman spectroscopy and X-ray diffraction," *Phys. Chem. Chem. Phys.*, vol. 4, no. 5, pp. 812–821, 2002. doi: 10.1039/b107012f.

[69] R. L. Frost and M. Weier, "Raman microscopy of selected autunite minerals," *Neues Jahrb. fur Mineral. Monatshefte*, vol. 5, no. 12, pp. 575–594, 2004. doi: 10.1127/0028-3649/2004/2004-0575.

[70] K. Shukla, A. A. Sugumaran, I. Khan, A. P. Ehiasarian, and P. E. Hovsepian, "Low pressure plasma nitrided CoCrMo alloy utilising HIPIMS discharge for biomedical applications," *J. Mech. Behav. Biomed. Mater.*, vol. 111, p. 104004, Nov. 2020. doi: 10.1016/j.jmbbm.2020.104004.

[71] K. Shukla, Y. P. Purandare, I. Khan, A. P. Ehiasarian, and P. E. H. Hovsepian, "Effect

of nitriding voltage on the impact load fatigue and fracture toughness behaviour of CoCrMo alloy nitrided utilising a HIPIMS discharge," *Surf. Coatings Technol.*, vol. 400, p. 126227, Oct. 2020. doi: 10.1016/j.surfcoat.2020.126227.

[72] A. A. Sugumaran, K. Shukla, I. Khan, A. P. Ehiasarian, and P. E. Hovsepian, "Dry sliding wear mechanisms of HIPIMS plasma nitrided CoCrMo alloy for medical implant applications," *Vacuum*, vol. 185, no. December 2020, p. 109994, Mar. 2021. doi: 10.1016/j.vacuum.2020.109994.

[73] S. Zhang, D. Sun, Y. Fu, and H. Du, "Toughness measurement of thin films: a critical review," *Surf. Coatings Technol.*, vol. 198, no. 1–3, pp. 74–84, Aug. 2005. doi: 10.1016/j.surfcoat.2004.10.021.

[74] K. Khlifi, H. Dhiflaoui, L. Zoghlami, and A. Ben Cheikh Larbi, "Study of mechanical behavior, deformation, and fracture of nano-multilayer coatings during microindentation and scratch test," *J. Coatings Technol. Res.*, vol. 12, no. 3, pp. 513–524, 2015. doi: 10.1007/s11998-015-9662-7.

[75] J. J. Kruzic and R. O. Ritchie, "Determining the Toughness of Ceramics from Vickers Indentations Using the Crack-Opening Displacements: An Experimental Study," *J. Am. Ceram. Soc.*, vol. 86, no. 8, pages. 1433–1436, Aug. 2003. doi: 10.1111/j.1151-2916.2003.tb03490.x.

[76] A. Leyland and A. Matthews, "On the significance of the H/E ratio in wear control: a nanocomposite coating approach to optimised tribological behaviour," *Wear*, vol. 246, no. 1–2, pp. 1–11, Nov. 2000. doi: 10.1016/S0043-1648(00)00488-9.

Chapter 5
Comparison between HPLN and DCPN

This part of the thesis compares the commercially DC plasma nitrided (DCPN) CoCrMo alloy with HIPIMS plasma nitrided one -900 V (HLPN).

5.1. Phase Composition Analysis of DCPN and HLPN

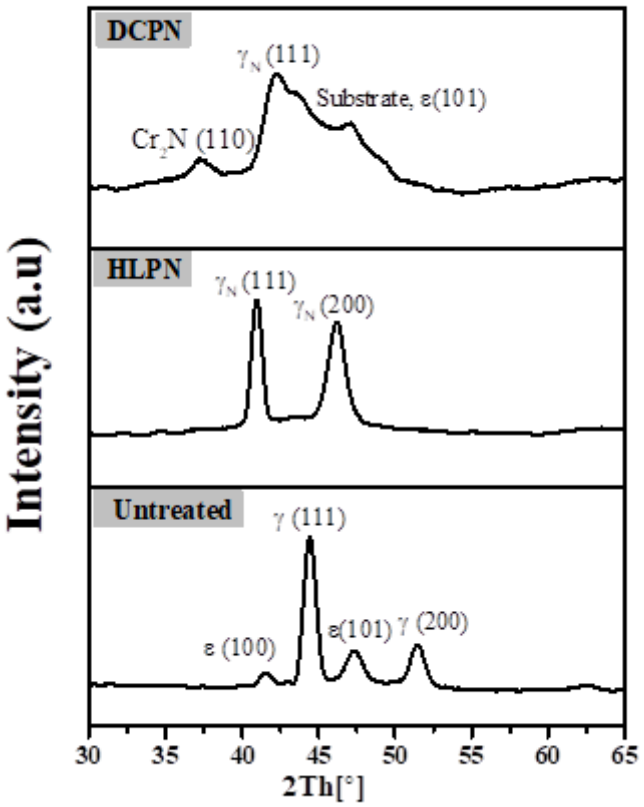

Figure 5-1: X-ray diffraction plot of untreated CoCrMo alloy, nitrided specimens (DCPN and HLPN).

Figure 5.1 depicts the X-ray diffraction of the untreated CoCrMo specimen and specimens nitrided with different techniques (DCPN and HLPN). Spectra obtained for the untreated specimen exhibited peaks which corresponded to the face centred cubic (f.c.c) γ

phases (44.53 [γ(111)] and 51.43 [γ(200)]) along with hexagonal close packed (h.c.p) α phases (peaks at 41.5 [ε(100)] and 47.5 [ε(101)]).

The XRD pattern obtained for HLPN showed the presence of peaks corresponding to two different expanded γ phases, $\gamma_N(111)$ and $\gamma_N(200)$, which were found to be shifted to lower values of 2θ as compared to untreated CoCrMo alloy. Peak shifting has been attributed mainly to the diffusion of N at octahedral position (Co-Co) in FCC crystal structure, which leads to the expansion of lattice points [1][2]. A shift in peak towards lower angle could also be due to the presence of compressive residual stresses and staking faults [2]. On the other hand, XRD patterns obtained for DCPN showed peaks corresponding to $\gamma_N(111)$ phase, (at a higher angle compared to HLPN by 1.5° (2θ)) and Cr precipitates in the form of Cr_2N (peaks at 37.5° (2θ)). Presence of a substrate peak (ε(101) indicated that the DCPN nitrided layer was thinner as compared to that of HLPN.

Table 5-1

Caption. d, a, lattice expansion and T* of the untreated, HLPN and DCPN.

Parameters	**Untreated**		**HLPN**		**DCPN**
	γ(111)	**γ(200)**	**$\gamma_N(111)$**	**$\gamma_N(200)$**	
d (nm)	0.203	0.177	0.220	0.196	0.213
a	0.351	0.354	0.381	0.392	0.368
$\Delta a/a_0*100$ %	-	-	8.56	10.92	4.84
T*	-	-	43.5	56.5	-

Table 5.1 contains interplanar distance (d), lattice constant (a), lattice expansion ($\Delta a/a_0*100$) and texture coefficient (T*). The highest d and a value were calculated for HLPN. The percentage of lattice expansion calculated for γN(111) was 8.56 % and for γN(200) was around 11 %, whereas it was 4.84 %, γN(111) for CPN. T* calculated for HLPN showed a mix-phase crystallographic orientation [(111):(200), 43.5:56.45]. In the case of CPN, (111) was

found to be the predominant crystallographic orientation. Previous works suggested that the layer consisting of both (111) and (200) phase had better corrosion, mechanical and tribological properties [2]. A (200) phase contributed to hardening of the nitrided layer whereas (111) phase enhanced it's corrosion and tribological properties [2][3][4].

5.2. Elemental Depth Profiling of DCPN and HLPN:

In principle, nitriding is a thermochemical process in which nitrogen diffuses into the matrix crystal structure through defects such as dislocations [5]. The depth of the diffusing species depends on the temperature as well as on the process time. As per the equilibrium phase diagram of Cobalt-Nitrogen (Co-N) at 400 °C, expanded γ (γ_N) phase also can be represented as Co_4N, contains nitrogen around 20-25 at%. If the diffused extra nitrogen concentration exceeds 25 at%, it develops a new phase which can be called as expanded α (α_N), $Co_{2-3}N$. Once the total amount of nitrogen reaches 50 at%, it forms a stoichiometric coating (CoN) containing an equal amount of Co and N. Figure 5.2 (a) illustrates the N_2 depth profile obtained for nitrided specimens using secondary ion mass spectrometry (SIMS) technique. As observed in the figure, the initial intense signal (count intensity) observed at the beginning of the depth profiles can be attributed to the sputtering of the thin (<10 nm) adsorption layer. As the test progressed, the concentration of N gradually decreased. Comparing the SIMS results with those of the standard calibrated specimens revealed that the maximum N concentration for HLPN was around 42 at% which also suggested the formation of $Co_{2-3}N$. As the test progressed, the N concentration decreased gradually and steadily to around 30 at% approximately at a depth of 1.3 µm from the surface. This further decreased and reached to around 2 at% giving rises to the formation of a Co_4N based diffusion layer at a depth of approximately 2.7 µm from the surface.

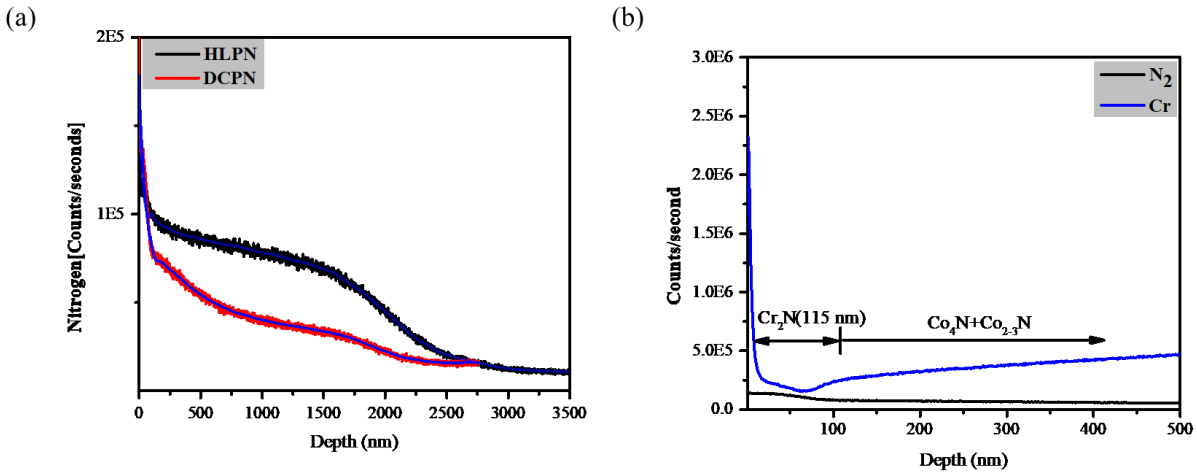

Figure 5-2: SIMS data of (a) N_2 depth profiling of DCPN and HLPN (b) Depth profiling of precipitation layer (Cr_2N) formed on the very top of the compound layer, DCPN.

The nitrogen depth profile obtained for DCPN was similar to that of HLPN. However, observed nitrogen concentration was half of the HLPN up to control depth of 1.5 µm. At start of the test, nitrogen counts for DCPN (5.5×10^5 c/s) was found to be far higher than that of HLPN (1.8×10^5 c/s) indicating the presence of Cr precipitation (lower Cr recorded up to depth of 115 nm) as shown in figure 4.38(b).

5.3. Thickness Analysis of DCPN and HLPN:

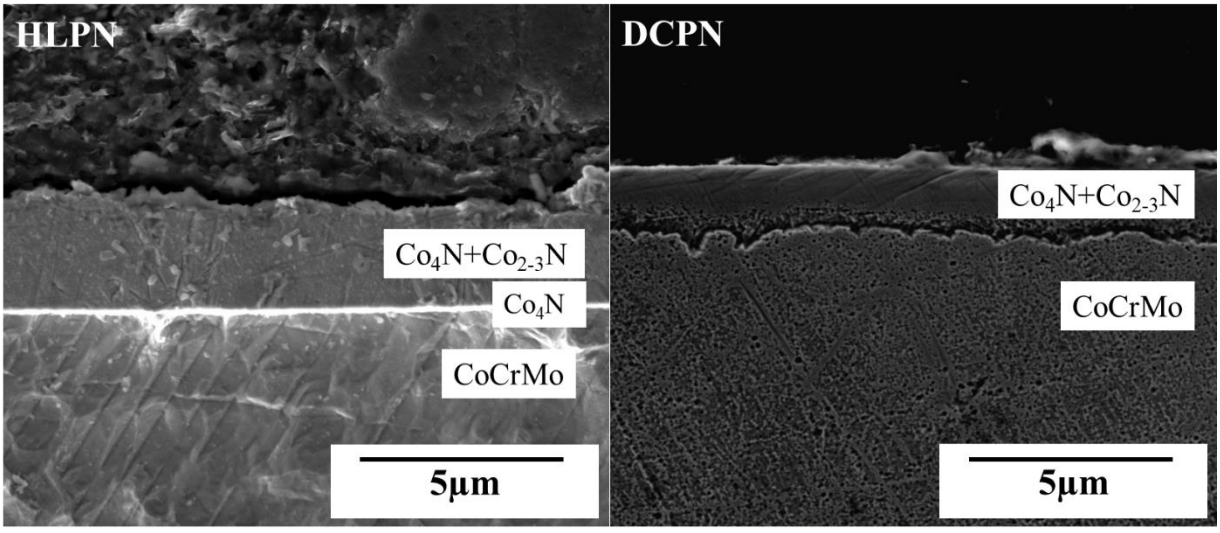

Figure 5-3: Cross-sectional SEM image of (a) HLPN and (b) DC PN.

Figure 5.3(a-b) illustrates the cross-sectional SEM images of the specimen's plasma nitrided in different discharge conditions (HLPN and DCPN). A specimen nitrided utilising HIPIMS discharge, figure 3a, clearly showed two distinct regions: (a) a thinner diffusion layer (Co_4N or also denoted as S-phase) with a bright contrast extending upward from the base CoCrMo alloy and (b), a thicker compound ($Co_{2-3}N$) layer with a grey contrast extending upward from the diffusion layer. Interestingly no distinct S-phase (Co_4N) layer was observed in the case of the DCPN nitrided specimen, figure 5.3b. The combined thickness (diffusion + compound) of the HLPN nitrided layer was around 2.8 µm and was twice thicker than that of the DCPN (1.4 µm). No evidence of chromium precipitation (CrN or Cr_2N) in the nitrided layer was found in the case of HLPN. The interface between the substrate and the nitrided layer was uniform and mainly maintained the flatness achieved through polishing the substrate. The nitrided layer appeared dense, uniform, and free of defects associated with contamination or sputtering such as chamber dust or other macroparticles. As described in the section 4.8 and 4.9 results, though no clear from the images, formation of Cr_2N on the top of the nitrided layer was observed in the case of DCPN specimens.

5.4. Mechanical and Tribological Studies of DCPN and HLPN:

Table 5-2

Hp, E, friction coefficient, wear coefficient (Kc), layer thickness (Dt), elastic (H/E) index, plastic index (H^3/E^2) and Fracture toughness (K_{Ic}) value of the untreated, HLPN and DCPN.

Sample ID	Hp (GPa)	E (GPa)	µ	Kc ($m^3N^{-1}m^{-1}$)	Dt		H/E	H^3/E^2	K_{Ic} ($MPamm^{1/2}$)
					SIMS (µm)	CS-SEM (µm)			
Untreated	8±0.0.1	249±4.9	0.81	6.00E-14	-	-	0.04	0.008	908
HLPN	23±0.5	287±3.8	0.62	1.18E-15	2.9	2.8±0.13	0.08	0.148	950
DCPN	20±0.2	276±2.6	0.60	2.20E-15	2.1	1.4±0.10	0.07	0.105	917

Table 5.2 compares the data on the surface hardness (H), Elastic modulus (E), coefficient of friction (μ), wear coefficient (K_C), elastic ratio (H/E), plastic ratio (H^3/E^2) and fracture toughness (K_{Ic}) values of the specimens analysed in this study. The highest friction coefficient, μ= 0.81 was measured for the untreated alloy. In comparison, irrespective of the nitriding technology, the nitrided specimens exhibited a near similar but lower steady state friction coefficient values of 0.6. Similarly, the K_C values measured for the nitrided specimens were more than one order of magnitude lower than that of the untreated specimen (K_C= 6.00×10^{-14} $m^3N^{-1}m^{-1}$) indicating a marked improvement in their wear resistance. The lowest K_C value was measured for the HLPN nitrided specimens (K_C= 1.18×10^{-15} $m^3N^{-1}m^{-1}$) which also exhibited the highest hardness value of 23 GPa as compared to 20 GPa and 8 GPa measured for DCPN and untreated specimens respectively. The microstructure of the HLPN nitrided layer was comprised of a diffusion layer (Co_4N) and a compound layer (Co_4N + $Co_{2-3}N$) whereas the diffusion layer was missing in the case of DCPN specimens. Thus, the superior wear resistance of the HLPN specimens could be attributed to its superior compound layer microstructure with a higher hardness and being ably supported by the diffusion layer from beneath.

5.5. Fracture Toughness (K_{Ic}) Analysis of DCPN and HLPN:

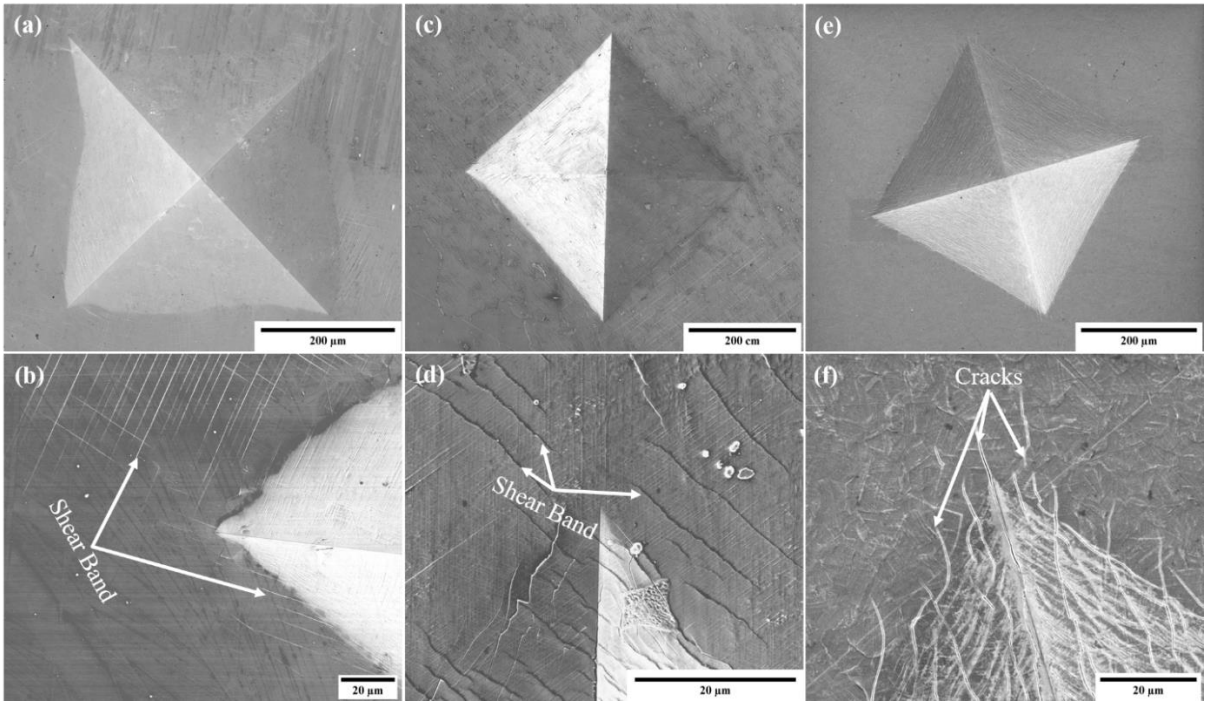

Figure 5-4: SEM images of Vickers diamond indenter impressions produced under an applied load of 50 kgf, on: (a-b) untreated alloy, (c-d) HLPN and (e-f) DC PN.

Fracture toughness (K_{Ic}) is one of the important materials properties which determines the material's resistance to crack propagation and requires special attention in applications of dynamic loading conditions. Indentation-fracture technique is one of the well-established methods to calculate fracture toughness of bulk materials and thin films, [6][7]. Recently, this approach has been successfully applied in characterising the fracture toughness and defining the K_{Ic} value of the modified layer obtained using diffusion techniques such as nitriding, [3][6].

Table 5.2 provides the K_{Ic} values calculated for all the specimens. In the conditions of the experiment the untreated alloy showed a K_{Ic} value of around 908 MPa.mm$^{1/2}$ which was relatively high considering the hardness of the alloy in the untreated state. Under the same conditions, the highest K_{Ic} value of 955 MPamm$^{1/2}$ was obtained for HIPIMS nitrided alloy. The commercially nitrided specimen (DCPN) showed around 5% lower value than that of HLPN. Increase in K_{Ic} value was found to be linked to the texture of the compound layer. The

texture values for both HLPN and CPN were calculated using the formula proposed in [3]. As per the T* analysis, the DCPN nitrided layer showed a predominant crystallographic (111) orientation whereas the HLPN nitrided layer developed a mixture of both (111) and (200). Volume fracture calculated for HLPN specimens suggested that contribution of (111) phase in the nitrided layer was (43.54 %) and for DCPN it was around 89 %.

Surface analysis of indentation impressions reveals further important information related to the fracture toughness of the modified surface layers. It was reported that in the indentation method, ideally two different types of crack modes, called radial mean and Palmquist type cracking, can be observed along the edges of the pyramidal square indent, [3][7]. Based on the proposed method, fracture toughness, K_{Ic} is inversely proportional to the crack length created along the edges of the square indents after the loading-unloading cycle.

Figure 5.4(a-f) illustrates the pyramidal square indentation impressions produced on the untreated and nitrided alloys. As expected for a material with a lower hardness (8 GPa) and high plasticity, the edges of the indentation on the untreated specimen were found to be crack free, figure 5.4(a-b). At higher magnification, the area surrounding the square indent showed presence of shear bands indicating plastic deformation during the loading-unloading cycle along with the presence of shear cracks. Development of such cracks can be attributed to the complex stress distribution in the material during the penetration of the indenter as well as the presence of some imperfections, such as micro voids (manufacturing defects) present within the substrate and the high strain developed around these voids.

Figure 5.4(c-d) shows the indentation produced on the specimen nitrided utilising the HIPIMS discharge. In general, at a lower magnification, (figure 5.4c) the area around the pyramidal square edges appeared to be crack free and implied a superior fracture toughness of the compound layer ($Co_{2\text{-}3}N+Co_4N$). At a higher magnification, a thorough surface examination showed some interesting features around the plastically deformed area, especially

around the boundary of the square impression. Both Palmquist and radial mean type cracks (figure 4.40d), which initiated and extinguished within the pyramidal faces of the indentation, were observed. Apart from these cracks, shear bands resulting from the hemispherical plastic zone (or semi-circular plastic zone) and radial stresses during the indentation were also observed [9][10][11].

Figure 5.4(e-f) shows the indentation on the specimens treated by DCPN. Numerous cracks, which were parallel to the square edges as well as parallel to the diagonals of the impression were observed. Cracks extending from the diagonals of the impression into the surrounding un-indented area were also visible. The impression was heavily cracked as compared to the HLPN and untreated impressions. At the same time the area surrounding the impression exhibited no shear bands or cracks which suggested that the layer did not deform plastically. The radial and Palmquist cracks (almost 9 to 10 µm in length) were found to have their initiation within the faces of the square impression. These findings implied that the nitrided layer was brittle in nature, had poor resistance to cracking and hence poor fracture toughness.

Literature suggests that the higher the H/E (elastic strain to failure ratio) and H^3/E^2 (plastic index) ratios, the tougher is the material with a higher ability to absorb shock without yielding (plastic deformation). This applies for all materials irrespective if the material is bulk, nanostructure coating or nitrided layer, [12][13]. In our research, the highest H/E and H^3/E^2 was calculated for the HLPN treatment which was two orders of magnitude higher than that of the untreated specimen, which demonstrates the high efficiency of the process.

5.6. Corrosion Analysis of DCPN and HLPN:

In a CoCrMo alloy, Cr contribution is around 28-30 wt% which makes this alloy more suitable for applications such as Hip and Knee implants where better corrosion resistance is an

essential requirement. The physiological environment is considered to be complex and contains amino acids, protein, lipids and various salts such as NaCl (0.9 wt.%). As soon as the metal implant submerges in the body fluid such as salt buffer solution, the material surface behaviour changes radically due to corrosion. Thus, corrosion analysis of the nitrided specimens and the as polished specimen in Hank's solution was necessary.

Figure 5.5 illustrates the polarisation curves recorded for the untreated and nitrided specimens when tested against a simulated body fluid (Hank's solution). The untreated specimen had the lowest E_{Corr} value (around -780 mV) and thus exhibited a poor corrosion resistance. A marked improvement in the E_{Corr} value was observed for both. HLPN (around -164 mV) and DCPN (around -180 mV), which implied that nitriding itself, irrespective of the technology, had a beneficial effect on the corrosion resistance of the alloy.

The curves could be easily distinguished into 3 regions: anodic dissolution domain, passive domain and a transpassive dissolution domain. In the transpassive domain (around +200 mV and above) all the specimens had a near similar behaviour and a steadily increasing corrosion current was the main feature. The formation of Cr (VI) species in the passive layers, increasing fraction of CoO and Mo, dissolution of Co at higher anodic potentials, significant increase in the passive layer thickness and dissolution of these passive films along with the water oxidation reactions can be attributed to the rapid rise in the current values [14][15][16].

Even though it had the lowest E_{Corr} value, the untreated alloys showed a stable passive region in the potential ranges of - 400 mV to + 200 mV. This stable passive region has been attributed to a mechanically stable Cr based oxide layer (mainly Cr_2O_3 along with some Mo oxide) which slowly dissolves in this potential range [2]. Co, on the contrary, preferentially and steadily dissolves by an outward migration through the passive layer [16]. Thus, even though the polarisation curve shows a steady passive domain, it's current density ($I_{Corr}= 2 \times 10^{-3}$ $mAcm^{-2}$) was the highest amongst the specimens analysed in this potential range. In comparison, the

HLPN specimen exhibited the lowest I_{Corr} value (5×10^{-5} mAcm^{-2}) whereas the DCPN specimen had an intermediate I_{Corr} value of 1×10^{-4} mA cm^{-2}.

Thus, it was clear that the HLPN specimens had the best corrosion performance in this study which could be attributed to the superior microstructure consisting of a combination of a uniform S phase band and a compound layer consisting of both $M_{2\text{-}3}N$ and M_4N (where M is mostly Co dominated). In the case of the DCPN specimens, absence of the distinct S phase layer as well as the presence of the Cr_2N precipitate layer on the top led to higher corrosion currents as compared to the HLPN specimens [2].

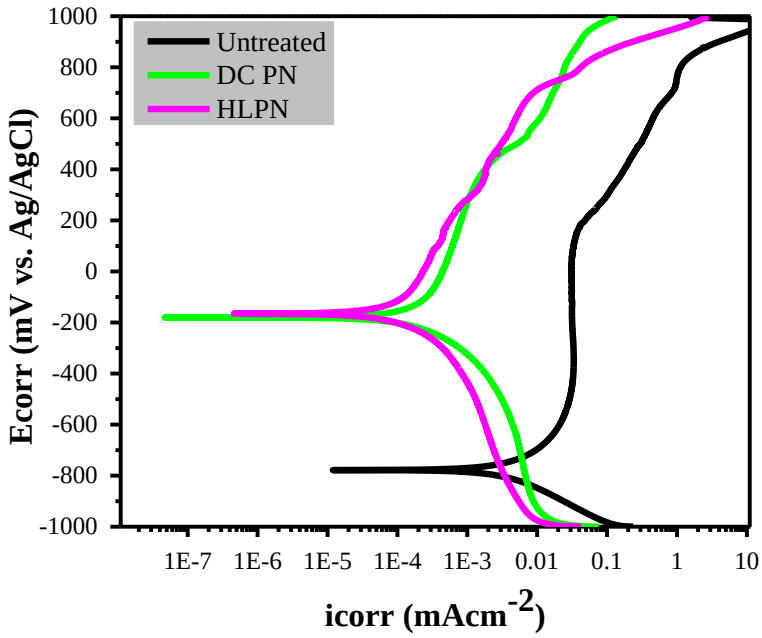

Figure 5-5: Electrochemical polarisation curve of the untreated and nitrided CoCrMo alloy in Hank's solution.

Table 5-3

ICPMS metal ion concentration measured for untreated, HLPN and DCPN.

	Co (ppb)	Cr (ppb)	Mo (ppb)
Untreated	0.7	2.2	1.3
HLPN	0.3	0.6	0.1
DCPN	0.1	1.5	0.2

Literature suggests that corrosion of the implant when in application can release Cr metal ions which can have a carcinogenic effect on the human body. With this perspective, Hank's solution from the corrosion tests was analysed to investigate for traces of any dissolved metal ions from the tests. Table 5.3 shows the concentration of Co, Cr and Mo ions found in the test solution. The lowest quantity of Cr metal ions was found in the HLPN test solution (0.6 ppb) followed by the DCPN (1.5 ppb) which confirmed the beneficial effect of nitriding, and in particular of, HIPIMS nitriding on the reduction of the Me-ion release.

References:

[1] H. Dong, “S-phase surface engineering of Fe-Cr, Co-Cr and Ni-Cr alloys,” *Int. Mater. Rev.*, vol. 55, no. 2, pp. 65–98, Mar. 2010, doi: 10.1179/095066009X12572530170589.

[2] K. Shukla, A. A. Sugumaran, I. Khan, A. P. Ehiasarian, and P. E. Hovsepian, “Low pressure plasma nitrided CoCrMo alloy utilising HIPIMS discharge for biomedical applications,” *J. Mech. Behav. Biomed. Mater.*, vol. 111, p. 104004, Nov. 2020, doi: 10.1016/j.jmbbm.2020.104004.

[3] K. Shukla, Y. P. Purandare, I. Khan, A. P. Ehiasarian, and P. E. H. Hovsepian, “Effect of nitriding voltage on the impact load fatigue and fracture toughness behaviour of CoCrMo alloy nitrided utilising a HIPIMS discharge,” *Surf. Coatings Technol.*, vol. 400, p. 126227, Oct. 2020, doi: 10.1016/j.surfcoat.2020.126227.

[4] A. A. Sugumaran, K. Shukla, I. Khan, A. P. Ehiasarian, and P. E. Hovsepian, “Dry sliding wear mechanisms of HIPIMS plasma nitrided CoCrMo alloy for medical implant applications,” *Vacuum*, vol. 185, no. December 2020, p. 109994, Mar. 2021, doi: 10.1016/j.vacuum.2020.109994.

[5] P. Hovsepian, G. Thompson. B. Lewis, A. Ehiasarian, and W.-D. Munz, *Performance of High-Precision Knife Blades Treated by Plasma Nitriding and PVD Coating*. 2003.

[6] S. Zhang, D. Sun, Y. Fu, and H. Du, “Toughness measurement of thin films: a critical review,” *Surf. Coatings Technol.*, vol. 198, no. 1–3, pp. 74–84, Aug. 2005, doi: 10.1016/j.surfcoat.2004.10.021.

[7] K. Khlifi, H. Dhiflaoui, L. Zoghlami, and A. Ben Cheikh Larbi, “Study of mechanical behavior, deformation, and fracture of nano-multilayer coatings during microindentation and

scratch test," *J. Coatings Technol. Res.*, vol. 12, no. 3, pp. 513–524, 2015, doi: 10.1007/s11998-015-9662-7.

[8] J. J. Kruzic and R. O. Ritchie, "Determining the Toughness of Ceramics from Vickers Indentations Using the Crack-Opening Displacements: An Experimental Study," *J. Am. Ceram. Soc.*, vol. 86, no. 8, pp. 1433–1436, Aug. 2003, doi: 10.1111/j.1151-2916.2003.tb03490.x.

[9] S. Jana, U. Ramamurty, K. Chattopadhyay, and Y. Kawamura, "Subsurface deformation during Vickers indentation of bulk metallic glasses," *Mater. Sci. Eng. A*, vol. 375–377, no. 1-2 SPEC. ISS., pp. 1191–1195, 2004, doi: 10.1016/j.msea.2003.10.068.

[10] M. Bagheripoor and R. Klassen, "The effect of crystal anisotropy and pre-existing defects on the incipient plasticity of FCC single crystals during nanoindentation," *Mech. Mater.*, vol. 143, no. September 2019, p. 103311, 2020, doi: 10.1016/j.mechmat.2020.103311.

[11] Y. Kato, H. Yamazaki, S. Yoshida, and J. Matsuoka, "Effect of densification on crack initiation under Vickers indentation test," *J. Non. Cryst. Solids*, vol. 356, no. 35–36, pp. 1768–1773, 2010, doi: 10.1016/j.jnoncrysol.2010.07.015.

[12] X. Chen, Y. Du, and Y. W. Chung, "Commentary on using H/E and H3/E2 as proxies for fracture toughness of hard coatings," *Thin Solid Films*, vol. 688, no. April, pp. 0–1, 2019, doi: 10.1016/j.tsf.2019.04.040.

[13] A. Leyland and A. Matthews, "On the significance of the H/E ratio in wear control: a nanocomposite coating approach to optimised tribological behaviour," *Wear*, vol. 246, no. 1–2, pp. 1–11, Nov. 2000, doi: 10.1016/S0043-1648(00)00488-9.

[14] N. Espallargas, C. Torres, and A. I. Muñoz, "A metal ion release study of CoCrMo exposed to corrosion and tribocorrosion conditions in simulated body fluids," *Wear*, vol. 332–333, pp. 669–678, 2015, doi: 10.1016/j.wear.2014.12.030.

[15] A. Bazzoni, S. Mischler, and N. Espallargas, “Tribocorrosion of Pulsed Plasma-Nitrided CoCrMo Implant Alloy,” *Tribol. Lett.*, vol. 49, no. 1, pp. 157–167, Jan. 2013, doi: 10.1007/s11249-012-0047-0.

[16] M. Pourbaix, *Atlas of electrochemical equilibria in aqueous solutions. Houston:NACE International*. 1974.

Chapter 6
Conclusions and Future Work

6.1. Conclusions

In this work, the effect of HIPIMS nitriding voltage (Bias) on the phase composition, microstructure, micro and nano hardness and dry sliding wear properties such as wear coefficient, friction coefficient, and electrochemical properties of CoCrMo alloy was investigated. Later, results were compared with benchmarked commercial DC plasma nitrided CoCrMo alloy. The following points were concluded from this work.

1. Nitriding voltage had a significant effect on the microstructure and phase composition of the nitrided layer due to the subsequent increase in ion bombardment which led in an increase in surface temperature from 400°C (-500 V) to 520°C (-1100V). The layer composition changed from pure coatings at -500V to compound layer ($Co_{2-3}N$) at -700 V, and further to mix-phase (Co_4N+$Co_{2-3}N$) at -1100 V. Below -700 V, the formed layer would be solely dominated by (Cr-Nb)N coatings whereas the voltage above -700 V promoted the formation of a layer dominated by $\boldsymbol{\gamma_N}$ (200) [T*=73%]. HIPIMS nitriding process was almost 10 times faster than that of the benchmarked DCPN.

2. Microstructures of the samples revealed that lower nitriding voltage (-700 V) formed a layer which has two distinct interfaces (substrate/diffusion layer and diffusion/ compound layer). As voltage increased further (above -900 V) the diffusion layer disappeared leaving the substrate/compound layer, voltages of -1000 V and -1100 V formed pure compound layer. Elemental depth analysis of the nitrided layer showed that the nitriding depth increased from 1.2 µm (at -700 V) to ~6.0 µm (at -1100 V). Further GDOES analysis showed that the nitrogen concentration in compound layer reached up to ~45 at% (Co_2N) and gradually decreased to below 30 at.% (Co_3N). The

lowest N concentration observed in all cases was 2 at.% (Co_4N). As compared to DCPN, HIPIMS nitrided samples have a higher (about two times) nitrogen concentration in the compound layer, estimated at the control depth of 1.5 µm.

3. Surface hardness tests showed that a significant increase in hardness after HIPIMS nitriding (Hp: 23 GPa and HK0.01= 2750, at -1100 V) was achieved which was better than DCPN (Hp= 20) and 5 times harder than that of untreated alloy.

4. Systematic increment in the elastic (H/E) and plastic (H3/E2) index ratio indicated an increase in fracture toughness (KIc values) especially at lower nitriding voltages (-700 V and -900 V). A general improvement in shock absorbing capacity, crack resistance and thereby in fatigue resistance under cyclic impact loading was observed for HIPIMS nitrided samples.

5. Dry sliding wear resistance of the CoCrMo alloy increased by almost two orders of magnitude with reduced friction values.

6. A significant improvement in the corrosion resistance of the CoCrMo alloy (NaCl: E_{Corr}= -590 mV and Hank's: E_{Corr}= -776 mV) was observed after HIPIMS nitriding for both NaCl (E_{Corr}= -133.39 mV) and Hank's solution (E_{Corr}= -205 mV) with two orders of magnitude lower corrosion current as a result of a uniform, defect free and with an uninterrupted microstructure. ICPMS analysis revealed that HIPIMS nitriding provides a reliable barrier, which reduces metal ions release significantly from bio-grade CoCrMo alloy.

Finally, it can be concluded that the nitrided layer formed using HIPIMS discharge at -700 V and -900 V may be used as a layer which can provide a stress/hardness gradient for depositing a top nanostructured coating to realise duplex surface treatment.

6.2. Future Work:

- Deposition of duplex coating (HIPIMS nitriding and nanostructured multilayer coating).
- Microstructural and phase composition analysis of the duplex coatings.
- Analysis of mechanical properties such as hardness, elastic modulus, fracture toughness (K_{Ic}), toughness and load impact fatigue of the alloy.
- Corrosion and tribocrossion analysis of the duplex coatings.
- Analysis of metal ion release during corrosion and tribocrossion analysis of the duplex coatings.